

**EVALUATION OF DISPERSIVE MIXING, EXTENSION RATE AND
BUBBLE SIZE DISTRIBUTION USING NUMERICAL
SIMULATION OF A NON-NEWTONIAN FLUID IN A TWIN-
SCREW MIXER**

by

MAUREEN L. RATHOD

A Dissertation submitted to the
Graduate School – New Brunswick
Rutgers, The State University of New Jersey
in partial fulfillment of the requirements

for the degree of

Doctor of Philosophy

Graduate Program in Food Science

written under the direction of

Dr. Jozef L. Kokini

and approved by

New Brunswick, New Jersey

May, 2015

ABSTRACT OF THE DISSERTATION

**EVALUATION OF DISPERSIVE MIXING, EXTENSION RATE AND
BUBBLE SIZE DISTRIBUTION USING NUMERICAL
SIMULATION OF A NON-NEWTONIAN FLUID IN A TWIN-
SCREW MIXER**

by

MAUREEN L. RATHOD

Dissertation Director:

Dr. Jozef L. Kokini

Initially 3D FEM simulation of a simplified mixer was used to examine the effect of mixer configuration and operating conditions on dispersive mixing of a non-Newtonian fluid. Horizontal and vertical velocity magnitudes increased with increasing mixer speed, while maximum axial velocity and shear rate were greater with staggered paddles. In contrast, parallel paddles produced an area of efficient dispersive mixing between the center of the paddle and the barrel wall.

This study was expanded to encompass the complete nine-paddle mixing section using power-law and Bird-Carreau fluid models. In the center of the mixer, simple shear flow was seen, corresponding with high $\dot{\gamma}$. Efficient dispersive mixing appeared near the barrel wall at all flow rates and near the barrel center with parallel paddles. Areas of backflow, improving fluid retention time, occurred with staggered paddles. The Bird-Carreau fluid showed greater influence of paddle motion under the same operating

conditions due to the inelastic nature of the fluid. Shear-thinning behavior also resulted in greater maximum shear rate as shearing became easier with decreasing fluid viscosity.

Shear rate distributions are frequently calculated, but extension rate calculations have not been made in a complex geometry since Debbaut and Crochet (1988) defined extension rate as the ratio of the third to the second invariant of the strain rate tensor. Extension rate was assumed to be negligible in most studies, but here extension rate is shown to be significant. It is possible to calculate maximum stable bubble diameter from capillary number if shear and extension rates in a flow field are known. Extension rate distributions were calculated for Newtonian and non-Newtonian fluids. High extension and shear rates were found in the intermeshing region. Extension is the major influence on critical capillary number and maximum stable bubble diameter, but when extension rate values are low shear rate has a larger impact. Examination of maximum stable bubble diameter through the mixer predicted areas of higher bubble dispersion based on flow type. This research has advanced simulation of non-Newtonian fluid and shown that direct calculation of extension rate is possible, demonstrating the effect of extension rate on bubble break-up.

ACKNOWLEDGEMENTS

- Dr. Jozef L. Kokini, my advisor, teacher, and mentor: for his guidance in my research and for showing me what is necessary to present and publish high quality work.
- Members of my Defense Committee: Dr. Paul Takhistov, Dr. Kit Yam, Dr. Robin Connelly; and my Oral Qualifier Committee: Dr. Paul Takhistov, Dr. Henryk Daun, Dr. Robin Connelly
- My labmates and friends: for sharing the journey.

DEDICATION

I dedicate this work to my family, for their love, support, encouragement, and sharing the belief that I would reach this goal.

My husband, Jigar.

My parents, Kathryn and John.

My brother, Andrew.

Table of Contents

ABSTRACT OF THE DISSERTATION	ii
ACKNOWLEDGEMENTS	iv
DEDICATION	v
Table of Contents	vi
List of Tables	ix
List of Figures	x
Chapter 1 - Introduction	1
1.2 Objectives:	3
1.3 Hypothesis	3
1.4 Research Strategy	4
1.5 Background	5
1.5.1 Benchmark Mixing Problems	5
1.5.2 Simple Mixers	9
1.5.3 CFD in a model batch mixer	12
1.5.4 2D Numerical Simulation	14
1.5.6 3D Numerical Simulation in a Twin-Screw Mixer	23
1.5.7 Scaling	25
1.5.8 Adaptive remeshing	26
1.5.9 Mesh superposition	28
1.5.10 Effect of Stagger Angle	29
1.5.11 Extension Rate Fundamental Studies	32
1.5.12 Bubble Breakup and Flow Type	34
1.6 Research Methods	41
1.6.1 Numerical Simulations	41
1.6.2 Fluid Rheology	42
1.6.3 Mixing Measurements	44
1.6.4 Critical Capillary Number and Maximum Stable Bubble Diameter	49
Chapter 2 - EFFECT OF MIXER GEOMETRY AND OPERATING CONDITIONS ON MIXING EFFICIENCY OF A NON-NEWTONIAN FLUID IN A TWIN SCREW MIXER ¹	54
2.1 Abstract	54
2.2 Introduction	55
2.3 Materials and Methods	59
2.3.1 Fluid Rheology	59
2.3.2 Characterization of mixing performance	60
2.3.3 Numerical Simulations	61
2.3.4 Mesh superposition	61
2.3.5 Mixer Geometry	62
2.4 Results and Discussion	65
2.4.1 Effect of flow rate on 3-D velocity distributions	65
2.4.2 Effect of flow rate on shear rate and mixing index	68
2.4.4 Effect of mixer speed on 3D velocity distribution	70
2.4.5 Effect of mixer speed on shear rate and mixing index	73
2.5 Conclusions	74

Chapter 3 - NON-NEWTONIAN FLUID MIXING IN A TWIN SCREW MIXER GEOMETRY: 3D MESH DEVELOPMENT, EFFECT OF FLUID MODEL AND OPERATING CONDITIONS ¹	76
3.1 Abstract	76
3.2 Practical Application	77
3.3 Introduction	77
3.4 Materials and Methods	81
3.4.1 Radial and axial mesh density	83
3.4.2 Determination of mesh quality	87
3.4.2.1 <i>Equiangle skew</i>	87
3.4.2.2 <i>Stretch ratio</i>	88
3.4.3 Simulation validation	90
3.4.3.1 <i>Experimental determination of velocity profiles</i>	90
3.4.3.2 <i>Calculation of simulation and experimental difference</i>	93
3.4.4 Calculation of mixing index	93
3.5 Results and Discussion	94
3.5.1 Selection and validation of mesh density	94
3.5.2 Effect of flow rate on mixing in a power-law fluid	99
3.5.3 Effect of mixer speed on mixing in a power law fluid	102
3.5.4 Effect of flow rate on mixing in a Bird-Carreau fluid	104
3.6 Conclusions	110
Chapter 4 - EXTENSION RATE DISTRIBUTION AND IMPACT ON BUBBLE SIZE DISTRIBUTION IN NEWTONIAN AND NON-NEWTONIAN FLUID IN A TWIN SCREW CO-ROTATING MIXER ¹	112
4.1 Abstract	112
4.2 Introduction	113
4.3 Materials and Methods	116
4.3.1 Description of the numerical simulation	116
4.3.2 Simulation of extension rate	118
4.3.3 Calculation of critical capillary number and maximum stable bubble diameter	120
4.4 Results and Discussion	121
4.4.1 Analysis of extension rates in the twin screw mixer	121
4.4.1.1 <i>Extension rate variation with viscosity and mixer operating parameters for a Newtonian fluid in a sample plane</i>	121
4.4.1.2 <i>Extension rate variation with mixer operating parameters for a non- Newtonian fluid in a sample plane</i>	124
4.4.1.3 <i>Analysis of the distribution of the magnitude of extension rate in the axial direction in the mixer</i>	126
4.4.1.4 <i>Analysis of the distribution of the magnitude of extension rate in the horizontal direction of the mixer</i>	130
4.4.2 Distribution of shear rates in the twin screw mixer	132
4.4.2.1 <i>Analysis of the distribution of the magnitude of shear rate in the axial direction in the mixer</i>	132
4.4.2.2 <i>Analysis of the distribution of the magnitude of shear rate in the horizontal direction in the mixer</i>	133

4.4.3 Relative effect of extension rate and shear rate on critical capillary number and maximum stable bubble diameter in a non-Newtonian fluid.....	134
4.5 Conclusions.....	141
Chapter 5 - Conclusions.....	142
References.....	145

List of Tables

Table 1.1 Influence of fluid rheology on the linear instability of Taylor-couette flow (Al Mubaiyedh et al., 2000)	8
Table 1.2. Critical Capillary Number for Different Flow Types	51
Table 1.3. Values of second and third invariants of the rate of deformation tensor in simple shear and uniaxial extensional flow (Debbaut and Crochet, 1988).....	52
Table 1.4. Mixing index and flow type parameter (Bentley and Leal, 1986).....	53
Table 3.1. Settings used for LDA system (Fanning, 2009)	92
Table 3.2. Quality of meshes with varying radial gradation (Ashokan, 2008).....	94
Table 3.3. Comparison of RMS % difference at points P1, P2 and P3 for the four 2D meshes investigated using corn syrup with a flow rate of 53cc/s into the mixer (Ashokan, 2008).....	94
Table 4.1. Comparison of highest extension rates for Planes 1, 2, 3, 4, and 5	127

List of Figures

Figure 1.1. Geometry of the cavity with time-periodic oscillatory lid velocity (Anderson et al., 2000a).	5
Figure 1.2. Effect of increasing amplitude, P on the chaotic advection in the cavity shown as deformation in the material strip (Anderson et al., 2000a).	6
Figure 1.3. Time evolution of Newtonian (N) and shear thinning polyacrylamide fluids dissolved in glycerol to various concentrations (C_1 , C_2 and C_3) in terms of area coverage by a dye (Leong and Ottino, 1990).	7
Figure 1.4. Probability distribution function of ξ/Re at $Re = 20, 40, 80$ and 160 (Zalc et al., 2001).	10
Figure 1.5. Percentage of the total volume invaded by tracer particles vs. number of impeller revolutions for $Re=20, 40, 80$, and 160 (Alvarez et al., 2002).	11
Figure 1.6. Mixing efficiency as a function of Re (Zalc et al., 2002).	11
Figure 1.7. a) Laser speckle photographs for 1% CMC solution in the one-rod geometry at various Reynolds numbers, b) Stream functions for an inelastic material in the one-rod geometry at various Reynolds numbers (Binding et al., 2003).	13
Figure 1.8. Velocity vectors showing the direction of the flow and colored by the magnitude of the velocity (cm/s). a) Single screw mixer rotating reference frame where the barrel is rotating counterclockwise and the paddle is fixed, b) Single screw mixer in the inertial reference frame where the barrel is fixed and the paddle rotates	

clockwise, c) Twin screw mixer after the paddles have turned clockwise 67.5° from the initial position. (Connelly and Kokini, 2007).	15
Figure 1.9. Mapping of the mixing index (λ_{MZ}) in a) the single screw mixer and the twin screw mixer at positions, b) 45° , c) 67.5° , d) 90° from the initial position where a value of 0 indicates pure rotation, a value of 0.5 indicates shear flow and a value of 1 indicates pure elongation. (Connelly and Kokini, 2007).	16
Figure 1.10. Mapping of the shear stress (τ_{12}) distributions where the units of stress are g/cm^2 in a) the single screw mixer and the twin screw mixer at positions b) 45° , c) 67.5° , d) 90° from the initial position. (Connelly and Kokini, 2007).	17
Figure 1.11. Particle tracking results showing the distributive mixing of a cluster (b1) of non-cohesive, material points initially centered in the leftmost section of the flow field a) initially, b) after 10 revolutions (Connelly and Kokini, 2007).	18
Figure 1.12. Particle tracking results showing the distributive mixing of a cluster (b2) of a non-cohesive, material points initially located behind the paddle in the leftmost section of the flow field a) initially, b) after 10 revolutions (Connelly and Kokini, 2007).	18
Figure 1.13. The mean and standard deviation of the length of stretch over 10 revolutions of the mixing paddles (Connelly and Kokini, 2007).	19
Figure 1.14. The mean and standard deviation of the time averaged mixing efficiency over 10 revolutions of the mixing paddles (Connelly and Kokini, 2007)	20
Figure 1.15. Manas-Zloczower mixing index distributions at 1 rpm of a) Newtonian, b) Oldroyd-B with relaxation time of 1.5 s, c) Bird–Carreau viscous, d) Phan-Thien Tanner fluid models (Connelly and Kokini, 2004).	21

Figure 1.16. Shear stress (τ_{12}) distributions at 1rpm of a) Newtonian, b) Oldroyd-B with relaxation time of 1.5s, c) Bird-Carreau viscous, d) Phan-Thien Tanner fluid models where the units of stress are dyne/cm ² (Connelly and Kokini, 2004).	22
Figure 1.17. Contour maps of dispersive mixing index λMZ , over three XY cross-sectional planes at time step 4 for FLAT configuration at 100 RPM a) P1, b) P4, c) P8 . Legend – yellow to red shades show predominantly elongation flow, green shades are predominantly shear and blue shades are predominantly rotation (Vyakaranam, 2012).	24
Figure 1.18. a) Illustration of ‘Squeeze flow’ in the intermeshing region between the paddle element surfaces and barrel wall surfaces causing a predominantly elongation flow, b) Velocity vector maps for the FLAT configuration at time step 4, 40° (Vyakaranam, 2012).	25
Figure 1.19. Demonstration of extruder scale-down (Dhanasekharan and Kokini, 2003).	26
Figure 1.20. Two-level adaptive mesh refinement procedure in the vicinity of the gaps (Bertrand et al., 2003).	27
Figure 1.21. Reference mesh for 2D twin-screw extrusion, before adaptive remeshing (Bertrand et al., 2003).	27
Figure 1.22. Variation of pressure with screw position. Simulated values from adapted mesh (Bertrand et al., 2003).	28
Figure 1.23. Pressure distributions in the axial direction with different stagger angles (Ishikawa et al., 2001).	30

Figure 1.24. Temperature distributions in the axial direction with different stagger angles (Ishikawa et al., 2001).....	30
Figure 1.25. Distributions of stress magnitudes with different stagger angles (Ishikawa et al., 2001).	31
Figure 1.26. Distributions of area stretch with different stagger angles (Ishikawa et al., 2001)..	31
Figure 1.27. The effect of L/a on the relaxation and breakup process. a) $A = 0.018$, b) 0.47, The horizontal arrows indicate when the flow is stopped. Data points for each experiment then continue until the first fragment separates from the main drop. A/A_0 denotes the fractional increase in interfacial area due to the fragmentation. The solid, almost vertical line indicates the rate at which a fluid element stretches in the linear flow, Δ , $\alpha = 1.0$; \square , 0.8; $*$, 0.6; \diamond , 0.6 (Stone et al., 1986).	36
Figure 1.28. The effect of flow type on elongation process and on subsequent relaxation and breakup phenomena. Viscosity ratio is held constant, $\lambda=0.09$, a) $\alpha=0.6$, $G_c=0.224s^{-1}$, b) $\alpha=0.2$, $G_c=0.33s^{-1}$ (Stone et al., 1986).	37
Figure 1.29. Critical elongation ratio necessary to ensure breakup, following an abrupt halt of the flow, as a function of viscosity ratio. Triangles denote the smallest L/a for which a drop was observed to breakup. Squares denote the largest L/a for which a drop relaxed back to a sphere. The shaded region denotes the uncertainty in the critical elongation ratio. The dashed line indicates the L/a values of the final steady shapes (Stone et al., 1986).	38
Figure 1.30. Mean Ca in the mixer vs Ca_{cr} Bubble breakup is possible only in elongation flow regions (Vyakaranam and Kokini, 2012).	39

Figure 1.31. Mean bubble diameter vs. simulated maximum stable bubble diameter as a function of dispersive mixing index (Vyakaranam and Kokini, 2012).	40
Figure 1.32. Effective shear rate vs. simulated mean shear rate assuming flow type a) pure elongation $\lambda_{MZ}=1$, b) simple shear $\lambda_{MZ}=0.5$, c) mixed flow $\lambda_{MZ}=0.6$ (Vyakaranam and Kokini, 2012).	41
Figure 1.33. Rheological properties of 2% CMC (Prakash, 1996).	44
Figure 1.34. Deformation of elements, lines and volumes (Ottino, 1989).	46
Figure 1.35. Typical behavior of mixing efficiency (Ottino, 1989).	46
Figure 1.36. Particle tracking results illustrating the distributive mixing between the upper and lower halves of both mixers a) initially, b) after one revolution, c) after 10 revolutions where the red (light) colored points were arbitrarily assigned a concentration of 1 and the blue (dark) colored points a concentration of zero (Connelly and Kokini, 2007).	47
Figure 1.37. Stream lines for linear flow $u = \Gamma \cdot x$ (Stone et al., 1986).	50
Figure 1.38. Scalar measures of deformation and orientation (Stone et al., 1986).	50
Figure 2.1. a) 2" Readco continuous processor with Plexiglas barrel, b) close-up of paddles in parallel configuration (Ashokan, 2008).	63
Figure 2.2. 3D barrel mesh with two pairs of superimposed paddles a) front view b) side view.	63
Figure 2.3. Paddle angle used in simulations.	64
Figure 2.4. Location of measurement points along the line between point P1 and point P2.	65
Figure 2.5. X component of velocity different flow rates for 2X, 2X45, 2X90.	66

Figure 2.6.. Y component of velocity at different flow rates for 2X, 2X45, 2X90.	67
Figure 2.7. Z component of velocity at different flow rates for 2X, 2X45, 2X90.....	68
Figure 2.8. Shear rate at different flow rates for 2X, 2X45, 2X90.	69
Figure 2.9. Mixing index at different flow rates for 2X, 2X45, 2X90.....	70
Figure 2.10. X velocity component at different rotation speeds for 2X, 2X45, 2X90.	71
Figure 2.11. Y velocity component at different rotation speeds for 2X, 2X45, 2X90.	72
Figure 2.12. Z velocity component at different rotation speeds for 2X, 2X45, 2X90.....	72
Figure 2.13. Shear rate at different rotation speeds for 2X, 2X45, 2X90.....	73
Figure 2.14. Mixing index at different rotation speeds for 2X, 2X45, 2X90.	74
Figure 3.1. Radial gradation of mesh density: a) Uniform, b) Radial, c) Radial-8-16, d) Radial-8-12, e) Radial-6-9, f) and g) Radial-4-6, h) Radial-4-6-azi.	84
Figure 3.2. 2D meshes with varying radial mesh density a) Mesh #1, b) Mesh #2, c) Mesh #3, d) Mesh #4 (Ashokan, 2008).	85
Figure 3.3. Barrel meshes with a) 2, b) 3, c) 4, d) 5 mesh intervals in the region of the paddles (Ashokan, 2008).	86
Figure 3.4. Three pair paddle mesh with a) nine, b) five mesh intervals.....	87
Figure 3.5. Nine paddle a) barrel, b) paddle meshes.	89
Figure 3.6. Position of a) Line 1, Points P1, P2, P3, b) Line 2 in the mixer.....	89
Figure 3.7. Mixer configurations and position of Line 3 a) parallel paddles, b) 45° staggered paddles.	89
Figure 3.8. LDA system a) Schematic (Fanning, 2009), b) Probe and beams (Ashokan, 2008).	90

Figure 3.9. Comparison of velocity magnitudes along Line 1 for Mesh #1 (■), Mesh #2 (◆), Mesh #3 (□) and Mesh #4 (◇) (Ashokan, 2008).....	95
Figure 3.10. Velocity comparison along Line 2 for meshes with 2 (■), 3 (◆), 4 (□) and 5 (◇) axial mesh intervals (Ashokan, 2008).	96
Figure 3.11. RMS % difference at point P1 between experimental and simulated values as a function of axial location for simulation geometries having 1 pair (■), 2 pairs (◆), 3 pairs (▲), 4 pairs (□) and 5 pairs (◇) of paddles in the a) v_x velocity component, b) v_z velocity component (Ashokan, 2008).	97
Figure 3.12. Velocity comparison along Line 2 for 3 paddle pair meshes with gaps (■), fused 3 paddle pair meshes with 9 (▲) and 5 (□) axial intervals (Ashokan, 2008). ..	98
Figure 3.13. RMS % difference at point P1 between experimental and simulated values as a function of axial location for simulation geometries having 5 pairs (■), 5 pairs with increase in entrance length (□) and 9 pairs (▲) of paddles in the a) v_x velocity component, b) v_z velocity component (Ashokan, 2008).	99
Figure 3.14. Power-law fluid velocity components along Line 3 at different fluid inflow rates and stagger angles a) 9X v_x , b) 9X45 v_x , c) 9X v_y , d) 9X45 v_y , e) 9X v_z , f) 9X45 v_z	100
Figure 3.15. Power-law fluid shear rate and mixing index along Line 3 at different fluid inflow rates and stagger angles a) 9X $\dot{\gamma}$, b) 9X45 $\dot{\gamma}$, c) 9X λ_{MZ} , d) 9X45 λ_{MZ}	101
Figure 3.16. Power-law fluid velocity components along Line 3 at different mixer speeds and paddle stagger angles a) 9X v_x , b) 9X45 v_x , c) 9X v_y , d) 9X45 v_y , e) 9X v_z , f) 9X45 v_z	102

Figure 3.17. Power-law fluid shear rate and mixing index along Line 3 at different mixer speeds and paddle stagger angles a) 9X $\dot{\gamma}$, b) 9X45 $\dot{\gamma}$, c) 9X λ_{MZ} , d) 9X45 λ_{MZ} ..	103
Figure 3.18. Bird-Carreau fluid velocity components along Line 3 at different fluid inflow rates and paddle stagger angles a) 9X v_x , b) 9X45 v_x , c) 9X v_y , d) 9X45 v_y , e) 9X v_z , f) 9X45 v_z	105
Figure 3.19. Bird-Carreau fluid shear rate and mixing index along Line 3 at different fluid inflow rates and paddle stagger angles a) 9X $\dot{\gamma}$, b) 9X45 $\dot{\gamma}$, c) 9X λ_{MZ} , d) 9X45 λ_{MZ}	106
Figure 3.20. Bird-Carreau fluid velocity components along Line 3 at different mixer speeds and paddle stagger angles a) 9X v_x , b) 9X45 v_x , c) 9X v_y , d) 9X45 v_y , e) 9X v_z , f) 9X45 v_z	108
Figure 3.21. Bird-Carreau fluid shear rate and mixing index along Line 3 at different mixer speeds and paddle stagger angles a) 9X $\dot{\gamma}$, b) 9X45 $\dot{\gamma}$, c) 9X λ_{MZ} , d) 9X45 λ_{MZ}	109
Figure 4.1. Nine paddle length barrel and paddle meshes (Rathod et al., 2014).	116
Figure 4.2. XY plane of superimposed barrel and paddle meshes.....	117
Figure 4.3. Location of Planes used to examine extension rates in the mixer a) Planes 1-5, b) Planes 6-12.	119
Figure 4.4. Extension rate for Newtonian corn syrup over three revolutions.....	122
Figure 4.5. Extension and shear rate versus mixer speed and fluid inflow rate in Newtonian fluids over one revolution at three mixer speeds.....	122
Figure 4.6. Ratio of maximum extension ratio to maximum shear rate for Newtonian fluids.	123

Figure 4.7. Extension rate for a non-Newtonian 2% CMC solution over three revolutions.	125
Figure 4.8. Extension rate and shear rate versus mixer speed and fluid inflow rate over three revolutions in a 2% CMC solution.	125
Figure 4.9. Ratio of maximum extension rate to shear rate over three revolutions for a 2% CMC solution.	126
Figure 4.10. Evolution of extension rate across characteristic axial planes a) 1, b) 2, c) 3, d) 4, e) 5.	128
Figure 4.11. Evolution of extension rate across characteristic horizontal planes a) 6, b) 7, c) 8.	131
Figure 4.12. Evolution of shear rate across characteristic axial planes a) 1, b) 2.	132
Figure 4.13. Evolution of shear rate across characteristic horizontal planes a) 6, b) 7, c) 8.	134
Figure 4.14. Relative effect of extension rate on a) critical capillary number and b) maximum stable bubble diameter.	135
Figure 4.15. Maximum stable bubble diameter at 100rpm and 55.31cc/s through the mixer a) yz view, b) angled view.	137
Figure 4.16. Maximum stable bubble diameter through the mixer a) 20cc/s, b) 100cc/s, c) 50rpm, d) 150rpm.	139

Chapter 1 - Introduction

Industries such as food, pharmaceuticals, polymers, and personal care depend on mixing processes to achieve their final product. Mixing is used to combine ingredients, develop structure, and entrain air. This is particularly important in wheat flour dough to disperse water and break flour, separating starch and protein for gluten formation. Glutenin is also stretched for molecular alignment and non-covalent bond formation resulting in elasticity, machinability and volume expansion. Bubbles formed during mixing become nuclei for carbon dioxide produced by fermentation (Connelly and Kokini, 2007).

Different types of mixers, including batch and continuous mixers with fixed and adaptable geometries, generate distinct mixing behavior. Banbury mixer, Brabender Farinograph, double sigma blade mixers, planetary mixers, spiral mixers, single and twin screw mixers are all examples. In general efficient mixers have a complicated geometry combined with several moving parts to enable fluid reorientation in the mixer. These geometries make the experimental evaluation of mixing more difficult and add a level of complexity and computational cost to numerical simulation. Using a simplified geometry such as an eccentric cylinder, Taylor-couette flow, flow past a cylinder, or a lid-driven cavity mixer can help to understand mixing while avoiding more complex calculations. Another way of combating this is to use a simplified mixer such as a stirred tank or couette. Additionally one can use a simpler fluid model.

A distinct advantage of numerical simulation is that, unlike experimental sampling, it can be used to determine data values at all points throughout the geometry of the mixer without disrupting fluid mixing. The challenge is that increasing complexity of

fluid model and geometry greatly increases the demand on computing power, increasing memory and time needed for simulation.

Mixing efficiency is determined by both distributive and dispersive mixing. Distributive mixing spreads material throughout the volume by stretching and reorientation. It is measured by length stretch, stretching efficiency, and segregation scale. Dispersive mixing breaks droplets, clumps, or bubbles and is measured by the Manas-Zloczower mixing index.

Extensive analysis of mixing has been performed using simple geometries and fluids. Previous work in our lab has examined Newtonian and non-Newtonian fluids, as well as model and industrial mixers. In this work we have explored dispersive mixing of non-Newtonian fluids in a realistic geometry, leading to extension rate distribution and maximum stable bubble size to better understand bubble break-up.

1.2 Objectives:

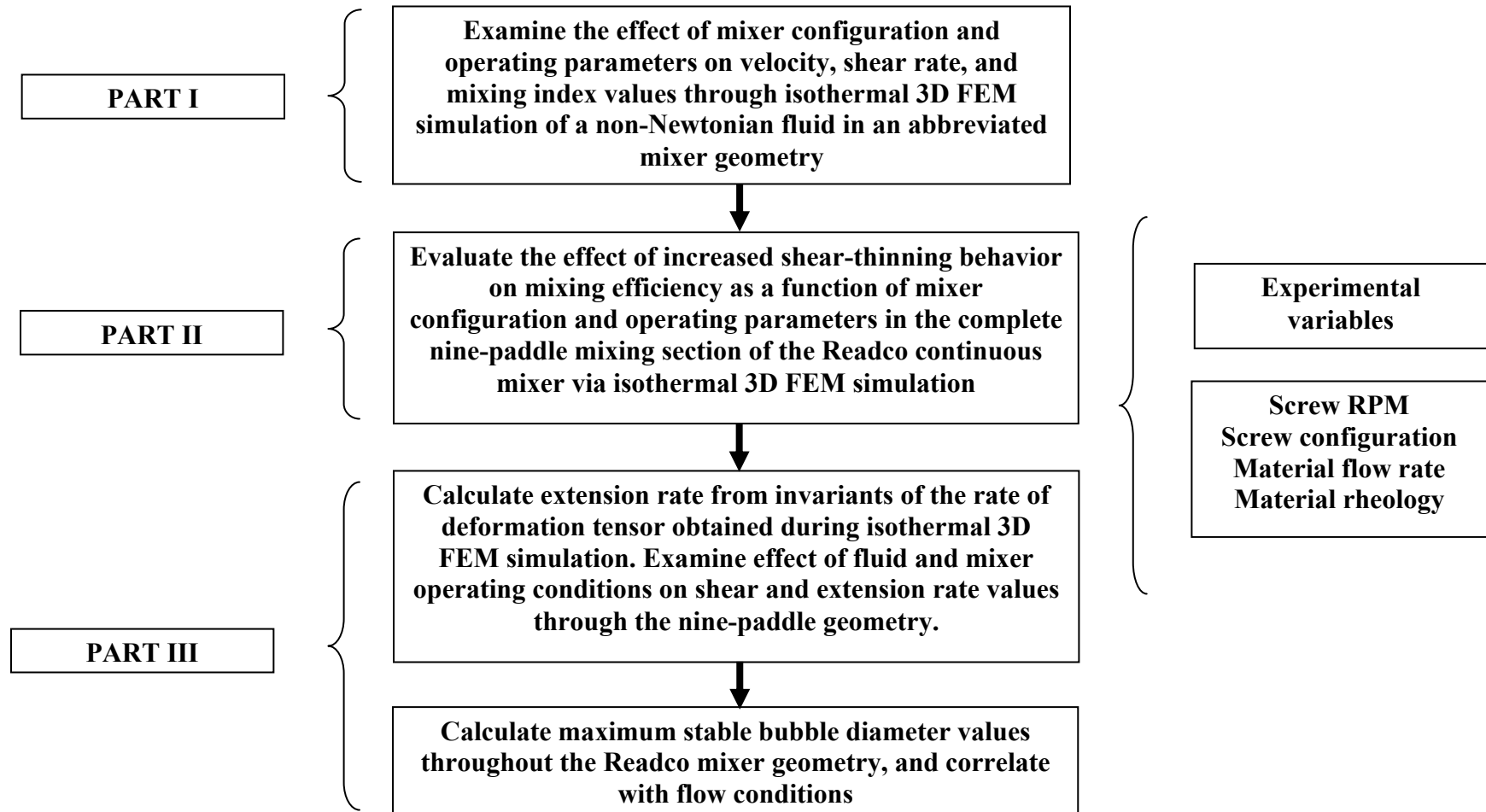
The objectives of this work are:

1. To examine the effect of paddle angle, fluid inflow rate, and mixer speed on velocity, shear rate, and mixing efficiency of a non-Newtonian fluid in abbreviated mixer configurations.
2. To explore the effect of increased shear-thinning behavior by comparing mixing of power-law and Bird-Carreau fluid models in the complete nine-paddle mixing section.
3. To calculate extension rates and map their distribution for Newtonian and non-Newtonian fluids in order to predict the contribution of extensional flows to deformation rate and bubble dispersion.

1.3 Hypothesis

Twin screw mixer configuration and operating conditions influence fluid mixing due to their effect on shear and extension rates. Shear rate is not sufficient to predict fluid behavior due to the impact of extension rate on flow and bubble dispersion in the mixer. Calculation of extension rate will enable direct evaluation of critical capillary number and maximum stable bubble diameter to be used for development of design criteria for dispersion of air and generation of nucleation sites throughout the mixer geometry.

1.4 Research Strategy



1.5 Background

1.5.1 Benchmark Mixing Problems

Simplified model geometries such as eccentric cylinder, Taylor-couette flow, and lid-driven cavity mixers are often used to observe fluid mixing. These models are used to reduce the complexity of mathematical simulation and enable validation using more basic experiments.

Anderson, et al. (2000a, 2000b) investigated a lid-driven cavity geometry (Figure 1.1) and found that using a pulsating lid velocity (Equation 1.1) lead to chaotic mixing in the core of the cavity (Figure 1.2). When steady motion of the opposite wall is induced, the well-mixed region spreads throughout the cavity. These experiments show the effect of boundary conditions on mixing efficiency.

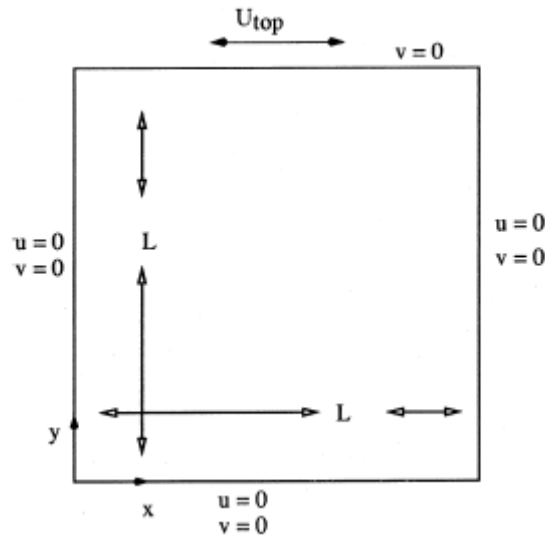


Figure 1.1. Geometry of the cavity with time-periodic oscillatory lid velocity (Anderson et al., 2000a).

$$\begin{cases} u = U_{\text{top}} = 1 + P \sin(\frac{2\pi x}{T}) & v = 0 \text{ top wall,} \\ u = 0 & v = 0 \text{ side and bottom walls.} \end{cases} \quad \text{Equation 1.1}$$

P is the amplitude of oscillation over a time period T.

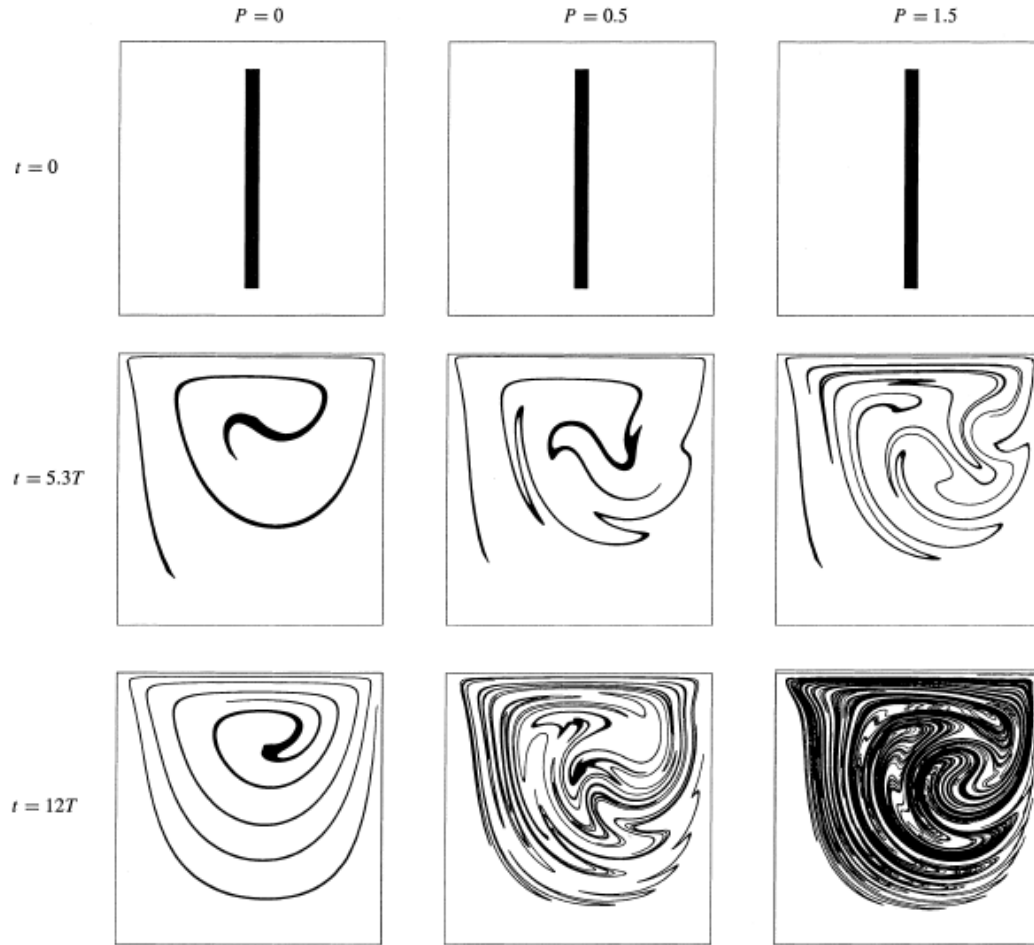


Figure 1.2. Effect of increasing amplitude, P on the chaotic advection in the cavity shown as deformation in the material strip (Anderson et al., 2000a).

The effects of boundary conditions on mixing were also studied by Kumar and Homsy (1996). They found that the viscoelasticity of an Oldroyd B fluid increased the chaotic mixing rate with different boundary motion. In simulating this situation, the researchers applied a viscoelastic correction to the Newtonian flow field using standard finite differences over a long time of motion. Through this research the investigators found that periodic and time-dependent disturbances improved mixing efficiency.

Leong and Ottino (1990) saw that shear thinning decreased mixing efficiency because it increased the number and size of isolated islands within the geometry. The

decrease in size and intensity of the chaotic mixing regions in time-periodic flow caused a decrease in stretching. To illustrate this, they mixed dye with both Newtonian and shear-thinning fluids and observed the size of the colored area. From this information, they determined that an increase in shear-thinning behavior correlated with a decrease in rate of stretching (Figure 1.3).

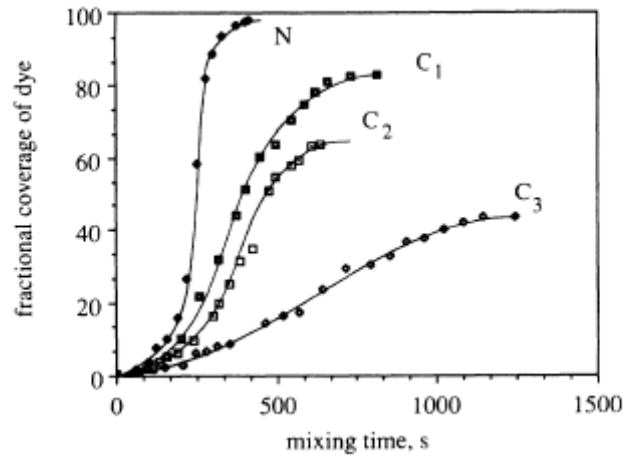


Figure 1.3. Time evolution of Newtonian (N) and shear thinning polyacrylamide fluids dissolved in glycerol to various concentrations (C_1 , C_2 and C_3) in terms of area coverage by a dye (Leong and Ottino, 1990).

Al Mubaiyedh et al. (2000, 2002a, 2002b) used a Taylor-couette geometry to examine the linear and non-linear effects in viscoelastic fluid flow stability. They looked at the effect of fluid rheology on the purely elastic instability of Taylor-couette flow, in particular the relaxations times, shear thinning at first normal stresses, finite second normal stresses, and the ratio of solvent to total viscosity (Al Mubaiyedh et al., 2000). Through this research they determined that the critical Deborah number (De_c – the ratio of fluid relaxation time to characteristic flow time scale at the onset of instability) decreased as the number of relaxation times describing the rheology of the fluid increased (Table 1.1).

Table 1.1 Influence of fluid rheology on the linear instability of Taylor-couette flow (Al Mubaiyedh et al., 2000)

Constitutive model	$\delta = 0.912$				$\delta = 0.8$			
	ξ	α_c	De_c	σ_{Ic}	ξ	α_c	De_c	σ_{Ic}
1-mode Oldroyd-B	0	7.7	21.55	0.0480	0	10.5	15.15	0.0755
	1	5.5	16.41	0.0186	1	5.8	11.38	0.0167
	2	5.4	16.09	0.0048	2	6.9	13.41	0.0158
4-mode Oldroyd-B	0	7.8	12.80	0.0216	0	11.9	9.20	0.0331
	1	4.8	8.38	0.0064	1	4.8	5.85	0.0222
	2	4.9	9.38	0.0243	2	5.8	8.16	0.0438
4-mode Phan-Thien and Tanner	0	7.3	68.63	0.0223	0	9.0	32.88	0.0387
	1	4.8	31.44	0.0036	1	4.8	18.81	0.0198
	2	4.9	35.35	0.0238	2	5.7	28.131	0.0446
4-mode Giesekus	0	6.8	90.82	0.0203	0	8.7	37.45	0.0372
	1	4.7	34.16	0.0036	1	4.7	19.63	0.0196
	2	4.8	39.61	0.0230	2	5.8	30.23	0.0421

In validation of the simulations, it was found that there was a noticeable difference between the data obtained by the isothermal simulation of purely elastic flow and the experiment. This discrepancy was theorized to be caused by the neglect of viscous heating in the simulation. Once viscous heating was taken into account De_c was shown to be one order of magnitude lower and much closer to the experimental values. The secondary flow patterns also coincided for the non-isothermal simulations and the experiments. This investigation illustrated the suitability of non-isothermal flow simulations given a fluid viscosity that is temperature sensitive, where a minor temperature fluctuation causes clear secondary flow patterns.

The previous benchmark problems show the effect of boundary conditions and fluid rheology on flow and mixing efficiency in a model mixer. The disadvantage of these problems is that they are very simple geometrically. They are not applicable to real-world situations because they have no complex impellers or complicated boundary

conditions. Despite these drawbacks, such studies allow the initial application of new techniques which can later be applied to more complicated geometries.

1.5.2 Simple Mixers

Mixing scenarios such as stirred tank reactors, static mixing flow, and laminar to turbulent flow regimes have been studied by F.J. Muzzio and his research group using generalized Newtonian fluids and models. Both experimental and CFD (computational fluid dynamics) methods were used to examine mixing. A selection of previous exploration appears in this section. Additional work from this group is summarized in sections 2.2 and 3.3.

Zalc et al. (2001) analyzed a three-impeller, unbaffled stirred tank with a rotating reference frame. These simulations were validated against PIV data obtained using a water and glycerin solution. Researchers analyzed the calculated magnitude of the deformation tensor, ξ , and found that its magnitude increased nonlinearly with Reynolds number, Re . The probability function of ξ/Re (Figure 1.4) showed an increase in ξ with increased Re . Local spatial derivatives of the velocity field determine stretching, folding, and reorientation of fluid elements. Knowing the velocity gradients at different locations in the flow allow the determination of regions with the greatest mixing potential.

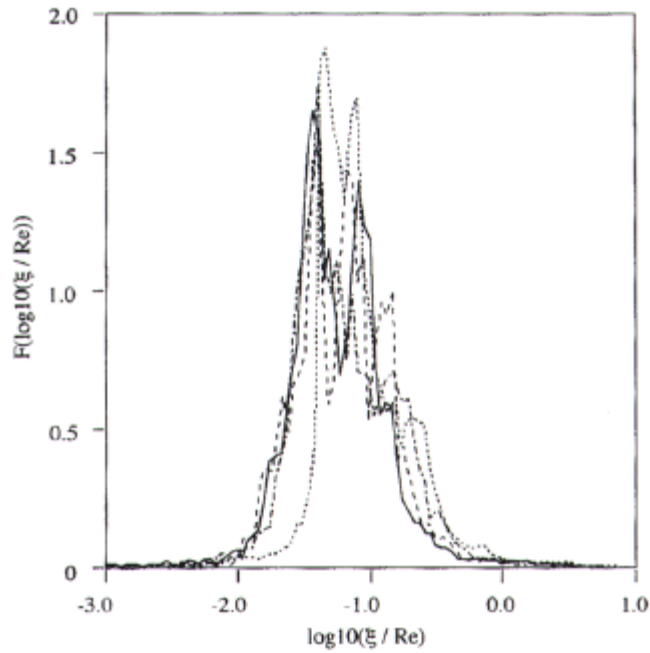


Figure 1.4. Probability distribution function of ξ/Re at $Re = 20, 40, 80$ and 160 (Zalc et al., 2001).

Alvarez et al. (2002) used computational particle tracking to create Poincaré sections that reveal the segregated regions found in the experiment and follow their shape change with the change in impeller velocity change. Homogeneity is measured by the percent of the flow domain occupied by tracer particles (V_i). It is observed that V_i increases with increasing Re (Figure 1.5).

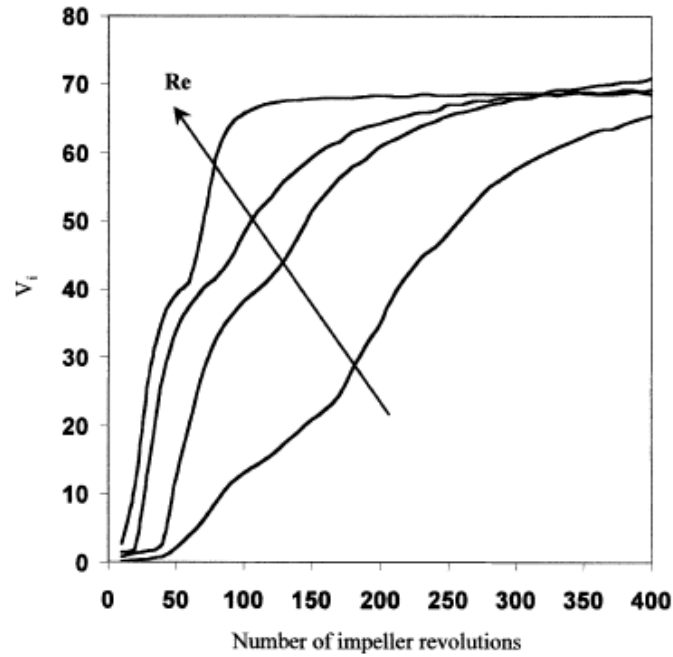


Figure 1.5. Percentage of the total volume invaded by tracer particles vs. number of impeller revolutions for $Re=20, 40, 80$, and 160 (Alvarez et al., 2002).

Examination of the arithmetic and volume averages of length of stretch and distribution of clusters and lines shows that mixing does not always improve with increasing Re . In fact, mixing efficiency reaches a plateau at high Re (Figure 1.6).

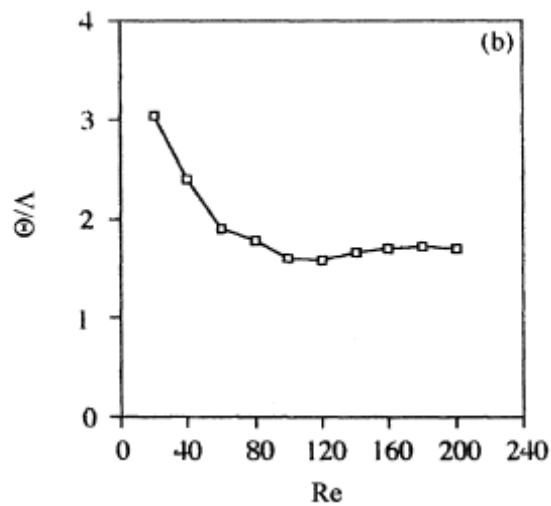


Figure 1.6. Mixing efficiency as a function of Re (Zalc et al., 2002).

Examining the effect of impeller geometry, number, and placement in a mixer as well as operating parameters like RPM allows researchers to explain the flow and mixing phenomena in simple mixing tanks. They are able to understand the chaotic mixing and segregated regions which occur in the mixer. The drawback to using simpler mixers is that the solutions obtained are not applicable to more complicated geometries like a twin-screw mixer. Simplifying assumptions used in these simulations do not account for flow irregularities produced by disturbances due to complex impeller geometry or chaotic mixing instabilities caused by complicated fluid rheology.

1.5.3 CFD in a model batch mixer

Binding et al. (2003) examined experimental and numerical simulation of dough mixing using a single couette. A fully filled geometry was used with a Newtonian and shear-thinning fluid. Streamlines and velocity vectors were very similar for the Newtonian and inelastic fluid cases. As seen in Figure 1.7 the experimental and numerical results have good agreement.

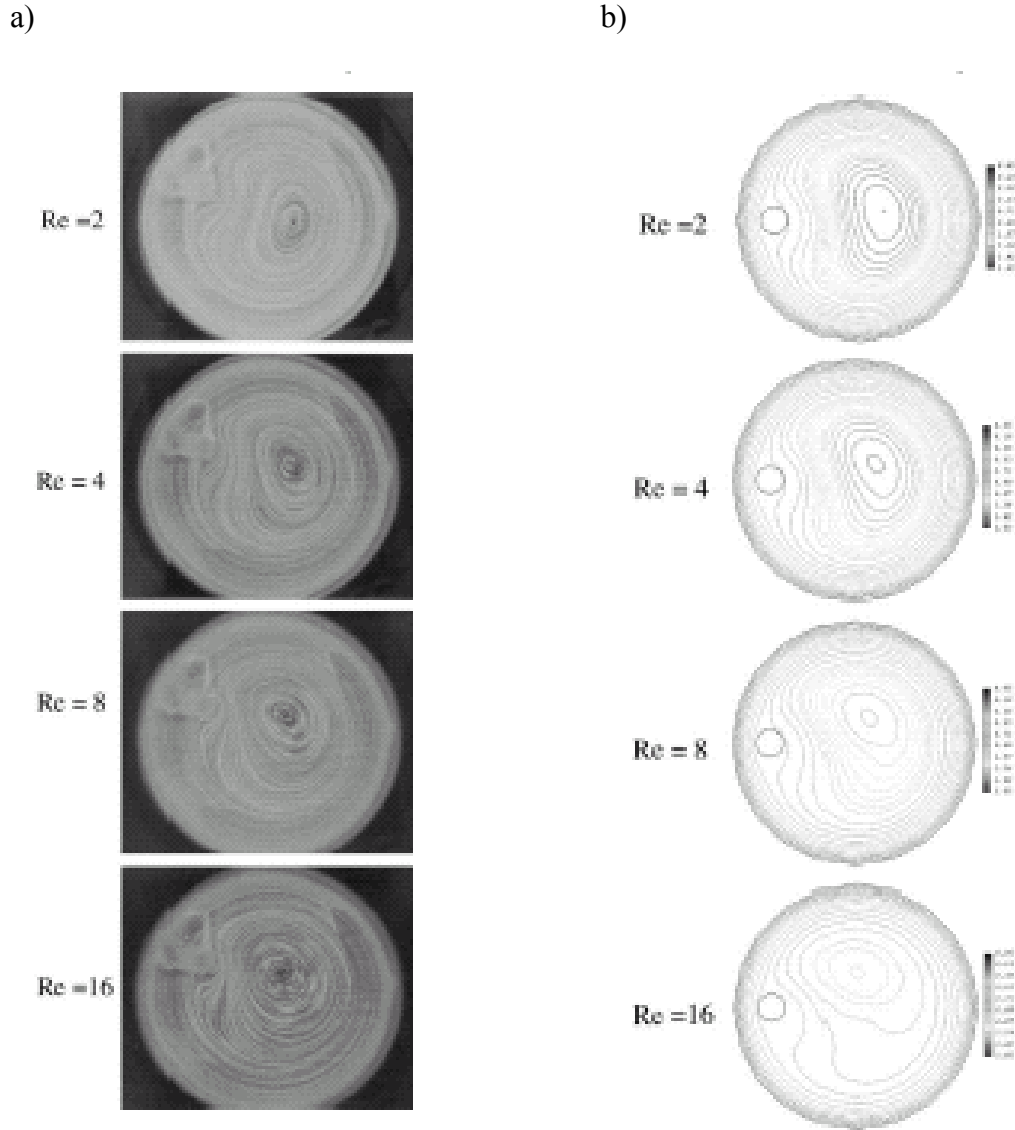


Figure 1.7. a) Laser speckle photographs for 1% CMC solution in the one-rod geometry at various Reynolds numbers, b) Stream functions for an inelastic material in the one-rod geometry at various Reynolds numbers (Binding et al., 2003).

Jongen et al. (2003) examined dough mixing in batch mixers using 2D numerical simulations. In order to distinguish between extensional flow, shear flow, and rigid body motion a parameter D is used. As defined in Equation 1.2, $D=-1$ for rotational flow, $D=0$ for shear flow, and $D=1$ for extensional flow.

$$D = \frac{1 - \mathcal{R}^2}{1 + \mathcal{R}^2}$$

Equation 1.2

where

$$\mathcal{R}^2 = \frac{\omega^2}{s^2}$$

Equation 1.3

This measure of deformation intensity is calculated from the second invariant of the strain rate tensor (s) and the rotation rate parameter (ω). D is only valid in 2D. Its 3D use is ambiguous and not able to be directly applied.

1.5.4 2D Numerical Simulation

Previous 2D work has successfully used FEM to simulate a twin-screw mixer and compare the resulting data with that obtained in a single-screw mixer (Connelly and Kokini, 2007). The complex fluid was a generalized Newtonian Carreau model; and isothermal conservation equations were solved via mixed Galerkin FEM.

Looking at velocity vectors in Figure 1.8 it can be seen that there are dead spots near the tip on the front of the blade and also on the back of the blade. The flow definitively follows the motion of the paddle. A symmetric velocity field is seen in the twin-screw mixer, with material flow between the right and left sides of the barrel and a dead zone in the region where the fluid direction changes. As fluid is forced through the small gap between the paddles, large pressure and velocity gradients are formed. This also affects axial fluid movement. This movement in the z direction would only be observed in a 3D simulation.

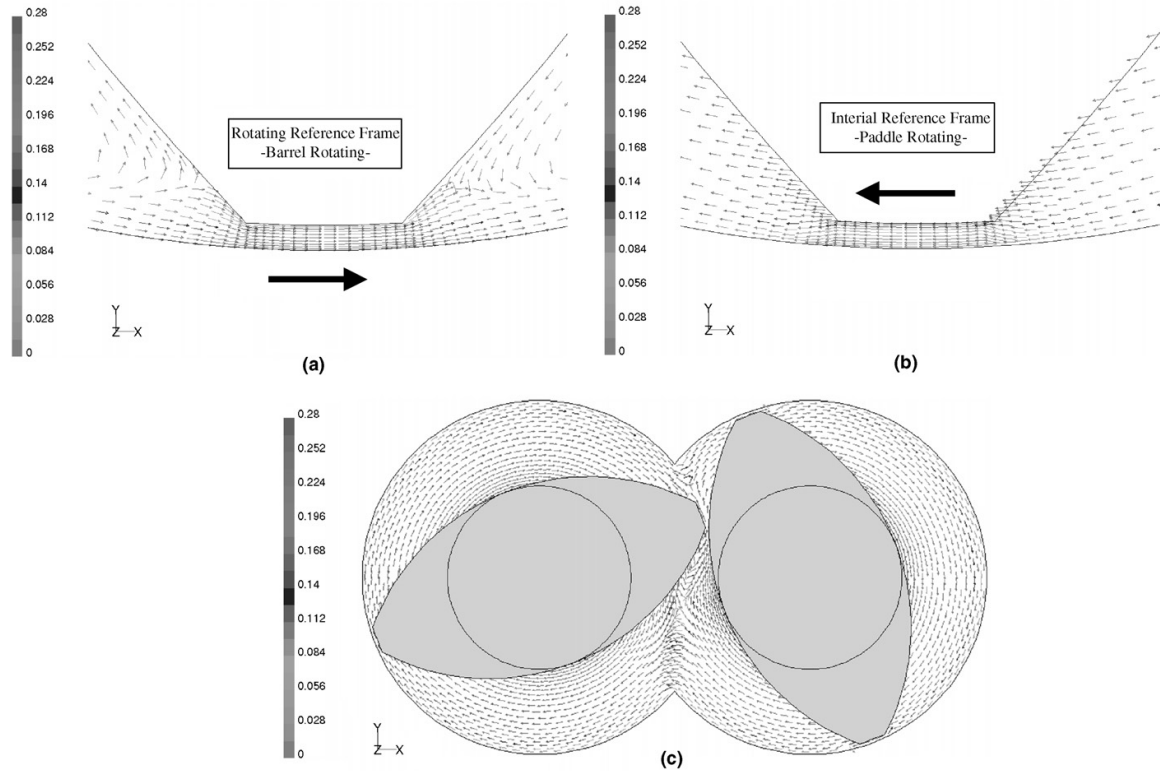


Figure 1.8. Velocity vectors showing the direction of the flow and colored by the magnitude of the velocity (cm/s). a) Single screw mixer rotating reference frame where the barrel is rotating counterclockwise and the paddle is fixed, b) Single screw mixer in the inertial reference frame where the barrel is fixed and the paddle rotates clockwise, c) Twin screw mixer after the paddles have turned clockwise 67.5° from the initial position. (Connelly and Kokini, 2007).

Mixing index values (Figure 1.9) along the length of the paddle are close to zero because the fluid is rotating as plug flow without deformation. Single and twin-screw mixers create mostly shear flow; and areas of elongation are larger and stronger in the twin screw mixer. Contours of mixing index (Figure 1.9) and shear stress (Figure 1.10) show that elongation and elevated shear stress are both found in the intermeshing region. This behavior in the twin-screw mixer produces better dispersive mixing, including bubble breakup, at lower speed compared to a single-screw mixer.

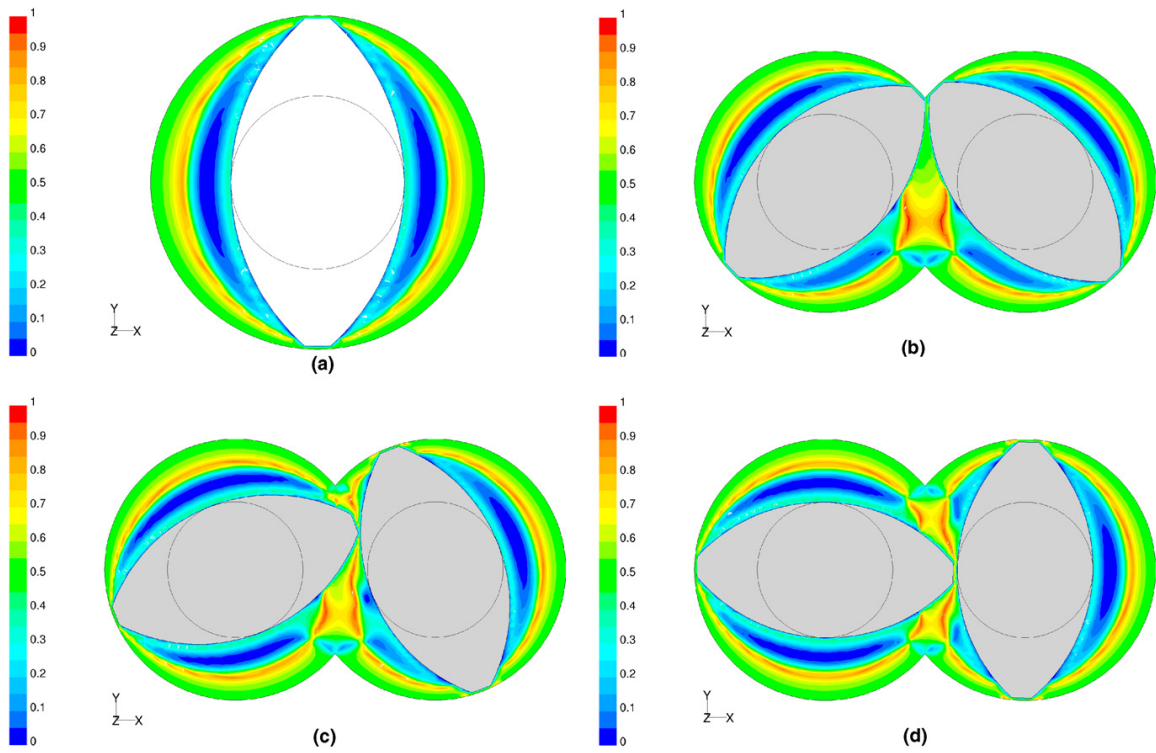


Figure 1.9. Mapping of the mixing index (λ_{MZ}) in a) the single screw mixer and the twin screw mixer at positions, b) 45°, c) 67.5°, d) 90° from the initial position where a value of 0 indicates pure rotation, a value of 0.5 indicates shear flow and a value of 1 indicates pure elongation. (Connelly and Kokini, 2007).

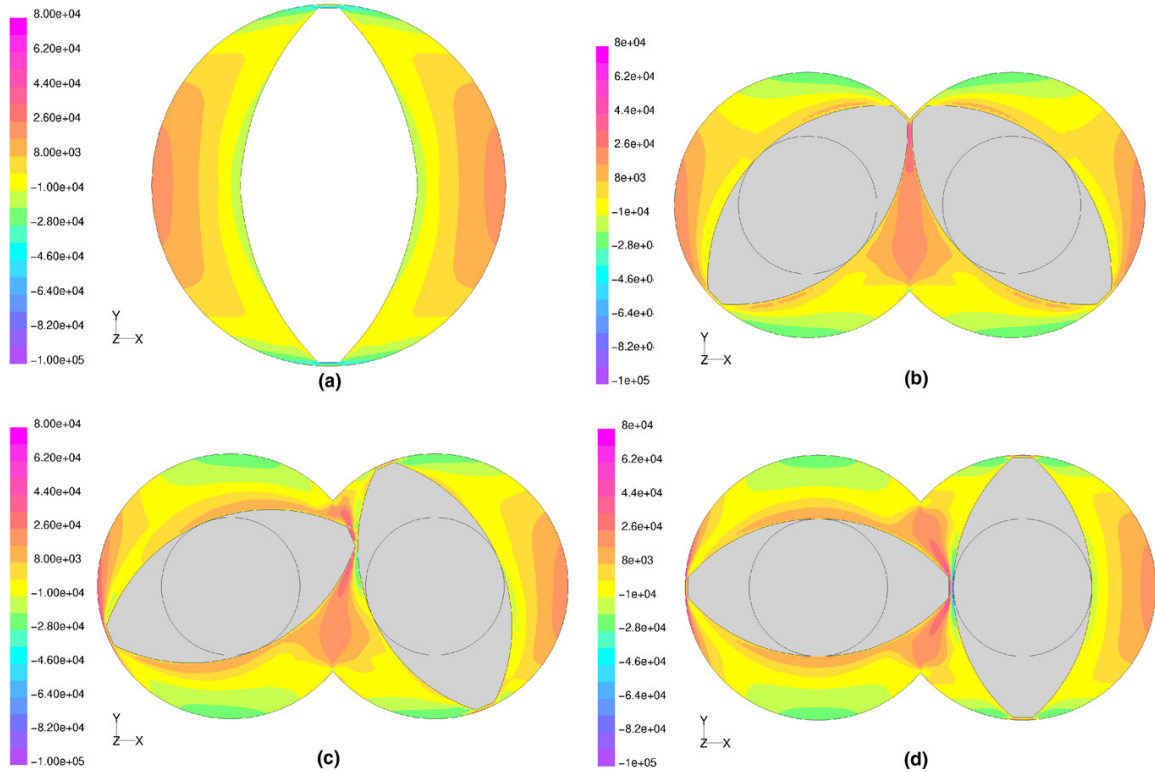


Figure 1.10. Mapping of the shear stress (τ_{12}) distributions where the units of stress are g/cm^2 in a) the single screw mixer and the twin screw mixer at positions b) 45° , c) 67.5° , d) 90° from the initial position. (Connelly and Kokini, 2007).

In Figure 1.11 and Figure 1.12 one can see the distribution of clusters initially found centered on the left and behind the paddle. Those particles initially in b1 (Figure 1.11) are distributed more effectively in the single screw mixer because of the continuous circulation which is interrupted in the twin screw mixer. This disruption also is seen in Figure 1.12 but accounting for the initial position of cluster b2 it aids in the distribution of particles.

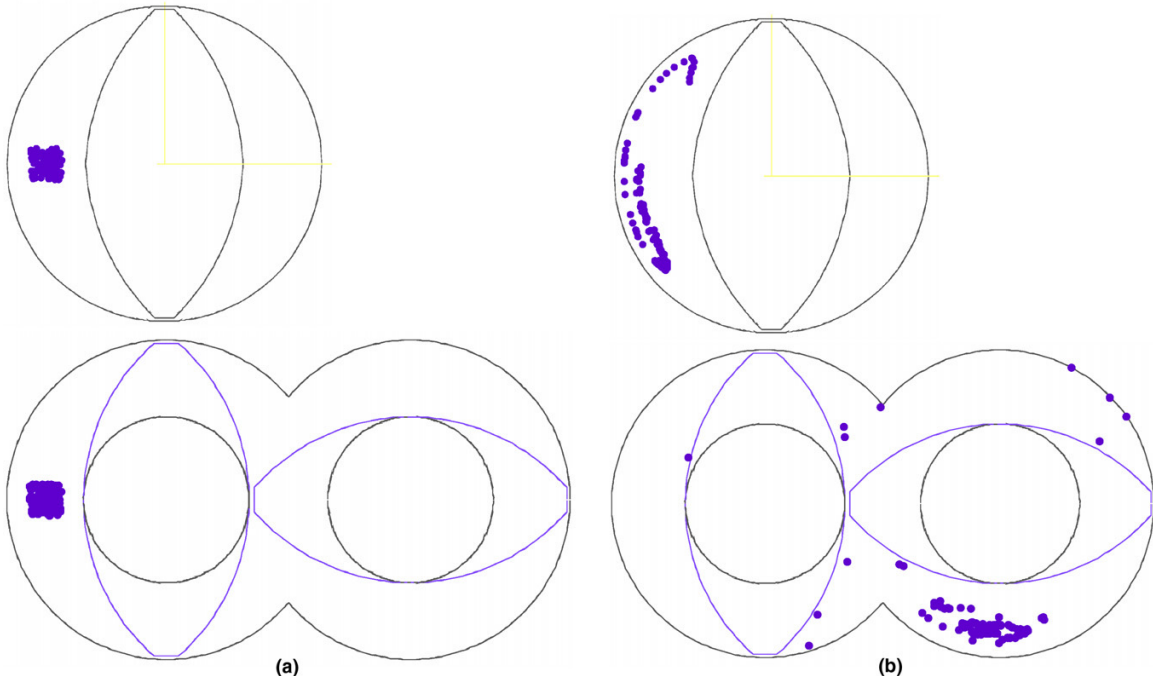


Figure 1.11. Particle tracking results showing the distributive mixing of a cluster (b1) of non-cohesive, material points initially centered in the leftmost section of the flow field a) initially, b) after 10 revolutions (Connelly and Kokini, 2007).

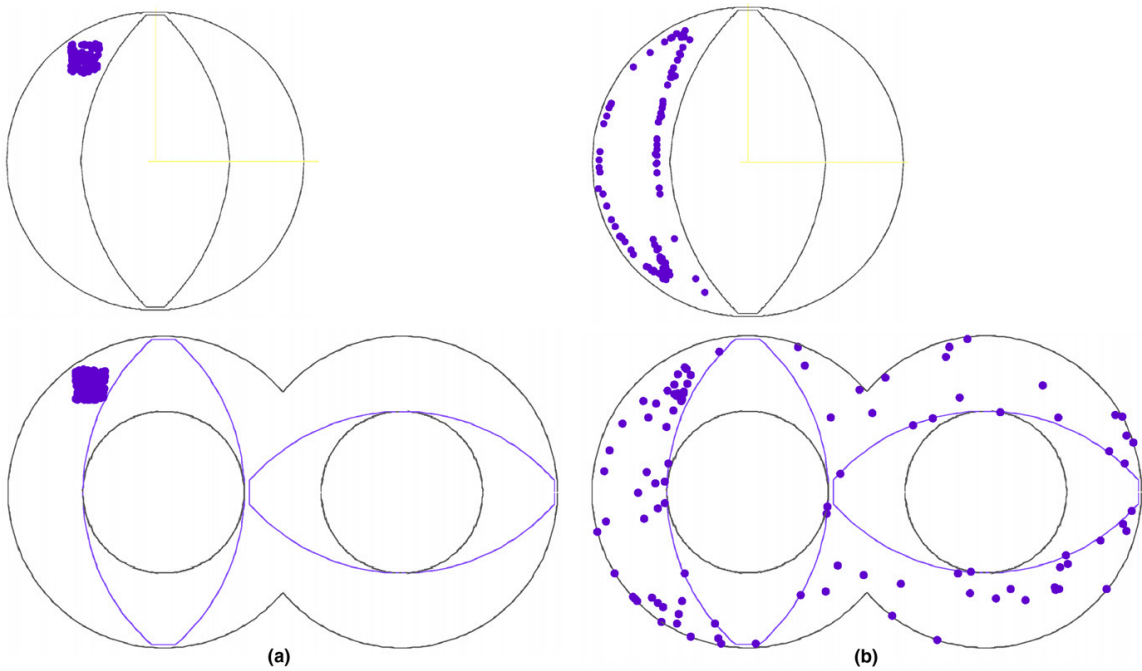


Figure 1.12. Particle tracking results showing the distributive mixing of a cluster (b2) of a non-cohesive, material points initially located behind the paddle in the leftmost section of the flow field a) initially, b) after 10 revolutions (Connelly and Kokini, 2007).

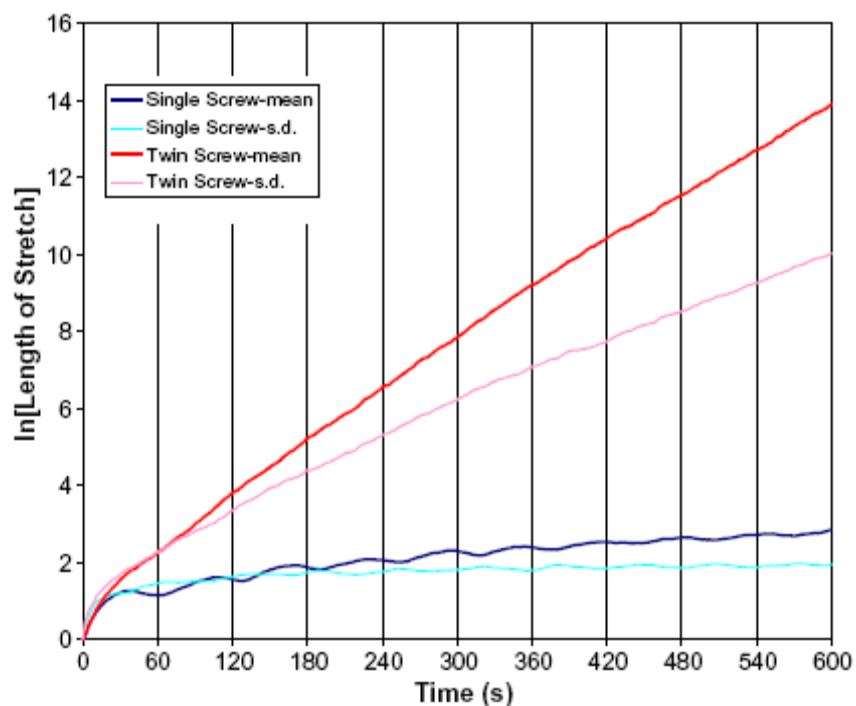


Figure 1.13. The mean and standard deviation of the length of stretch over 10 revolutions of the mixing paddles (Connelly and Kokini, 2007).

As shown in Figure 1.13 above, stretching in a single screw mixer is almost level while the length of stretch in a twin screw mixer increases exponentially. This increase is probably caused by folding which occurs in the region between the screws and is vital to efficient laminar mixing. Efficient mixing is also seen in Figure 1.14 where the time averaged efficiency remains above zero showing strong reorientation in the twin screw mixer.

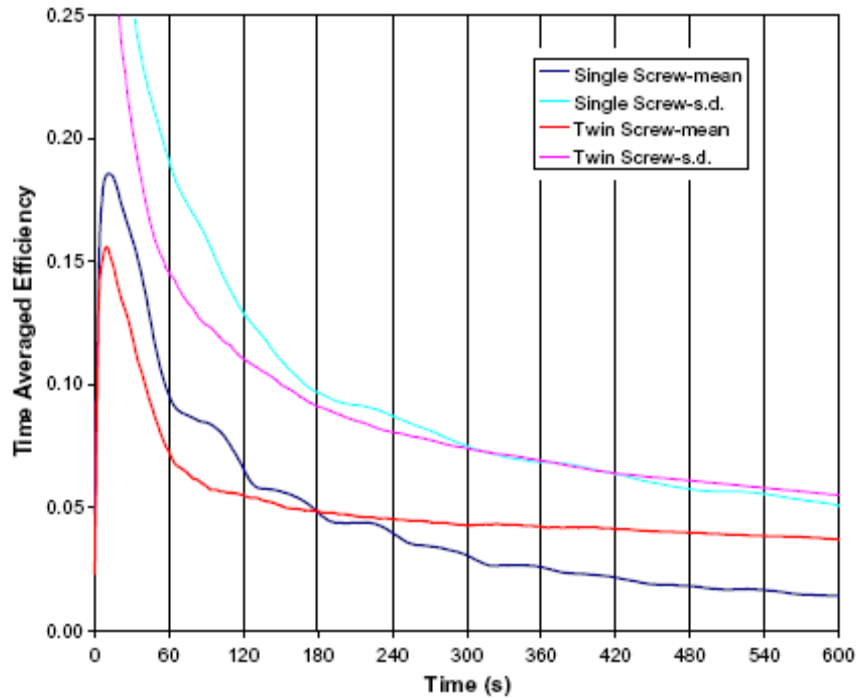


Figure 1.14. The mean and standard deviation of the time averaged mixing efficiency over 10 revolutions of the mixing paddles (Connelly and Kokini, 2007).

Areas of high mixing index values were larger with a viscoelastic fluid, showing increased elongation flow (Figure 1.15). Plug flow and areas of low mixing index increased with shear-thinning behavior. Viscoelasticity shifted areas of high shear stress ahead of the paddle and low shear stress behind (Figure 1.16). Increased shear stress and elongation lead to better dispersion ahead of the paddle, while shear-thinning behavior caused decreased shear stress near the paddle tip and increased dead zones, leading to decreased dispersion (Connelly and Kokini, 2004).

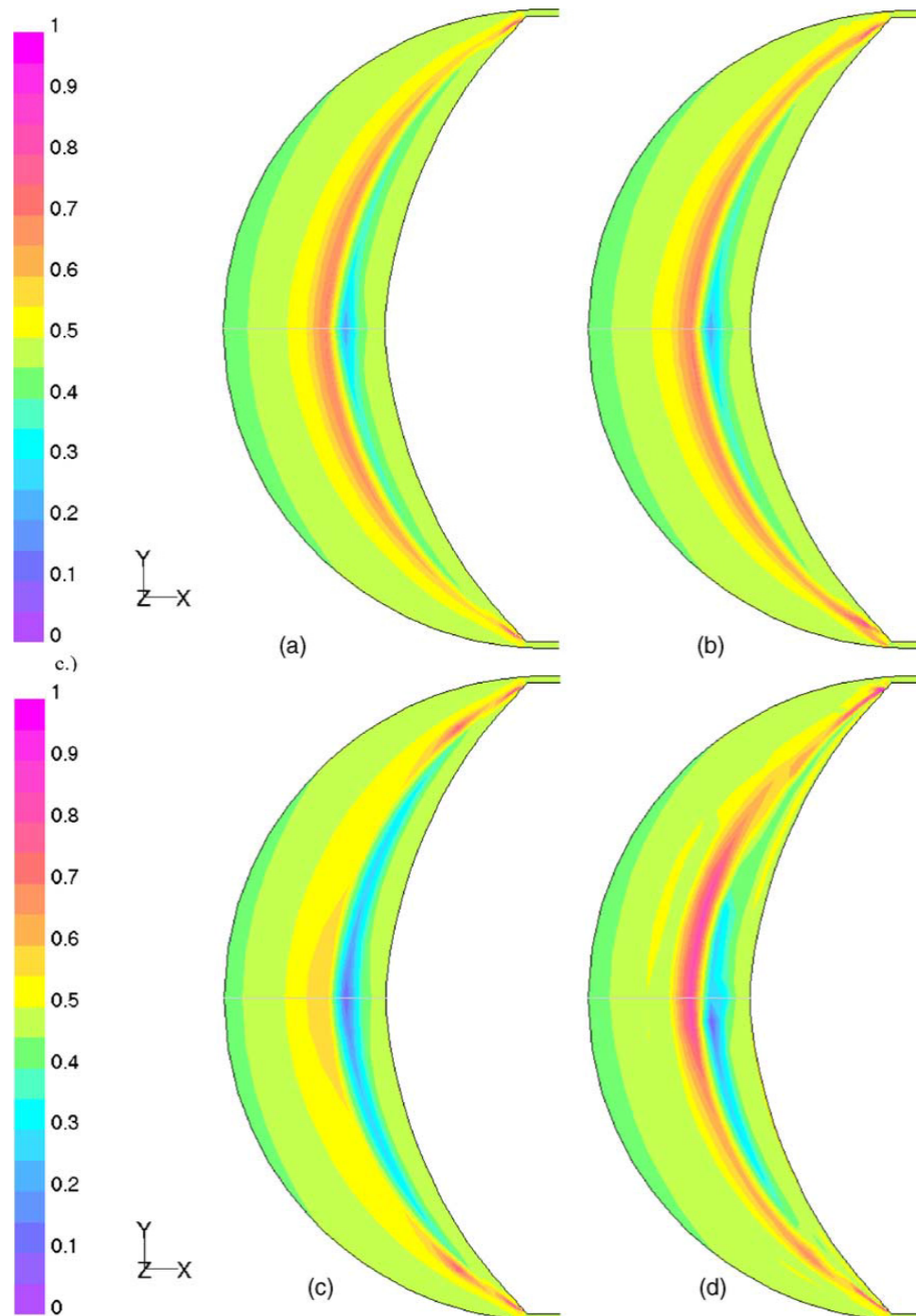


Figure 1.15. Manas-Zloczower mixing index distributions at 1 rpm of a) Newtonian, b) Oldroyd-B with relaxation time of 1.5 s, c) Bird–Carreau viscous, d) Phan-Thien Tanner fluid models (Connelly and Kokini, 2004).

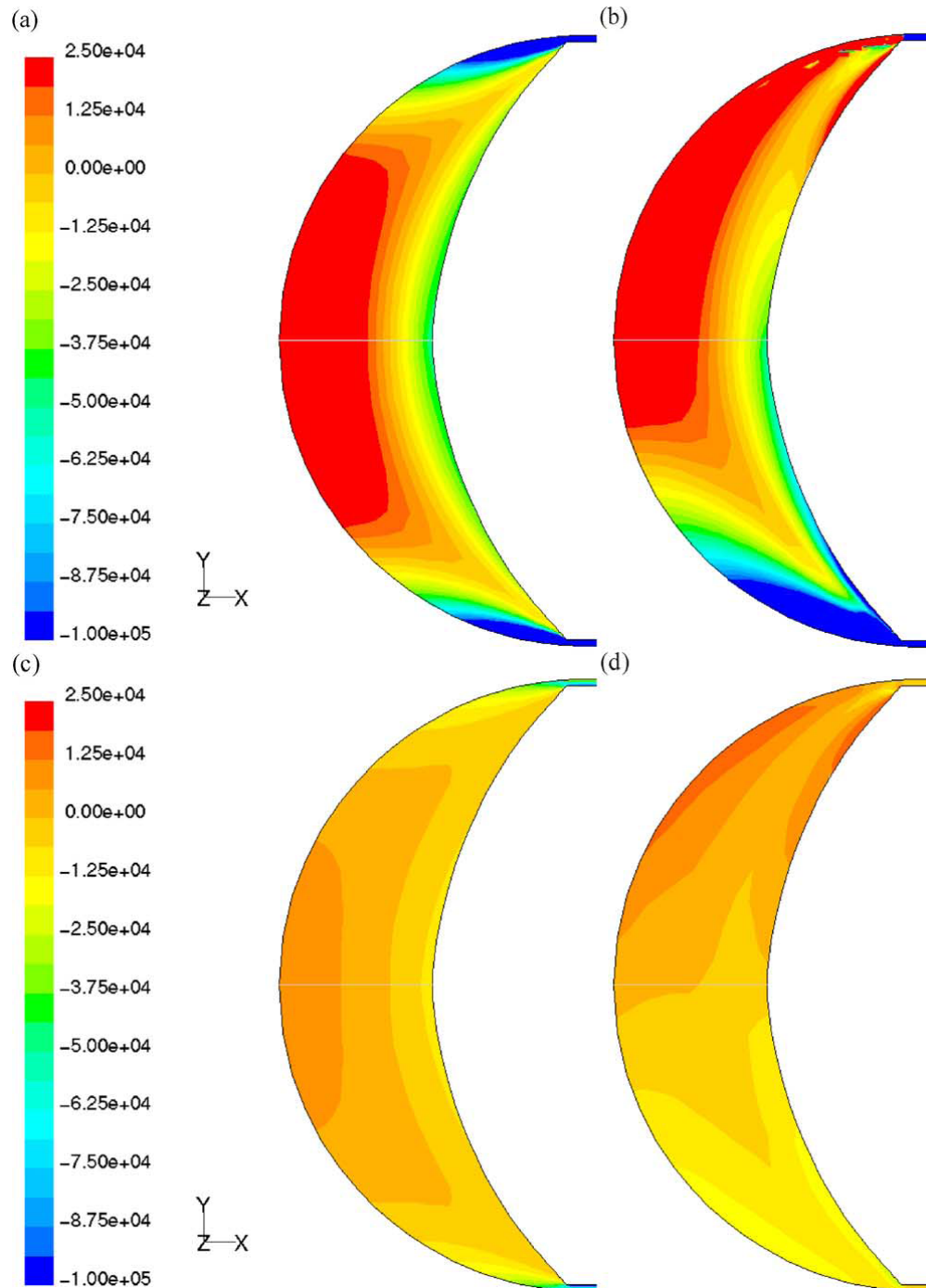


Figure 1.16. Shear stress (τ_{12}) distributions at 1rpm of a) Newtonian, b) Oldroyd-B with relaxation time of 1.5s, c) Bird-Carreau viscous, d) Phan-Thien Tanner fluid models where the units of stress are dyne/cm^2 (Connelly and Kokini, 2004).

1.5.6 3D Numerical Simulation in a Twin-Screw Mixer

Mixing efficiency is dependent on the geometry of the kneading section of the mixer including the stagger angle, width and number of kneading discs. Previous work has numerically examined 2D mixer geometries but to truly examine a time dependent 3D flow a time dependent 3D simulation must be performed. To simplify only one kneading block of several discs is used. Isothermal flow is an acceptable assumption because of the short time length considered. Boundary conditions included a developed velocity profile at the inlet and vanishing normal velocity and tangential force at the exit. A full stick condition is assumed at the barrel and screw surfaces and the mixing section is assumed to be fully filled. It is found that elements with a reverse geometry and larger number of discs increase the quality of mixing (Alsteens et al., 2004).

Experimental and numerical examination of Newtonian corn syrup mixing in a Readco continuous mixer was performed by Vyakaranam, et al. (2012). Validation of the 3D FEM simulation data was done by comparing experimental velocities obtained using LDA. Paddle stagger angle was found to create only local flow disruption, specifically affecting v_z . Global forward or reverse flow was not caused, in part, due to the constant inlet flow set at the boundary in the simulation. Experimental material flow rate varied only with screw speed. The FLAT configuration experienced the greatest v_z due to the straight fluid path formed by the parallel paddles in the center of the mixer. This is blocked by angled paddles in the 45F and 45R configurations with 45° staggered paddles forward and reverse, respectively. The FLAT configuration also showed greater pressure in the intermeshing region, indicating squeeze flow. Within the remaining volume fluid experiences axial transport in the FLAT and 45R simulations. In 45R backflow is seen in

the intermeshing region, while in 45F axial flow is seen. The lack of significant pressure variation indicates leakage flow as the transport mechanism.

Strong elongation flows, indicated by $\lambda_{MZ} > 0.7$, cause better dispersive mixing. This flow behavior is seen in the intermeshing region, above and below the paddle, and in the middle of the crescent area between the paddle and barrel wall. Thus the intermeshing region is important to dispersive mixing. Elongation flow is not seen between the paddle tips and the barrel wall; instead high shear rates are seen.

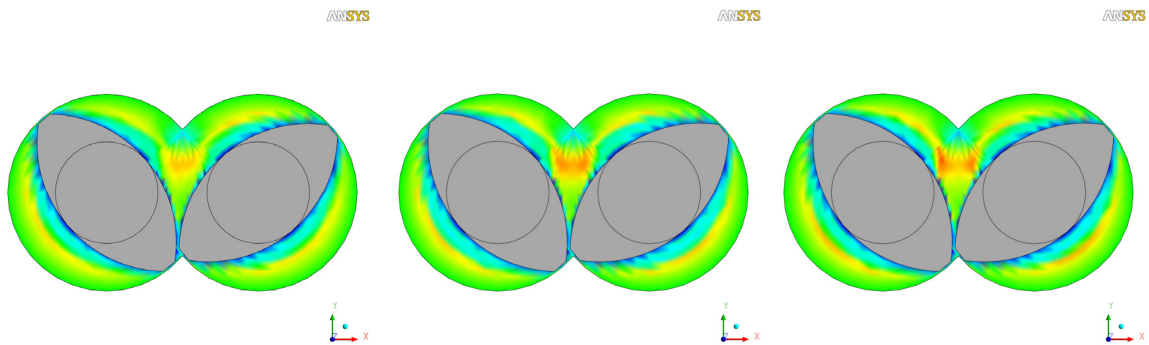


Figure 1.17. Contour maps of dispersive mixing index λ_{MZ} , over three XY cross-sectional planes at time step 4 for FLAT configuration at 100 RPM a) P1, b) P4, c) P8 . Legend – yellow to red shades show predominantly elongation flow, green shades are predominantly shear and blue shades are predominantly rotation (Vyakaranam, 2012).

Staggered paddles were shown to disrupt the axial flow and reduce elongational flow. Only the FLAT configuration allowed apparent squeeze flow in the intermeshing region (Figure 1.18) as the fluid passed between two paddles inducing motion in opposite directions. This effect was fragmented with the introduction of staggered paddles.

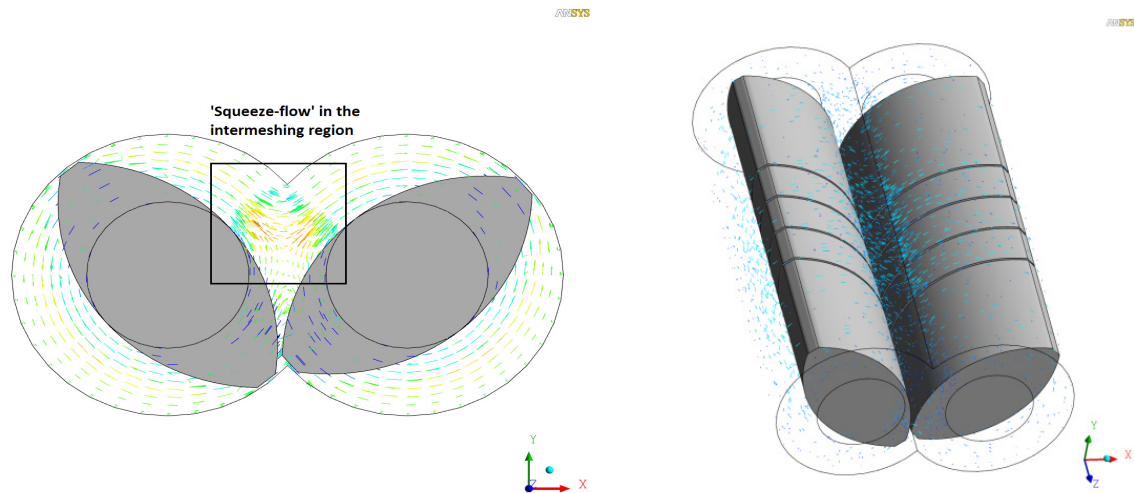


Figure 1.18. a) Illustration of ‘Squeeze flow’ in the intermeshing region between the paddle element surfaces and barrel wall surfaces causing a predominantly elongation flow, b) Velocity vector maps for the FLAT configuration at time step 4, 40° (Vyakaranam, 2012).

1.5.7 Scaling

Dimensional analysis is used to relate the geometry or operating conditions to the heat transfer possible or power needed by a machine. The corresponding relations are not universal because a dimension varies by ϕ , the flow and power requirement varies by ϕ^3 , while heat transfer characteristics will be scaled only by a factor of ϕ^2 . These difficulties have previously been avoided by dividing the variables considered into primary variables (screw diameter, flight height) and secondary variables (residence time, shear rates, power consumption, heat transfer). Then scaling primary variables will affect the secondary variables (Rauwendaal, 1987). This method has been used to scale single-screw extruders (Rauwendaal, 1987; Dhanasekharan and Kokini, 2003) using similarity in specific mechanical energy input and residence time distribution (Dhanasekharan and Kokini, 2003) and varying geometric parameters like L/D, screw diameter, channel depth or screw speed (Figure 1.19).

Geometry 1 (big)

$D = 3.5\text{ cm}$, $H = 1\text{ cm}$, $D/H = 3.5$, helix angle = 17.66° , $\varepsilon = 0.03\text{ cm}$, $L/D = 6$

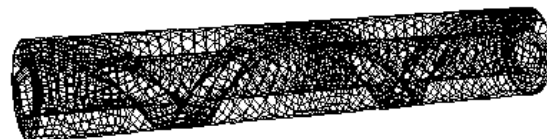


SME = 164.42 KJ/Kg

Average Residence time = 31.16 s

Geometry 2 (small)

$D = 1.6\text{ cm}$; $H = 0.381\text{ cm}$; helix angle = 40° ; $\varepsilon = 0.03\text{ cm}$; $L/D = 6$.



SME = 152.57 KJ/Kg

Average Residence time = 31.81 s

Figure 1.19. Demonstration of extruder scale-down (Dhanasekharan and Kokini, 2003).

1.5.8 Adaptive remeshing

Fictitious domain method is a mesh refinement relying on a single reference mesh (Bertrand et al., 2003). This allows simulation of a complex moving part geometry without remeshing for every time step as is necessary in classical finite element method. Internal parts are not meshed as such but are accounted for with time dependent control points where a kinematic constraint was imposed. These points can be updated with the kinematics of moving parts. This method allows the prediction of shear rate in the intermeshing zone and between the screws and the barrel. These gaps are very small and the position varies with time. Thus one wants to use mesh refinement based on a single mesh which can adapt locally (Figure 1.20). The initial 2D mesh for a twin screw extruder is shown in Figure 1.21. When comparing the resulting simulation values to experimental values (Figure 1.22) a good agreement is found. Giguere et al. (2006) used the method shown here to simulate a 3D helical ribbon mixer geometry.

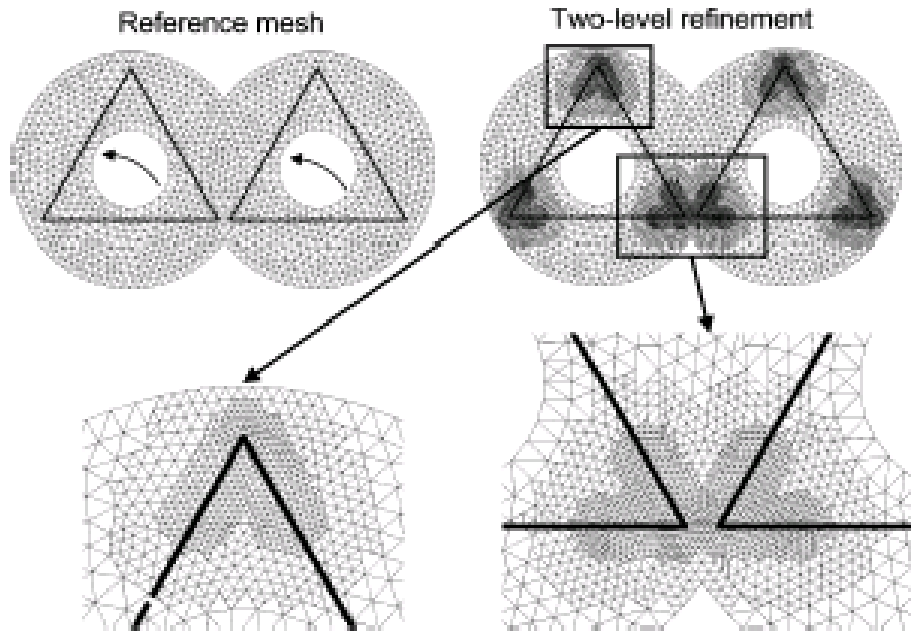


Figure 1.20. Two-level adaptive mesh refinement procedure in the vicinity of the gaps (Bertrand et al., 2003).

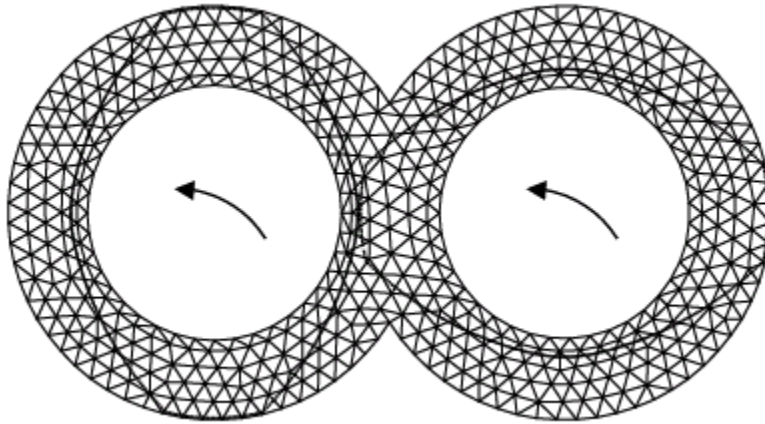


Figure 1.21. Reference mesh for 2D twin-screw extrusion, before adaptive remeshing (Bertrand et al., 2003).

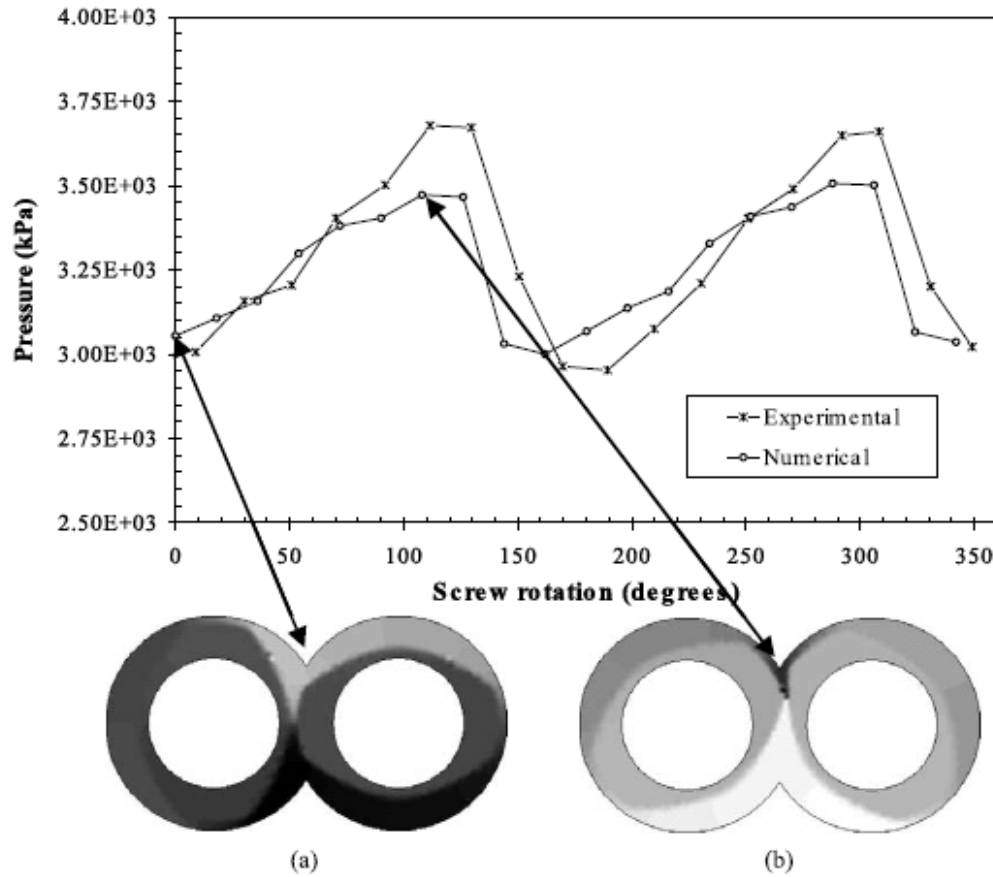


Figure 1.22. Variation of pressure with screw position. Simulated values from adapted mesh (Bertrand et al., 2003).

1.5.9 Mesh superposition

Mesh superposition allows the use of a single mesh for the fluid domain. This eliminates the need to remesh the geometry for each time step. Separate meshes are created for the barrel (fluid) and paddle (solid) zones. These are then superimposed. When greater than 60% of a barrel element is overlapped by the paddle, the element is considered solid and is assigned the velocity of the moving part by the addition of a penalty term H into the equation of motion (Equation 1.4). $H=0$ outside the moving part and $H=1$ inside.

$$H(\mathbf{v} - \bar{\mathbf{v}}) + (1 - H)(-\nabla p + \nabla \cdot \mathbf{T} + \rho \mathbf{g} - \rho \mathbf{a}) = 0$$

Equation 1.4

where H is a step function, \mathbf{v} is the velocity, $\bar{\mathbf{v}}$ is the local part velocity, p is the pressure, \mathbf{T} is the extra stress tensor, $\rho \mathbf{g}$ is the volume force, and $\rho \mathbf{a}$ is the acceleration term.

Fluid leakage into the solid paddle is a concern due to the fact that the solid-liquid boundary can not be precisely determined (Jongen, 2000). This is taken into account by the addition of a very small compression factor ($\beta=0.01$) to the continuity equation (Equation 1.5).

$$\nabla \cdot \mathbf{v} + \frac{\beta}{\eta} \Delta p = 0 \quad \text{Equation 1.5}$$

where η is the local viscosity.

1.5.10 Effect of Stagger Angle

Ishikawa et al. (2001) examined the effect of stagger angle and disk width on pressure, temperature, stress, and area stretch distributions in the kneading section of a corotating twin screw mixer. They found that a paddle configuration with a strong conveying influence such as FFF (forward staggered) produced a smaller pressure gradient (Figure 1.23) than one with a backward flow such as BBB (backward staggered). Temperature distributions (Figure 1.24) were also influenced by paddle configuration. FFF and NNN (neutral) produce low temperature distributions but BBB increases temperature because of the backward flow.

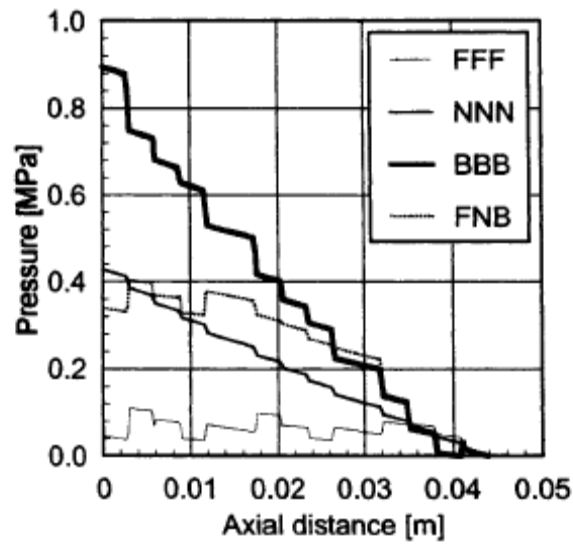


Figure 1.23. Pressure distributions in the axial direction with different stagger angles (Ishikawa et al., 2001).

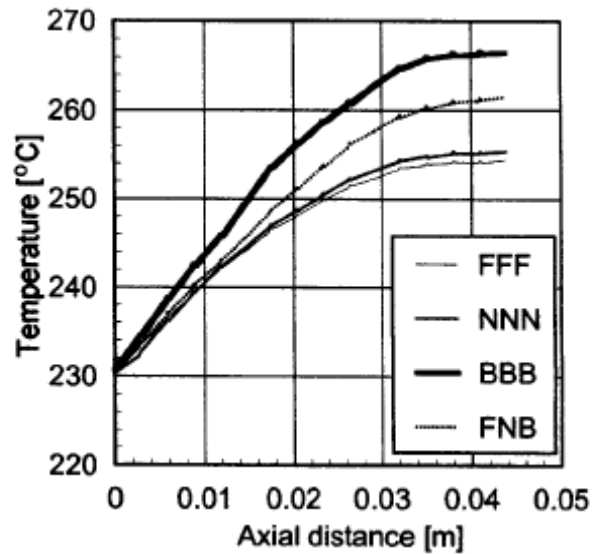


Figure 1.24. Temperature distributions in the axial direction with different stagger angles (Ishikawa et al., 2001).

Dispersive mixing is examined by using stress (Figure 1.25). The desired combination of high stress and a narrow distribution curve is found for FNB (forward, neutral, backward). This denotes the best dispersive mixing. Distributive mixing is measured by area stretch as seen in Figure 1.26. Large stagger angles such as those found

in FNB positively affect distributive mixing. Also the distribution function shows low values at low area stretch and a broad distribution. Thus FNB has the best overall mixing capacity.

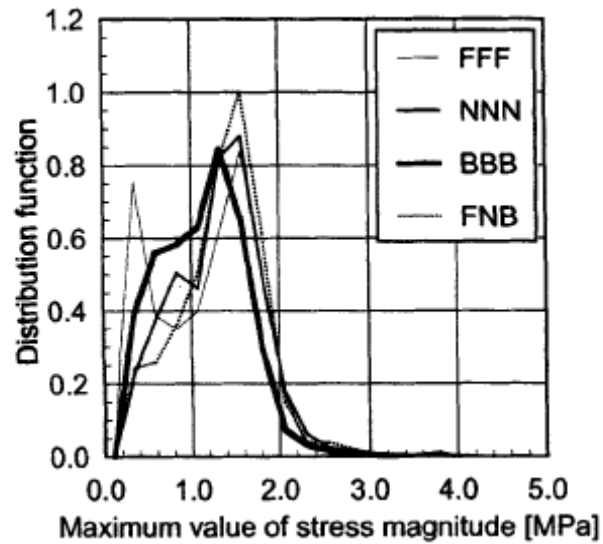


Figure 1.25. Distributions of stress magnitudes with different stagger angles (Ishikawa et al., 2001).

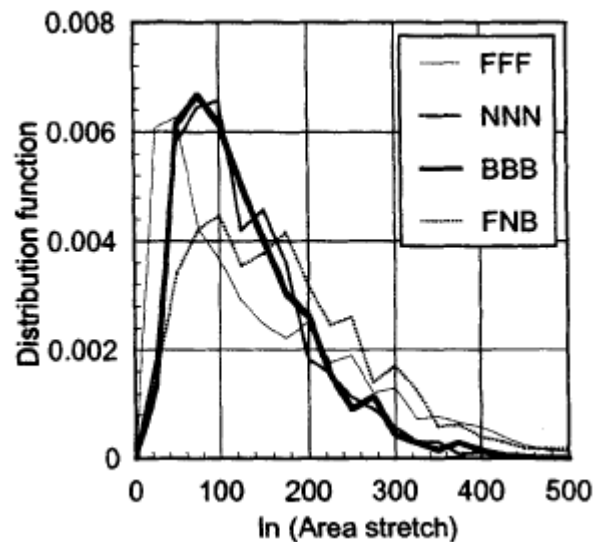


Figure 1.26. Distributions of area stretch with different stagger angles (Ishikawa et al., 2001).

1.5.11 Extension Rate Fundamental Studies

Extension rate distribution research, although important to mixing, has not been performed in complex geometries. Simplified geometries used include abrupt contractions (Debbaut and Crochet, 1988; Keunings and Crochet, 1984; Debbaut et al., 1988), abrupt expansions (Dheur and Crochet, 1987), flow around a sphere, and circular die swell (Debbaut and Crochet, 1988). It is difficult to separate extension rate from shear because of combined shear and extension flow. Debbaut and Crochet (1988) thoroughly explored extension rate theory using both generalized Newtonian (White-Metzner and Bird-Carreau) and viscoelastic (upper-convected Maxwell) fluid models. They determined that extension rate can be defined as six times the third invariant divided by the second invariant of the rate of strain tensor.

Wang and James (2011) estimated extensional flow resistance using a dilute polymer solution in a lubricated, converging microfluidic channel. Nearly constant viscosity fluids were used. Microfluidic systems provide an opportunity to obtain structure-property relations for complex fluids as they produce low Reynolds and Peclet numbers over a wide range of Deborah and Weissenberg numbers. Steady extensional flow was achieved at low Reynolds numbers (Re) and moderate Hencky strain. Apparent extensional viscosity was a function of strain rate and was estimated as the difference between the experimental pressure drop and calculated pressure drop of shearing the core fluid.

Oliveira et al. (2007) found the extensional rate at the center line of the microchannel to be constant with increasing channel aspect ratio, allowing them to calculate extensional viscosity. Arratia et al. (2008) used a polymer solution which

experienced slower filament break-up. This enabled them to estimate extensional viscosity from a normal stress balance at the interface.

Extensional rate increased in the direction of flow, with a maximum at the convergent channel entrance, and decreased toward the exit. Extensional elasticity was generated early, when local $De > 1$ upstream. Elastic stresses resulted in a higher than Newtonian pressure drop. This difference was used to estimate extensional viscosity.

For two phase flows, final product morphology is dependent on mixer design and operating conditions (Stegeman, et al., 2002). An essential function is the deformation and break-up of droplets. The Grace curve (Grace, 1982) relates the viscosity ratio to the critical capillary number. The Capillary number is the ratio of viscous to interfacial forces (Taylor, 1934). It is used to determine the necessary shear to elongation rate for binary break-up of a single spherical droplet in quasi-steady homogeneous Newtonian flow. The Grace curve has limited use in industrial applications where the capillary number is much larger than the critical capillary number and the flow field is not homogeneous (Stegeman, et al., 2002).

Bubbles are able to break in transient flow fields while remaining unbroken in steady flows of similar strength. A droplet will break if its length is greater than the critical sustainable length for a sufficient period of time. Droplet deformation in a time-dependent experiment is a function of rheological properties and densities of the two fluids, instantaneous flow rate, and instantaneous dimensionless droplet length. A small droplet deforms more slowly until steady state is reached. A slightly larger droplet elongates faster with time until break-up (Stegeman, et al., 2002). A specific elongation rate was used. Once a given steady length was achieved, oscillation was imposed. A

droplet followed the oscillation or elongated faster with time until it deformed to coincide with the continuous phase.

Models of droplet deformation corresponded well with experimental trends, but under-predicted deformation, did not predict break-up, and predicted much greater droplet length. Droplets with an initially elongated shape had much smaller critical capillary numbers. For low viscosity ratio droplets, the initial length effect was negligible because the shape was already elongated. At a fixed viscosity ratio, break-up depended on initial length and a decreased capillary number. Adding elongational flow caused the break-up of high viscosity ratio droplets. A time and temperature dependent viscosity ratio led to initial droplets with deviant (non-spherical) shapes.

The Manas-Zloczower mixing index has been used previously as an indicator of extensional flow (Cheng and Manas-Zloczower, 1990). Although the values point to flow type, they do not offer quantitative information on extension rate distribution in a mixer. Mixing index values between 0.5 and 1 show mixed shear and elongation flow. The contribution of elongation flow is increased as the value approaches one. This flow behavior aids in bubble breakup (Grace, 1982; Bentley and Leal, 1986; Meijer and Janssen, 1994; Vyakaranam, 2012).

1.5.12 Bubble Breakup and Flow Type

Emin and Schuchmann (2013) performed both experimental and numerical work with starch extrusion. The researchers found that increasing screw speed and oil content increased the instance of bubble coalescence through drainage probability and likelihood of bubble collision. Thus increasing screw speed did not lead directly to smaller bubbles due to competition between increasing break-up and coalescence. In contrast, increasing

material feed rate increased smaller droplets due to decreased probability of coalescence combined with increased blend viscosity. They also found that the use of reverse kneading blocks increased the number of particles with high maximum capillary ratio, leading to dispersive mixing.

Bubble break-up in a practical mixing device resulted from elongated threads which break into small drops, rather than large drops breaking stepwise into smaller drops (Janssen and Meijer, 1993). Transient mechanisms resulted in smaller droplets and finer morphology with higher viscosity ratios. They found that 2D elongation was more effective for bubble break-up than simple shear flow. Thus critical capillary number was less for a thread than a drop; and increasing extension rate produced a thinner thread prior to break-up, resulting in smaller drops.

Stone et al. (1986) examined deformation of a liquid drop in a four-roll mill. They found that this deformation was dependent on initial drop shape and viscosities of the continuous and droplet liquids. The effect of elongation ratio on the relaxation and break-up process is shown here for two viscosity ratios (Figure 1.27). When the elongation ratio is not too large, drop length shortens before breakup. It is apparent that relaxation is slower for the higher viscosity ratio. Drops become increasingly elongated as they approach the behavior of a fluid element in linear flow.

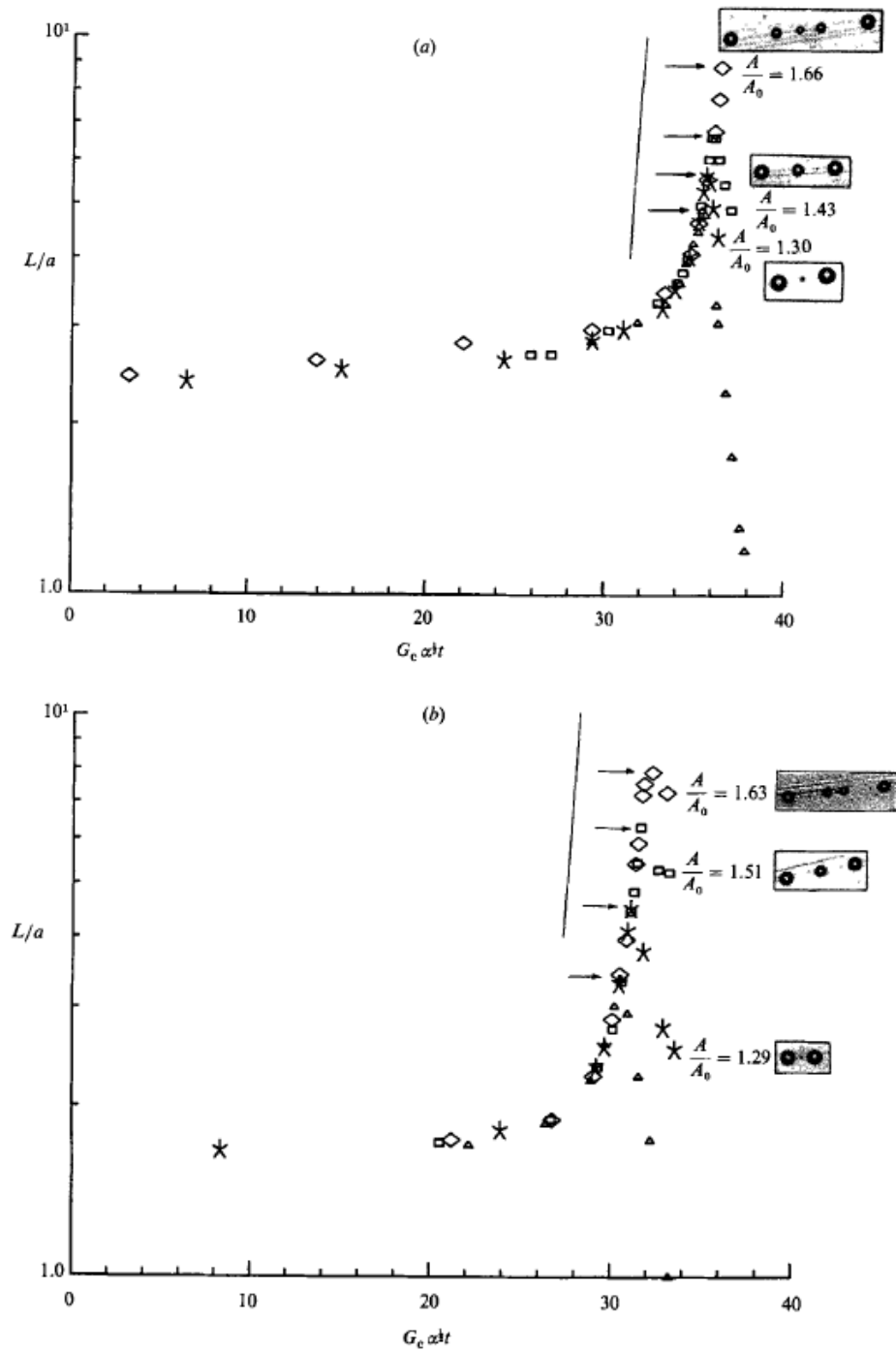


Figure 1.27. The effect of L/a on the relaxation and breakup process. a) $A = 0.018$, b) 0.47 . The horizontal arrows indicate when the flow is stopped. Data points for each experiment then continue until the first fragment separates from the main drop. A/A_0 denotes the fractional increase in interfacial area due to the fragmentation. The solid, almost vertical line indicates the rate at which a fluid element stretches in the linear flow, Δ , $\alpha = 1.0$; \square , 0.8 ; $*$, 0.6 ; \diamond , 0.4 (Stone et al., 1986).

A similar process of drop break-up is seen for both flow types shown in Figure 1.28, although $\alpha=0.2$ is largely shear-dominated flow and $\alpha=0.6$ approaches extensional behavior. At the point where flow stops, both drops are elongated and end pinching is observed with bulbous ends growing longer until they pinch off from the center thread.

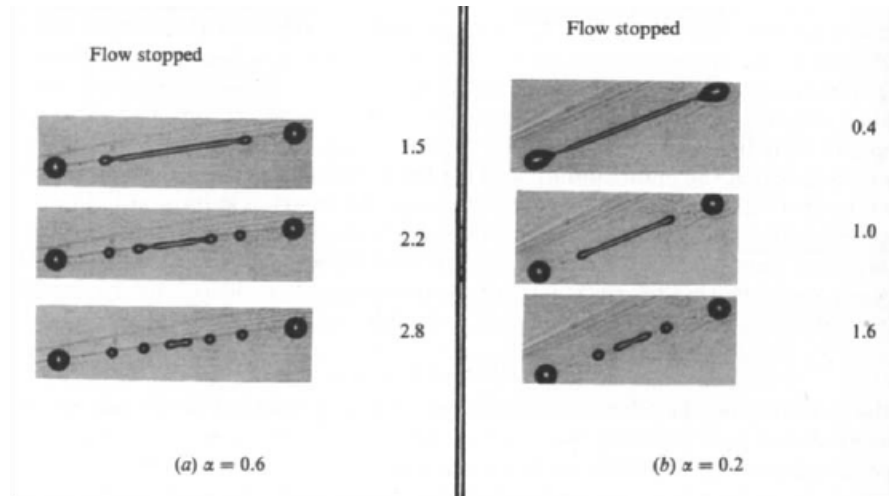


Figure 1.28. The effect of flow type on elongation process and on subsequent relaxation and breakup phenomena. Viscosity ratio is held constant, $\lambda=0.09$, a) $\alpha=0.6$, $G_c=0.224\text{s}^{-1}$, b) $\alpha=0.2$, $G_c=0.33\text{s}^{-1}$ (Stone et al., 1986).

When examining elongation ratio versus viscosity ratio, Stone, et al. (1986) found an area of uncertainty between the largest elongation ratio capable of allowing a drop to return to its relaxed state and the smallest ratio where break-up occurred upon flow stop (Figure 1.29).

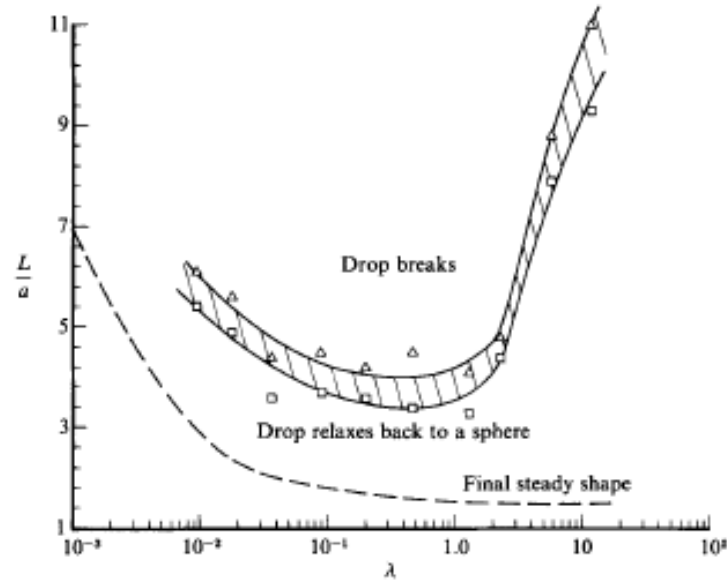


Figure 1.29. Critical elongation ratio necessary to ensure breakup, following an abrupt halt of the flow, as a function of viscosity ratio. Triangles denote the smallest L/a for which a drop was observed to breakup. Squares denote the largest L/a for which a drop relaxed back to a sphere. The shaded region denotes the uncertainty in the critical elongation ratio. The dashed line indicates the L/a values of the final steady shapes (Stone et al., 1986).

Vyakaranam and Kokini (2012) investigated the effect of flow type on bubble breakup using a Newtonian fluid in a Readco continuous mixer. Flow type was determined based on the Manas-Zloczower mixing index. The researchers found that, consistent with earlier studies (Grace, 1982; Khakhar and Ottino, 1986), extensional flows are important in breaking bubbles during mixing. Three mixer configurations were used, FLAT, 45F, and 45R where the consecutive paddles were parallel and at 45° to each other. Mean critical capillary number lies between the critical limits for breakup in shear and elongational flows (Figure 1.30). Mixed flow is the dominant type for bubble break-up.

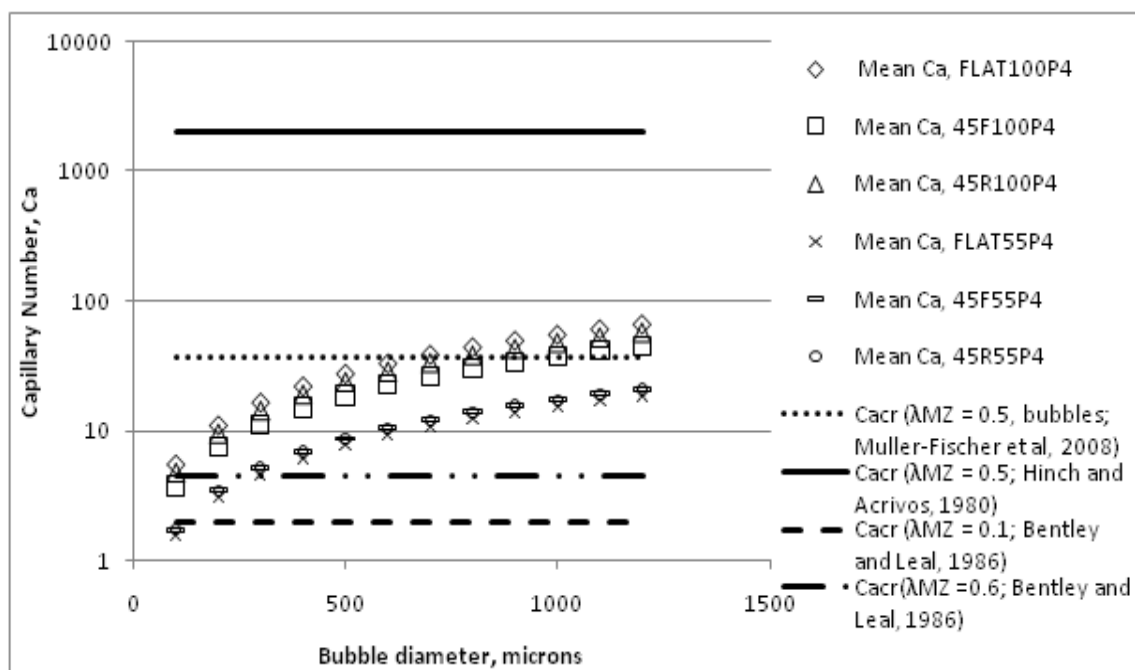


Figure 1.30. Mean Ca in the mixer vs $Cacrit$ Bubble breakup is possible only in elongation flow regions (Vyakaranam and Kokini, 2012).

Vyakaranam and Kokini calculated critical capillary number and maximum stable bubble diameter and compared the values with experimental data for Newtonian corn syrup. Predicted maximum stable bubble diameters were approximately half of the experimental mean values when the mixing index was 0.6 (Figure 1.31). The predicted values were even lower when the mixing index was 1. This gap is due to the fact that under the right conditions, of flow type and flow strength, break-up is dynamic and a mean value is an indicator, not an exact representation. The process was also affected by residence time of the bubble in the mixer compared to the time necessary for break-up. In pure elongational flow the mean shear rate was larger than the necessary flow strength to obtain these bubbles. In simple shear flow the mean shear rate was only a fraction of that needed, while in mixed flow twice the necessary shear rates were obtained at 100 rpm, and half the necessary shear rates were obtained at 55rpm (Figure 1.32).

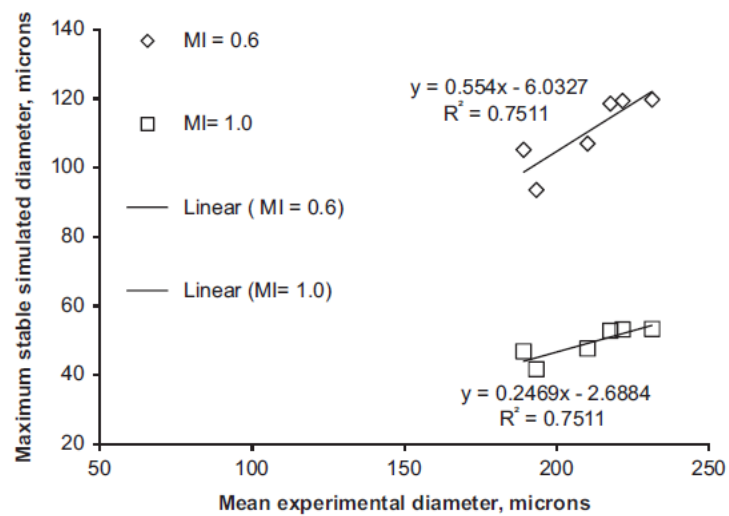


Figure 1.31. Mean bubble diameter vs. simulated maximum stable bubble diameter as a function of dispersive mixing index (Vyakaranam and Kokini, 2012).

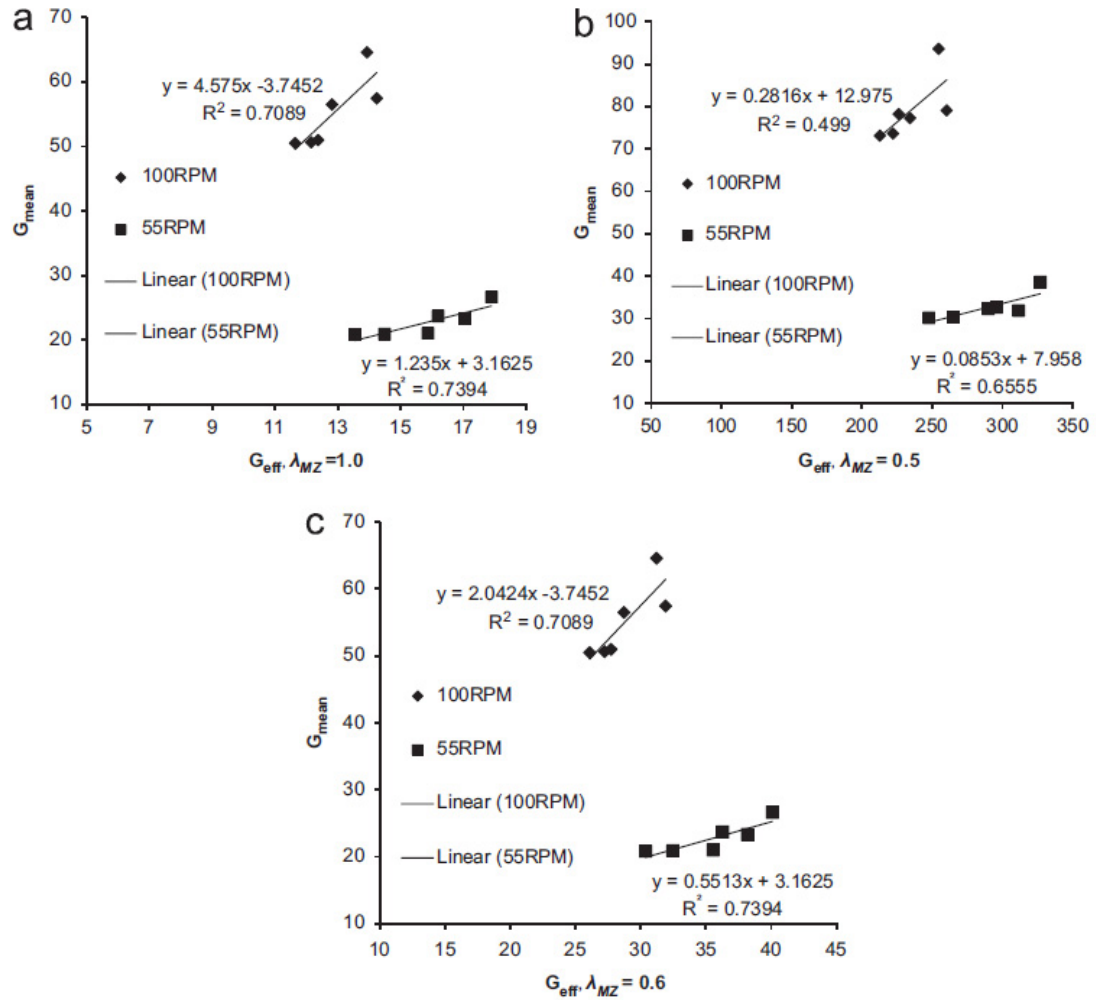


Figure 1.32. Effective shear rate vs. simulated mean shear rate assuming flow type a) pure elongation $\lambda_{MZ}=1$, b) simple shear $\lambda_{MZ}=0.5$, c) mixed flow $\lambda_{MZ}=0.6$ (Vyakaranam and Kokini, 2012).

1.6 Research Methods

1.6.1 Numerical Simulations

The Polyflow program group (ANSYS, Inc.) was used to perform numerical simulations. This includes a mesh generator: Gambit, FEM solver: Polyflow, and graphics post-processor: CFX-Post. Simulations were run on a Dell Precision 690 workstation with Dual Core Xeon processors and 16 GB RAM.

Polyflow is a finite-element CFD program where simulations can be isothermal or non-isothermal, 2D or 3D, and steady-state or time dependent. It solves the equations of conservation of mass and momentum with constitutive equations. This set is solved in a coupled form where velocity and pressure variables are solved with the stress or in a decoupled form that uses an iterative method to solve for velocity and pressure while treating the stress tensor separately. Polyflow has been used in previous research in our lab examining flow, mixing, and extruder scale-up (Dhanasekharan and Kokini, 2000, 2003; Connelly and Kokini, 2003, 2004, 2006a, 2006b, 2007; Ashokan, 2008; Vyakaranam, 2012; Vyakaranam and Kokini, 2012; Vyakaranam et al., 2012)

1.6.2 Fluid Rheology

Increasingly complex fluids have viscosities are divided into Newtonian, power-law, and viscoelastic relations. Newtonian and power-law fluids are collectively generalized Newtonian fluids and their stress tensor is given in Equation 1.6. Newtonian fluids have a constant viscosity (Equation 1.8). The viscosity of power-law fluids is a function of shear rate (Equation 1.9).

$$\mathbf{T} = \eta \mathbf{D}$$

Equation 1.6

where \mathbf{D} is the rate-of-deformation tensor and η is a here function of local shear rate $\dot{\gamma}$ (It can also be a function of temperature).

$$\dot{\gamma} = \sqrt{2tr(\mathbf{D}^2)}$$

Equation 1.7

$$\eta = \eta_0$$

Equation 1.8

where η_0 is the zero shear rate viscosity

$$\eta = K(\lambda \dot{\gamma})^{n-1}$$

Equation 1.9

where K is the consistency factor, λ is the natural time, and n is the power-law index, a property of the material.

Viscoelastic fluids have a more complicated relation between shear rate and viscosity. Their extra stress tensor is found by Equation 1.10.

$$\mathbf{T} = \mathbf{T}_1 + \mathbf{T}_2 \quad \text{Equation 1.10}$$

where \mathbf{T}_1 is the viscoelastic component, which is different based on the viscoelastic model chosen, and \mathbf{T}_2 is the purely viscous component found as follows

$$\mathbf{T}_2 = 2\eta_2 \mathbf{D} \quad \text{Equation 1.11}$$

where η_2 is the viscosity for the purely-viscous component of the extra-stress tensor.

The viscosity for the viscoelastic (η_1) and purely-viscous (η_2) components are as follows

$$\eta_1 = (1 - \eta_r)\eta \quad \text{Equation 1.12}$$

$$\eta_2 = \eta_r \eta \quad \text{Equation 1.13}$$

where η_r is the viscosity ratio defined as η_2/η .

The fluids used are corn syrup with a viscosity of 54 Poise, a 2% Carboxymethyl Cellulose (CMC) solution modeled as a non-Newtonian power law fluid as shown in Equation 1.9, and a shear-thinning Bird-Carreau fluid as shown in Equation 1.14. The parameters for Equation 1.9 were calculated by Prakash (1996) from steady shear measurement results as plotted in Figure 1.33.

$$\eta = \eta_\infty + (\eta_0 - \eta_\infty)(1 + \lambda^2 \dot{\gamma}^2)^{(n-1)/2} \quad \text{Equation 1.14}$$

where $\eta_0=100000$ poise, $\eta_\infty=11111.11$ poise, $\lambda=60$, and $n=0.2$ (Connolly 2004).

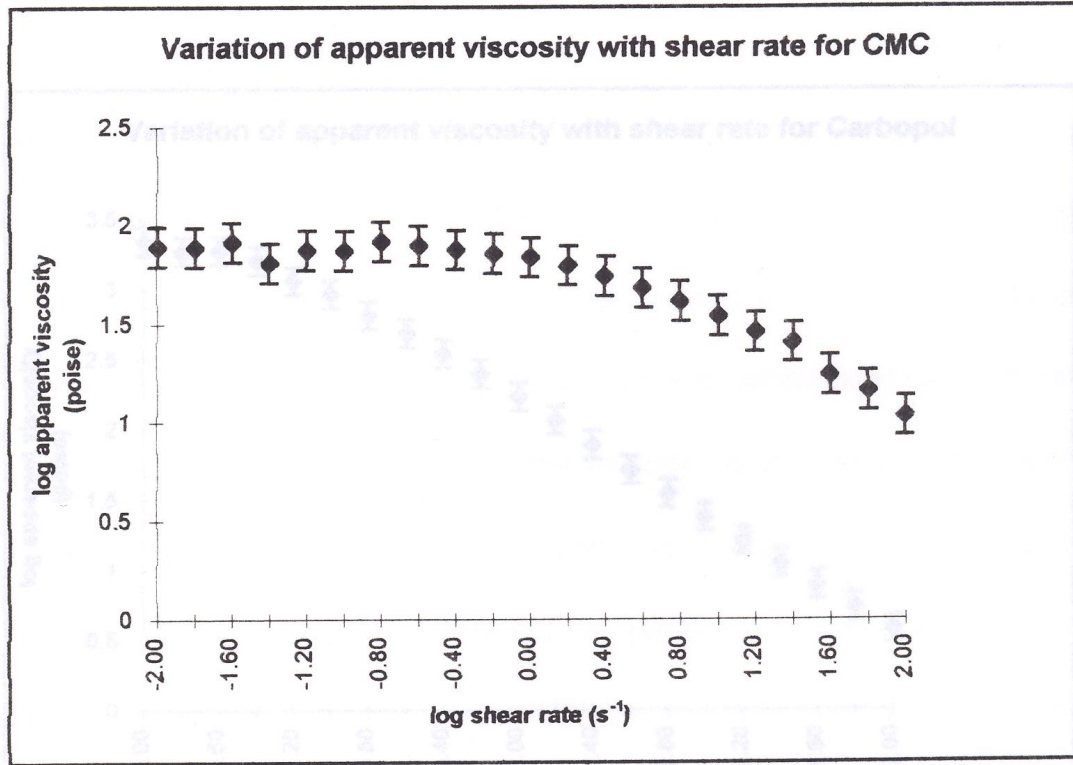


Figure 1.33. Rheological properties of 2% CMC (Prakash, 1996).

1.6.3 Mixing Measurements

Particle tracking experiments are performed by distributing a set of massless particles and then following their trajectories along streamlines in the mixer. For accuracy, a large number of initial points must be chosen. From these trajectories, mixing criteria such as segregation scale, length of stretch (Equation 1.15), area stretch (Equation 1.16), and time averaged efficiency (Equation 1.18) can be obtained. In order to obtain these trajectories Polyflow (2008) integrates $\dot{X} = \dot{V}$ over time. This allows calculation of properties such as stretching for each point on its trajectory.

$$\lambda = |\mathbf{dx}|/|\mathbf{dX}|$$

Equation 1.15

where \mathbf{dx} is an infinitesimal line segment initially of length \mathbf{dX} , \mathbf{X} is the position of a line at $t=0$ and \mathbf{x} is the position of a line at time t .

$$\eta = |\mathbf{da}|/|\mathbf{dA}|$$

where $\mathbf{da} = d\mathbf{x}_1 \times d\mathbf{x}_2$ and $\mathbf{dA} = d\mathbf{X}_1 \times d\mathbf{X}_2$

Equation 1.16

Depictions of these stretch values are found in Figure 1.34.

Local efficiency of mixing (e_λ)

$$e_\lambda(\mathbf{X}, \mathbf{M}, t) = \frac{\dot{\lambda}/\lambda}{(\mathbf{D} : \mathbf{D})^{\frac{1}{2}}}$$

Equation 1.17

where \mathbf{D} is the rate of strain tensor and $(\mathbf{D} : \mathbf{D})^{1/2}$ is the magnitude of \mathbf{D} (Ottino 1989).

Values range between -1 and 1 where a value of -1 indicates all energy was used in shortening of the line and 1 indicates all energy was used in stretching the line.

The time-averaged efficiency ($\langle e_\lambda \rangle$)

$$\langle e_\lambda \rangle(\mathbf{X}, \mathbf{M}, t) = \frac{1}{t} \int_0^t e_\lambda(\mathbf{X}, \mathbf{M}, t') dt'$$

Equation 1.18

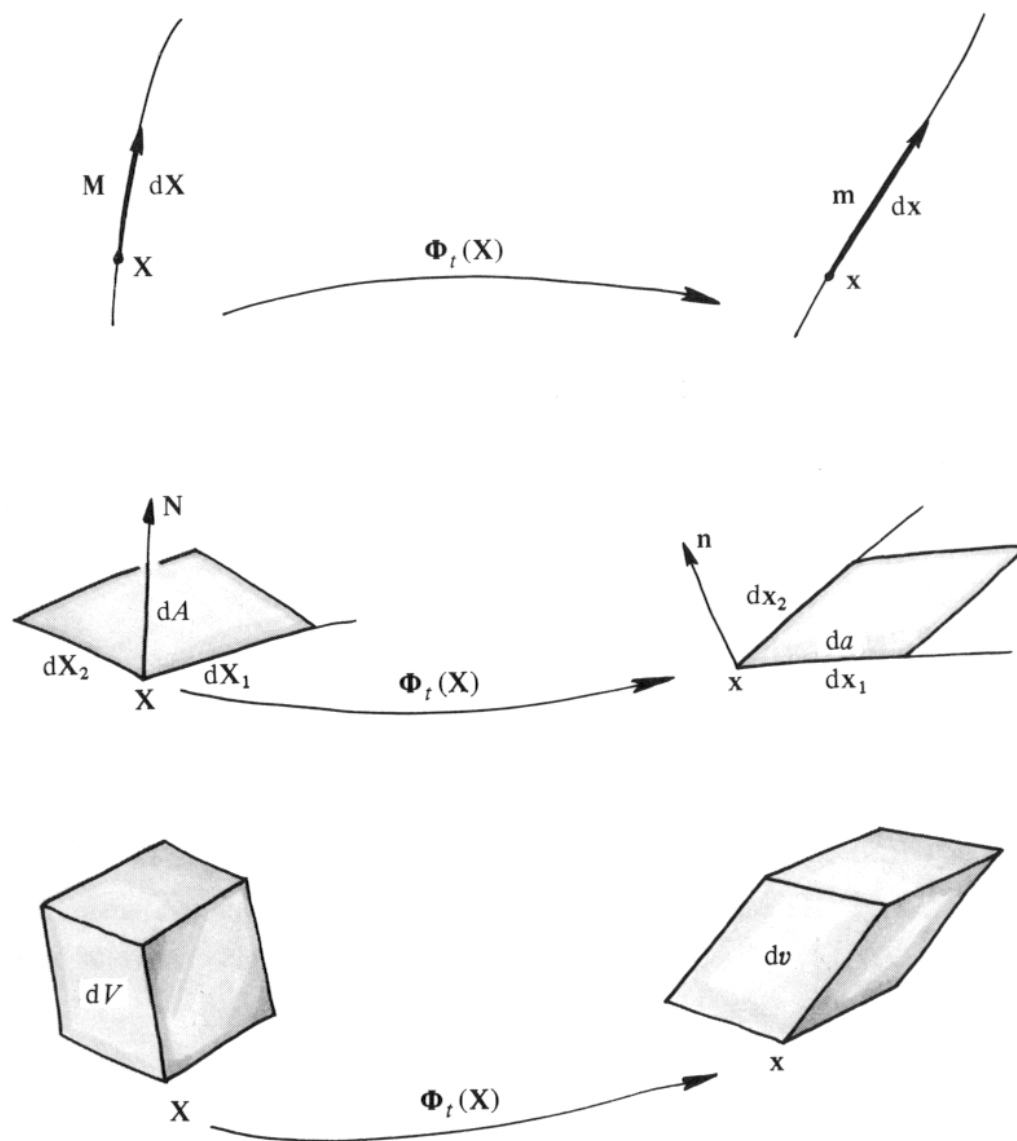


Figure 1.34. Deformation of elements, lines and volumes (Ottino, 1989).

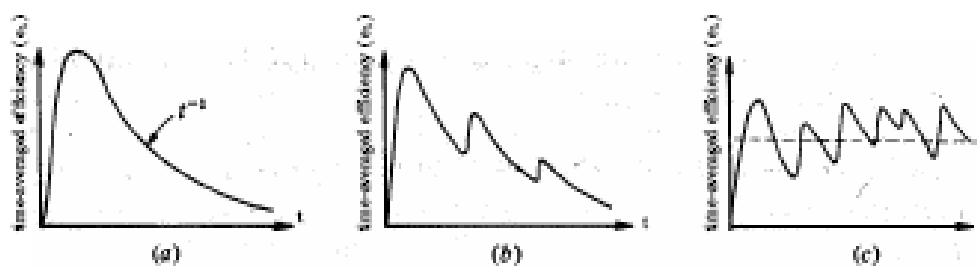


Figure 1.35. Typical behavior of mixing efficiency (Ottino, 1989).

From Figure 1.35 one can see the behavior of time averaged mixing efficiency from (a) the decay of the efficiency with time as t^{-1} for flows with no reorientation such as the simple shearing flow, (b) flows with some periodic reorientation but still decaying on average with time as t^{-1} , and (c) flows with strong reorientation with an average constant value of the efficiency (Ottino, 1989).

Segregation scale is obtained by setting all particles within a given portion of the geometry (e.g. the upper half of the mixer) to an arbitrary concentration value of 1 and the rest of the particles to an arbitrary concentration of 0 (Figure 1.36). At every time step, the scale of segregation is calculated based on the positions of the particles. Thus one can follow the evolution of the parameter with time.

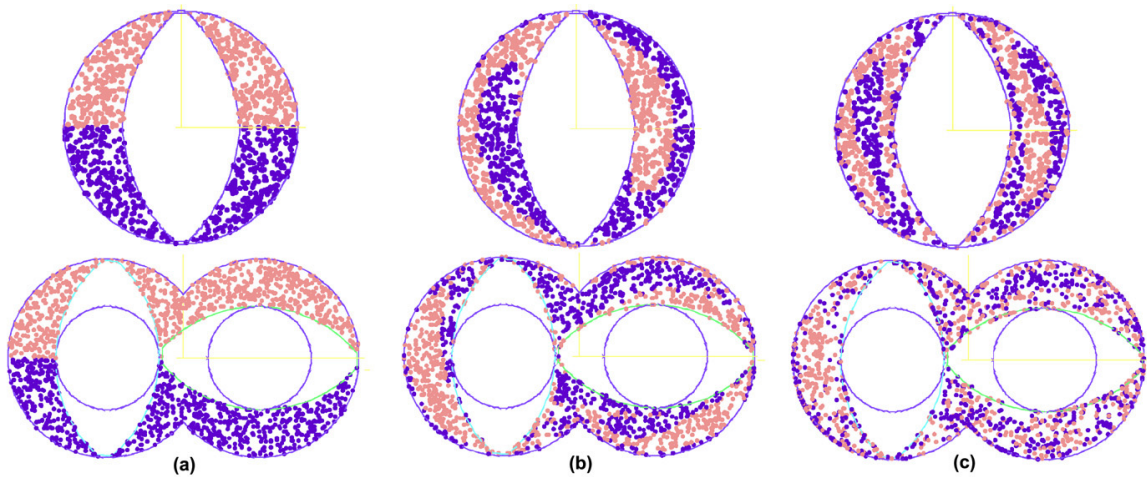


Figure 1.36. Particle tracking results illustrating the distributive mixing between the upper and lower halves of both mixers a) initially, b) after one revolution, c) after 10 revolutions where the red (light) colored points were arbitrarily assigned a concentration of 1 and the blue (dark) colored points a concentration of zero (Connelly and Kokini, 2007).

Scale of segregation is a global measurement intended to indicate the size of segregated regions and is calculated using the following equation.

$$S(t) = \int_0^{\xi} R(r, t) dr \quad \text{Equation 1.19}$$

where r is the distance between two points, t is time, and the correlation coefficient, R , is as follows:

$$R(r, t) = \frac{\sum_{j=1}^M (c_j' - \bar{c})(c_j'' - \bar{c})}{M\sigma_c^2} \quad \text{Equation 1.20}$$

where M is the number of material point pairs, c_j' and c_j'' are the concentrations of the two points in the pair, \bar{c} is the average concentration of all points, and σ_c is the standard deviation. $R(0) = 1$ for points having the same correlation and $R(f) = 0$ where there is no correlation.

Dispersive mixing can be determined by the Manas-Zloczower mixing index λ_{MZ} (Connelly, 2004).

$$\lambda_{MZ} = \frac{|\mathbf{D}|}{|\mathbf{D}| + |\mathbf{\Omega}|} \quad \text{Equation 1.21}$$

where $|\mathbf{D}|$ and $|\mathbf{\Omega}|$ are the strain rate and vorticity tensors respectively. When $\lambda_{MZ} = 0$ there is pure rotational mixing, when $\lambda_{MZ} = 0.5$ there is simple shear flow, and when $\lambda_{MZ} = 1$ there is elongational flow. An additional measure to examine dispersive mixing is the distribution of shear stress.

1.6.4 Critical Capillary Number and Maximum Stable Bubble Diameter

Stone, Bentley and Leal (1986) examined strong flows between simple shear and pure elongational flow due to their ability to produce the greatest deformation at a given shear rate. The velocity gradient tensor, a function of flow type, is seen in Equation 1.22. Strong flows are those with $\alpha > 0$ and which cause greatest deformation for a given shear rate. These are of greatest interest and their flow streamlines are found in Figure 1.37. At small Reynolds numbers, with a neutral buoyant drop and steady flow, droplet behavior is controlled by viscosity ratio, capillary number, and flow type parameter. Deformation measures for different flow types are displayed in Figure 1.38. The orientation of a bubble with respect to the principal strain axis is θ . In a specific flow, droplet deformation is dependent on this angle. For a slightly deformed drop D is used to measure scalar deformation, while for a highly extended drop L/a is used.

$$\Gamma = \frac{1}{2} G \begin{bmatrix} 1 + \alpha & 1 - \alpha & 0 \\ -1 + \alpha & -1 - \alpha & 0 \\ 0 & 0 & 0 \end{bmatrix} \quad \text{Equation 1.22}$$

where Γ is the velocity gradient tensor, α is a flow type parameter, G is shear rate

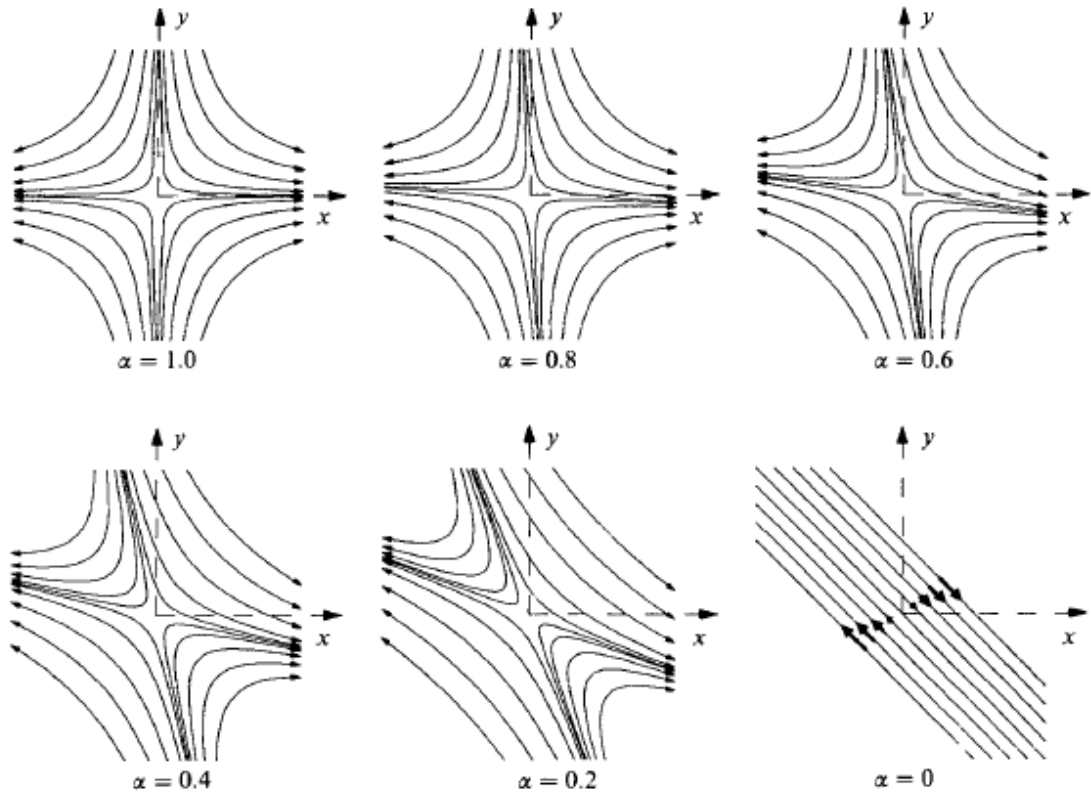


Figure 1.37. Stream lines for linear flow $u = \Gamma x$ (Stone et al., 1986).

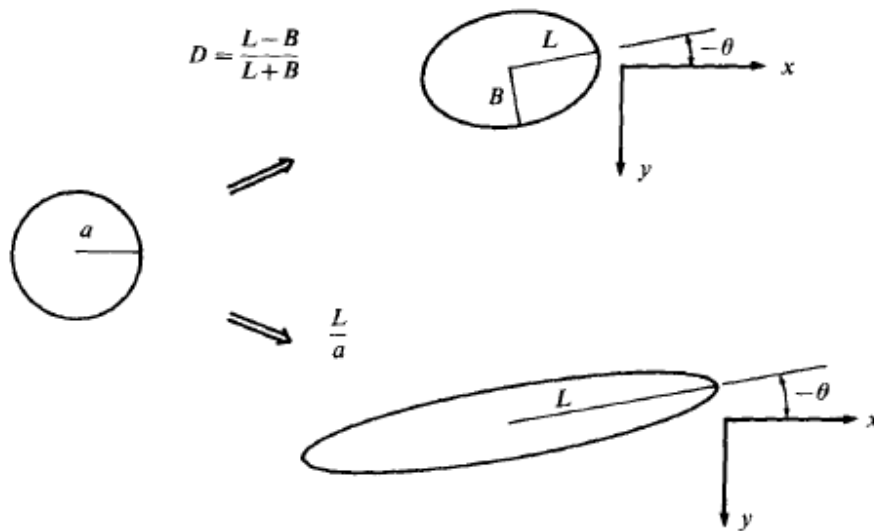


Figure 1.38. Scalar measures of deformation and orientation (Stone et al., 1986).

Various coworkers and Acrivos elegantly obtained critical capillary numbers (Table 1.2) for uniaxial extension from a plot of the deformation curve, 2D planar extension, and simple shear. Bentley and Leal predicted and verified the relation for mixed flow, dependent on flow type (α). Since the continuous twin-screw mixer produces mixed shear and elongational flow, this equation is used for the following work.

Table 1.2. Critical Capillary Number for Different Flow Types

$Ca_{cr} = 0.148 p^{\frac{1}{6}}$	Uniaxial extension (Acrivos and Lo, 1978)
$Ca_{cr} = 0.145 p^{\frac{1}{6}}$	2D planar extension (Hinch and Acrivos, 1979)
$Ca_{cr} = 0.0541 p^{\frac{2}{3}}$	Simple shear (Hinch and Acrivos, 1980)
$Ca_{cr} = \frac{0.145 p^{\frac{1}{6}}}{\alpha^{\frac{1}{2}}}$	Mixed simple shear and pure extension (Bentley and Leal, 1986)

where $p = \mu / \mu_c$

Numerical simulation of shear rate and second invariant of the rate of deformation tensor are well-established, but these have not been tested beyond simple geometries. Because it is difficult to separate extensional properties from shear properties due to their presence in the constitutive model Debbaut and Crochet (1988) extended the extension rate relation to include both the second and third invariants of the rate of deformation tensor. This allowed them to separate normal stress effects from extensional ones.

Using simple shear and uniaxial extension flows, they calculated the second and third invariants of the rate of deformation (Table 1.3). The ratio three times the third invariant divided by the second invariant was also calculated. These equations were arranged to solve for the shear rate and extension rate. They found that using high

Trouton ratio fluids showed the importance of extensional effects on macroscopic behavior.

Table 1.3. Values of second and third invariants of the rate of deformation tensor in simple shear and uniaxial extensional flow (Debbaut and Crochet, 1988)

Flow	II	III	$\frac{3III}{II}$
Simple shear	$\frac{\dot{\gamma}^2}{4}$	0	0
Uniaxial extension	$\frac{3\dot{\epsilon}^2}{4}$	$\frac{\dot{\epsilon}^3}{4}$	$\dot{\epsilon}$

where velocity gradients are

Simple shear

$$v_1 = \dot{\gamma}x_2$$

$$v_2=v_3=0$$

Uniaxial extension

$$v_1 = \dot{\epsilon}x_1$$

$$v_2 = \frac{-\dot{\epsilon}x_2}{2}$$

$$v_3 = \frac{-\dot{\epsilon}x_3}{2}$$

For biaxial extension, the invariant ratio is multiplied by two (Equation 1.23). This biaxial equation was used for calculations in this work. First, the second and third invariants were calculated for an incompressible fluid, and then these invariants were used to calculate the extension rate.

$$\dot{\epsilon}_B = 6 \frac{III}{II}$$

Equation 1.23

The Manas-Zloczower mixing index was also used as a second criterion to see the distribution of shear rate and extension rate and understand the pre-dominance of shear or extensional flows. Both the dispersive mixing index and the flow type parameter alpha indicate the rotational and elongational character of the flow (Table 1.4). They have different ranges, but are calculated using the deformation tensor and the vorticity tensor.

Table 1.4. Mixing index and flow type parameter (Bentley and Leal, 1986)

	α	λ
Pure Rotation $ \mathbf{D} = 0$	-1	0
Simple Shear $ \mathbf{D} = \mathbf{\Omega} $	0	0.5
Pure Extension $ \mathbf{\Omega} = 0$	1	1

where $\alpha = \frac{|\mathbf{D}| - |\mathbf{\Omega}|}{|\mathbf{D}| + |\mathbf{\Omega}|}$ and $\lambda_{MZ} = \frac{1 + \alpha}{2}$

Chapter 2

EFFECT OF MIXER GEOMETRY AND OPERATING CONDITIONS ON MIXING EFFICIENCY OF A NON-NEWTONIAN FLUID IN A TWIN SCREW MIXER¹

2.1 Abstract

The effect of mixer speed, fluid inflow rate, and paddle angle was examined in a shortened geometry. 3D FEM simulation of non-Newtonian 2 g/100 mL carboxymethyl cellulose aqueous solution in the mixing region of a Readco continuous mixer was performed. Data gathered included velocity vectors, shear rate, and mixing index. Increasing mixer speed increased velocity magnitudes in the horizontal and vertical directions. Fluid inflow rate had little impact on velocity in the horizontal and vertical directions, but increased velocity in the axial direction and elongational contribution to the mixing index. All configurations showed areas of simple shear flow where the fluid experienced high shear rates. Staggering paddles increased the maximum axial velocity and shear rate. When successive paddles on the same screw are parallel, a zone was seen between the center of the paddle and the barrel wall which demonstrated efficient dispersive mixing.

¹ Reprinted with permission from Maureen L. Rathod and Jozef L Kokini, “Effect of mixer geometry and operating conditions on mixing efficiency of a non-Newtonian fluid in a twin screw mixer”, Journal of Food Engineering, 118, 256-265 (2013).

2.2 Introduction

Mixing is an important process in the production of foods, polymers, and pharmaceuticals. It is used to blend different components, to develop desirable product attributes and to introduce air. All of these processes are important to mixing of wheat flour with water and other ingredients resulting in wheat flour doughs. In this system, water must be distributed and flour particles must be broken to release starch and protein to allow gluten formation. Additionally, mixing is used to stretch glutenin promoting molecular alignment and the formation of non-covalent bonds giving dough elasticity, imparting machinability and gas retention. Bubbles introduced during mixing become nuclei for carbon dioxide formed in fermentation and allow for expansion of the dough during proofing (Connelly and Kokini, 2007).

Various kinds of mixers promote different types of mixing. These include batch and continuous mixers and those with both fixed and variable geometries. Effective mixers often have complex geometries and several moving parts. Numerical simulation can provide velocity, shear rate, shear stress, temperature, and moisture content distribution within the mixer in a non-destructive manner which is a distinct advantage over experimental measurements that often disturb the fluid while acquiring data. One major limitation of numerical simulation is the increased computational requirement for more complicated simulations. Using a more complex mixer geometry and fluid increases the equipment and time cost, especially when the fluids being mixed are very viscous or viscoelastic.

In determining mixing efficiency, one can examine both dispersive and distributive mixing. Distributive mixing spreads particles throughout the mixer volume

and is influenced by fluid stretching and reorientation. Measures of distributive mixing include length of stretch, stretching efficiency, and segregation scale. Dispersive mixing separates clumps or aggregates in the mixer through shear and elongational stresses (Alsteens, et al., 2004). It is measured by the Manas-Zloczower mixing index.

Muzzio and his research group (Alvarez et al., 2002; Lamberto et al., 2001; Zalc et al., 2001; Portillo et al., 2008, 2009) have studied stirred tank reactors, static mixing flows, and mixing in laminar to turbulent flow regimes with generalized Newtonian fluids. These investigations have involved experimental and computational fluid dynamics (CFD) work. Lamberto et al. (2001) used a rotating reference frame technique to examine laminar mixing of a Newtonian fluid in an unbaffled stirred tank with an impeller. This study was comparable to simulations performed using a classical geometry and varying time-periodic boundary conditions. The objective was to observe the effect of varying speed on mixing performance. They found the toroidal structures which form at a constant impeller speed periodically relocated if the speed varied between two values. This relocation caused an exponential increase in stretching. Increasing the frequency of the speed fluctuation also increased the stretching rate. Simulation results were a close match to data obtained by particle image velocimetry (PIV) in a seeded glycerin solution.

More recently, Portillo et al. (2008) examined the mixing of acetaminophen and lactose in a continuous convective blender. Their goal was to see the effect of blade design, mixer rotation rate, and processing angle on mixing efficiency. Blended samples were taken at the blender outlet and analyzed using NIR to determine their composition. Relative standard deviation (RSD) of tracer concentration was used as a measure of

homogeneity. Lower RSD was taken as an indicator of less sample variability and therefore better mixing. The variance reduction ratio (VRR) which is the ratio of the calculated variance for the material entering and exiting the mixer measures the ability of a mixer to eliminate variability found in the product before entering the mixer. The upward processing angle (where the exit of the mixer was positioned higher than the entrance) resulted in the largest mean residence time as well as the lowest RSD and highest VRR providing the best mixing performance. Increasing mixer rpm decreased the powder residence time but increased the number of blade passes it experienced resulting in more variability with increasing speed. Increasing the blade angle from 15° to 60° decreased the RSD, but above 60° the axial transport was not strong enough to continue the trend.

In comparing different blenders, Portillo et al. (2009) found that the effectiveness of a mixer was affected by the design of the impeller and blades. The blade angle relative to the shaft affected mixing performance. Impeller rotation rate caused the most significant effect on relative variance, followed by powder cohesion, and then vessel angle. Rotation rate and processing angle significantly affected residence time, with rotation rate having a greater influence. A direct correlation was found between improved mixing and higher residence time.

Zhang et al. (2009) examined residence time distribution (RTD) of a co-rotating twin screw extruder using CFD and compared the data obtained with experimental results. They analyzed the distributive mixing performance of different kneading disc types by measuring the area stretch ratio, instantaneous efficiency and time-averaged efficiency. The researchers found that local RTD was affected by both operating

conditions (screw speed and feed rate) and the geometry of the kneading discs used. Mean RTD increased while axial mixing decreased with increasing stagger angle of the kneading discs. Generally, kneading discs with a disc gap, small disc width, and large stagger angle produce good distributive mixing performance.

Previous numerical simulation work has frequently examined mixing behavior of simple fluid in simplified geometries. In our lab, geometries resembling those in industrial mixers have been used with Newtonian and non-Newtonian fluids (Connelly and Kokini, 2003, 2004, 2006a, 2006b, 2007; Connelly, 2004; Ashokan et al., 2003; Ashokan 2008; Vyakaranam, 2012; Vyakaranam and Kokini, 2012; Vyakaranam et al., 2012). Mixing in a Brabender Farinograph was explored numerically by Connelly (Connelly, 2004; Connelly and Kokini, 2004, 2006a, 2006b) using mesh superposition and particle tracking with a Newtonian fluid. The results were validated against laser Doppler anemometry (LDA) values obtained by Prakash and coworkers (Prakash, 1996; Prakash and Kokini, 1999, 2000; Prakash et al., 1999). Twin-screw mixers have also been simulated with more complex fluids. Successful simulation of mixing in a twin-screw mixer was performed using 2D finite element method (FEM) techniques; and these results were compared to those from previous 2D simulation of a single screw mixer (Connelly and Kokini, 2007). A generalized Newtonian Carreau fluid model was used in a mixed Galerkin FEM simulation.

Variation of mixing index with mixer operating conditions and configuration was not found to be significant (Cheng and Manas-Zloczower, 1997) but changing fluid rheology had an impact. The influence of rheology increased with non-Newtonian behavior (Prakash and Kokini, 1999). Viscoelasticity enlarged the areas of high mixing

index, those with more elongational flow. Increased shear thinning caused greater areas of plug flow with low mixing index values. Shear stress was shifted in a viscoelastic fluid so that high shear stresses increased ahead of the blade and low shear stress moved behind the blade. Adding high values of shear stress to areas with elongational flow increased the dispersion ahead of the paddle. Conversely, increased shear stress magnitudes near the paddle tip increased the area of dead zones, thus hindering dispersion (Connelly and Kokini, 2004).

Recent work by Vyakaranam, et al. (2012) has examined mixing in a Readco continuous mixer both experimentally and numerically. A high viscosity Newtonian corn syrup was used as the model fluid. Experimental measurements were made using LDA to determine fluid velocity and compared to values obtained via numerical simulation. Stagger angle of the mixer paddles caused local disruption but did not change global forward or reverse flow. Flow rate was found to be independent of stagger angle, but varied with screw speed. The axial component of velocity (v_z) was affected by stagger angle, but the horizontal component (v_x) and the vertical component (v_y) were unaffected.

2.3 Materials and Methods

2.3.1 Fluid Rheology

This research focused on a non-Newtonian power-law fluid. Fluids that follow the power-law relation have a viscosity dependent on shear rate as found in Equation 2.1.

$$\mathbf{T} = 2\eta(\dot{\gamma}, T)\mathbf{D} \quad \text{Equation 2.1}$$

where \mathbf{T} is extra stress tensor, \mathbf{D} is the rate of deformation tensor and η is dynamic viscosity, here a function of temperature T and local shear rate $\dot{\gamma}$ as seen below in Equation 2.3. The extra stress tensor is isotropic and represents the effects of deformation

on a material while being dependent on the gradient of fluid velocity and fluid density. In the case of a Newtonian fluid, it is a linear function of the rate of deformation tensor:

$$\dot{\gamma} = \sqrt{2tr(\mathbf{D}^2)} \quad \text{Equation 2.2}$$

$$\eta = K(\lambda\dot{\gamma})^{n-1} \quad \text{Equation 2.3}$$

where K is the consistency factor, λ is the natural time, and n is the power-law index which is a property of the material.

A 2% by weight aqueous Carboxymethylcellulose (CMC) solution was modeled as a non-Newtonian power law fluid. CMC has served as a model fluid in much of our work to date (Prakash, 1996; Prakash and Kokini, 1999, 2000; Prakash et al., 2000; Connelly and Kokini, 2006a, 2006b; Fanning, 2009). The parameters for Equation 2.3 were calculated by Prakash (1996) from steady shear measurement results as $K=15.74 \text{ N s}^n \text{ m}^2$, $n=0.397$, and $\lambda=1$.

2.3.2 Characterization of mixing performance

Dispersive mixing was characterized by the Manas-Zloczower mixing index

λ_{MZ} (Cheng and Manas-Zloczower, 1990):

$$\lambda_{MZ} = \frac{|\mathbf{D}|}{|\mathbf{D}| + |\mathbf{\Omega}|} \quad \text{Equation 2.4}$$

where \mathbf{D} and $\mathbf{\Omega}$ are the rate of deformation and vorticity tensors respectively. When

$\lambda_{MZ}=0$ it indicates pure rotational mixing, $\lambda_{MZ}=0.5$ indicates simple shear flow, $\lambda_{MZ}=0.7$

indicates efficient dispersive mixing, and $\lambda_{MZ}=1$ indicates elongational flow. An

additional measure to examine dispersive mixing is the distribution of shear stress

(Manas-Zloczower and Kaufman, 2009).

2.3.3 Numerical Simulations

Numerical simulations were performed using the Polyflow family of programs from ANSYS-Fluent, Inc. (Lebanon, NH). These are a CFD program suite including a mesh generator: Gambit, FEM solver: Polyflow, and graphics post-processor: CFX-Post. A Dell Precision 690 workstation with Dual Core Xeon processors and 16 GB RAM was used.

The boundary conditions used were no slip at the walls, fully developed Poiseuille flow in the region between paddles and barrel, and zero tangential velocity and normal force at the outflow. Isothermal flow was modeled with inertia taken into account, and gravity was neglected. Fluid parameters used were those for a 2% CMC solution described above with a density of 1.0068 g/cm^3 . Viscosity and density values were measured at room temperature (23-25°C). Mesh superposition was used to account for the moving paddles in the mixer geometry.

2.3.4 Mesh superposition

In order to account for the moving paddle elements without remeshing the entire fluid region for every time step, the mesh superposition technique was used. The paddles and barrel are meshed separately and then the paddles are superimposed on the barrel mesh. A barrel element is determined to be part of the solid paddle if more than 60% of it is overlapped by the paddle mesh. The threshold value was identified as that which gave good results in several different simulation problems performed by Polyflow. A value too small would not allow fluid flow between the screw and barrel wall and could allow a screw dimension which is larger than the barrel. Once a barrel element is considered part of the paddle as stated above, the velocity of that element is set equal to the velocity of

the moving part. This adjustment is accomplished by the use of a penalty term $H(\mathbf{v} - \bar{\mathbf{v}})$ in the equation of motion as seen below in Equation 2.5. H is a step function which equals 0 outside the moving part and 1 within it. The variable \mathbf{v} is velocity; and $\bar{\mathbf{v}}$ is the local moving part velocity.

$$H(\mathbf{v} - \bar{\mathbf{v}}) + (1 - H)(-\nabla p + \nabla \cdot \mathbf{T} - \rho \mathbf{a}) = 0 \quad \text{Equation 2.5}$$

where p is the pressure, and $\rho \mathbf{a}$ is the acceleration term. Since gravity is neglected, there is no gravity term in Equation 2.5.

The boundary between the solid and fluid elements can only be determined to within one element. When a small amount of fluid leakage into the paddle occurs (Jongen, 2000) a very small compression factor ($\beta=0.01$) is added to the continuity equation to compensate for it and eliminate its effect on the computation. The modified equation then becomes as follows:

$$\nabla \cdot \mathbf{v} + \frac{\beta}{\eta} \nabla^2 p = 0 \quad \text{Equation 2.6}$$

2.3.5 Mixer Geometry

The Readco continuous mixer (Figure 2.1) model geometry was created and meshed for numerical simulation using Gambit (Figures 2.2a and 2.2b). This mixer is a co-rotating mixer with initial and exiting conveying screws and nine pairs of self-wiping paddles in the center length of the mixer. Here only the mixing section of the mixer is examined. In order to balance computational cost with accuracy, several meshes with varying densities were developed and the resulting data was compared to experimental values. Root mean square differences were calculated for simulation velocities as a percent of the experimental values at several points in the mixer. Velocity magnitude data

for the various meshes was also compared. This information was used to choose the best mesh combination for further simulations (Ashokan, 2008). The outcome was a choice of the least dense mesh which provided an accurate velocity profile and most closely coincided with experimental data. Further description of the method used can be found in Vyakaranam et al. (2012).

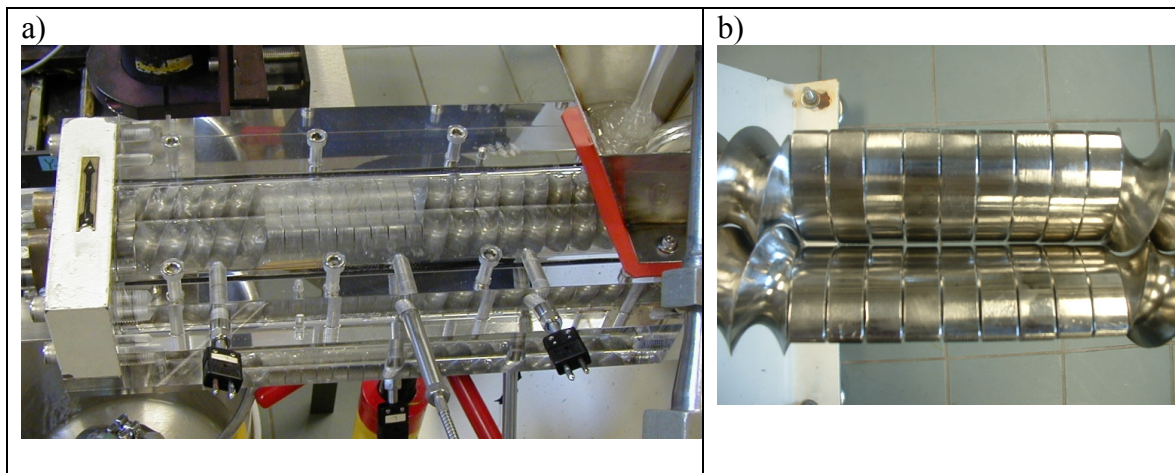


Figure 2.1. a) 2'' Readco continuous processor with Plexiglas barrel, b) close-up of paddles in parallel configuration (Ashokan, 2008).

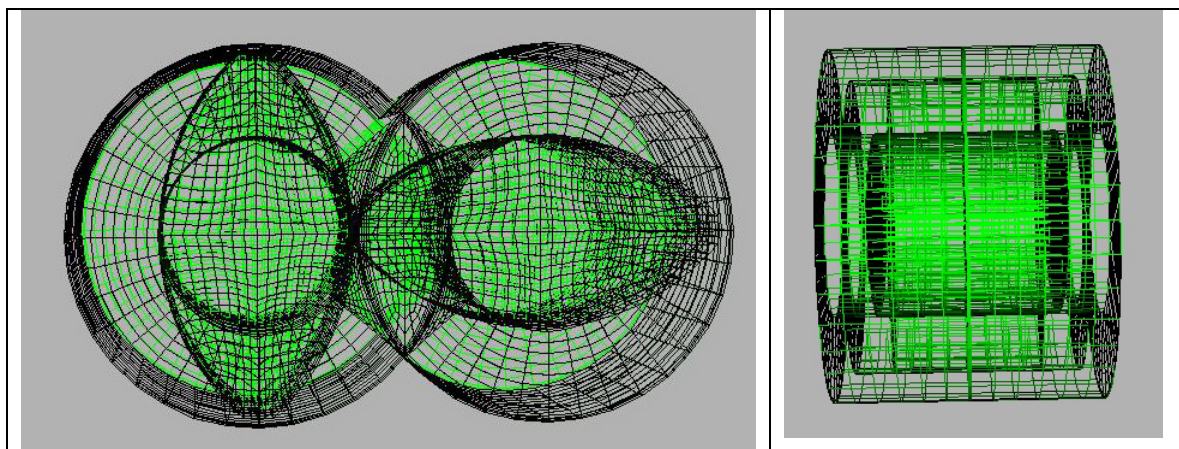


Figure 2.2. 3D barrel mesh with two pairs of superimposed paddles a) front view b) side view.

Paddle angles, rotation speeds, and fluid inflow rates were chosen based on the starting point (100rpm and 55.31cc/s) of previous experimental work in our laboratory

(Fanning, 2009). Here, values were chosen above and below those used previously in experimental and simulation work to see the trend with changing mixer speed and fluid inflow rate. Paddles configurations were used with the second paddle set staggered at 0° (2X), 45° (2X45), and 90° (2X90) to the initial paddles. Mixer speeds of 50rpm, 100rpm, and 150rpm were selected. Fluid inflow rates of 20cc/s, 40cc/s, 55.31cc/s, 75cc/s, and 100cc/s were examined. Each simulation was run for one rotation of the paddles and results were recorded every 10° . Based on the mixer speed the output time at 10° is 0.033333 seconds at 50rpm, 0.016667 seconds at 100rpm, and 0.011111 seconds at 150rpm.

The various paddle angles are shown below in Figure 2.3. Figure 2.4 below shows the line along which data points were taken. This line passes through the gap between the two paddle pairs. Velocities, shear rates, and mixing indices shown in the following graphs were obtained on the line between point P1 and point P2.

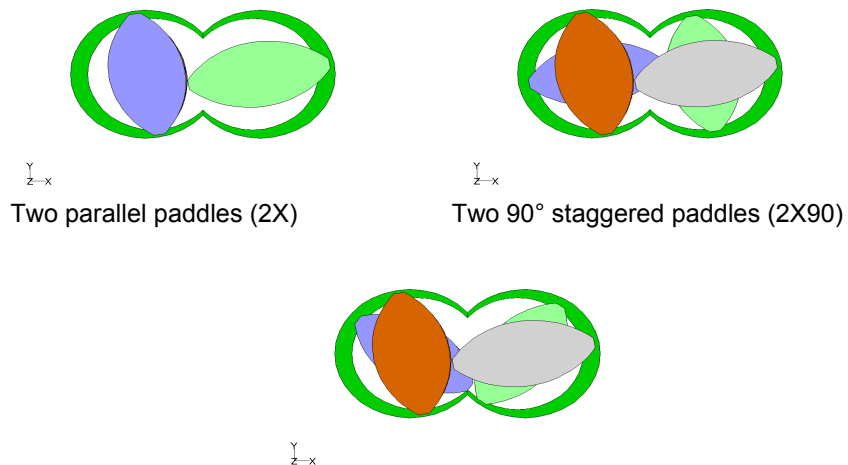


Figure 2.3. Paddle angle used in simulations.

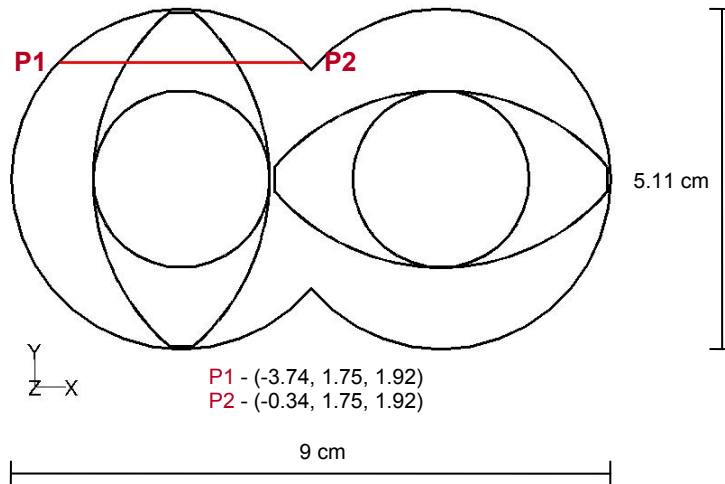


Figure 2.4. Location of measurement points along the line between point P1 and point P2.

2.4 Results and Discussion

2.4.1 Effect of flow rate on 3-D velocity distributions

Figures 2.5-7 show v_x , v_y , and v_z plotted against x position along the line between points P1 and P2 for various flow rates. The horizontal axis across the barrel is x , the vertical axis is y , and the axis from the inlet to the outlet of the mixer is z . The paddle angles are as shown in Figure 2.3. Values of v_x have low magnitudes near the center of the mixer (x location closer to zero) and near the barrel wall (x location closer to -4). Negative values of v_y are seen near the barrel wall and positive values near the barrel center. These values are a logical result of the counterclockwise rotation of the paddles pushing the fluid up near the center of the mixer, across the top, and then down near the barrel wall.

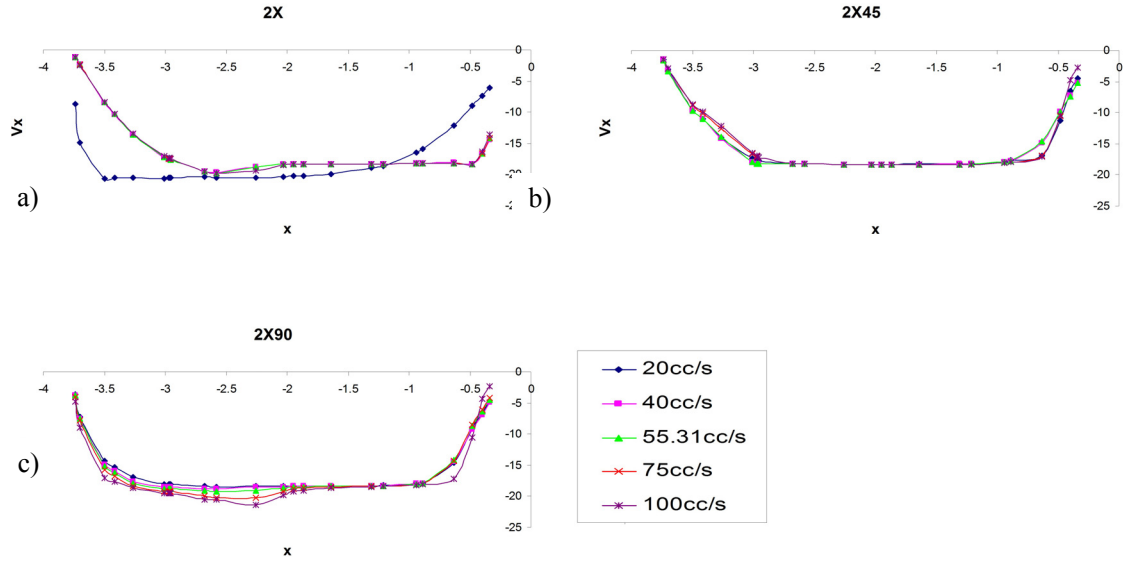


Figure 2.5. X component of velocity different flow rates for 2X, 2X45, 2X90.

There is no significant trend for v_x and v_y with increasing fluid flow rate in the 2X and 2X45 configurations (Figures 2.5 and 2.6). The exception is 20cc/s in the 2X configuration which is not a fast enough rate to follow the curves found with the other flow rates. Higher values near the barrel wall are generated because the lower fluid inflow rate allows the fluid in this area to spend more time in the mixer, experiencing more passes of the paddles. This effect does not occur in the fluid at the center of the mixer which is undergoing forward pumping motion advancing the fluid.

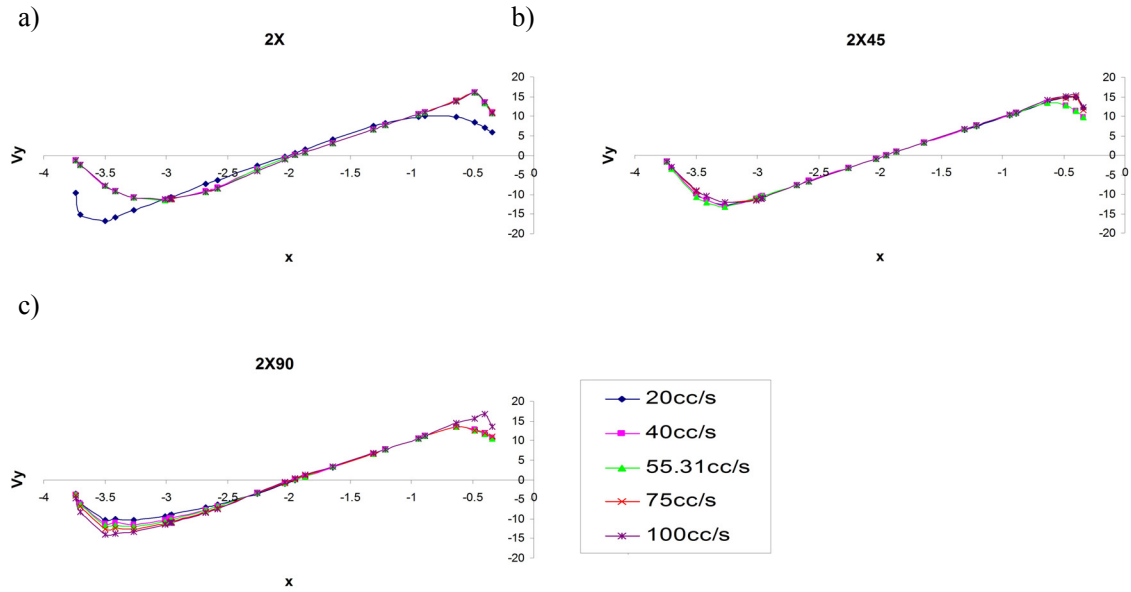


Figure 2.6. Y component of velocity at different flow rates for 2X, 2X45, 2X90.

A characteristic critical flow rate does not appear in the staggered paddle configurations. The staggered paddles impart consistent v_x and v_y values to the fluid even at the lowest fluid inflow rate. In the 2X90 configuration (Figures 2.5 and 2.6), increasing fluid inflow rate increases the magnitude of negative v_x and v_y values as the fluid approaches the barrel wall where faster fluid flow aids in increased mixing, adding to the fluid motion caused by the paddles. Increasing flow rate increases v_z . At a constant flow rate, average v_z would be constant in a pipe. Average v_z should also be constant at a constant flow rate in a complex geometry, but it is not. Our observation of increasing v_z is counter-intuitive and unexpected. Constant flow should produce constant v_z in steady state flow, but here it does not due to the complexity of the geometry.

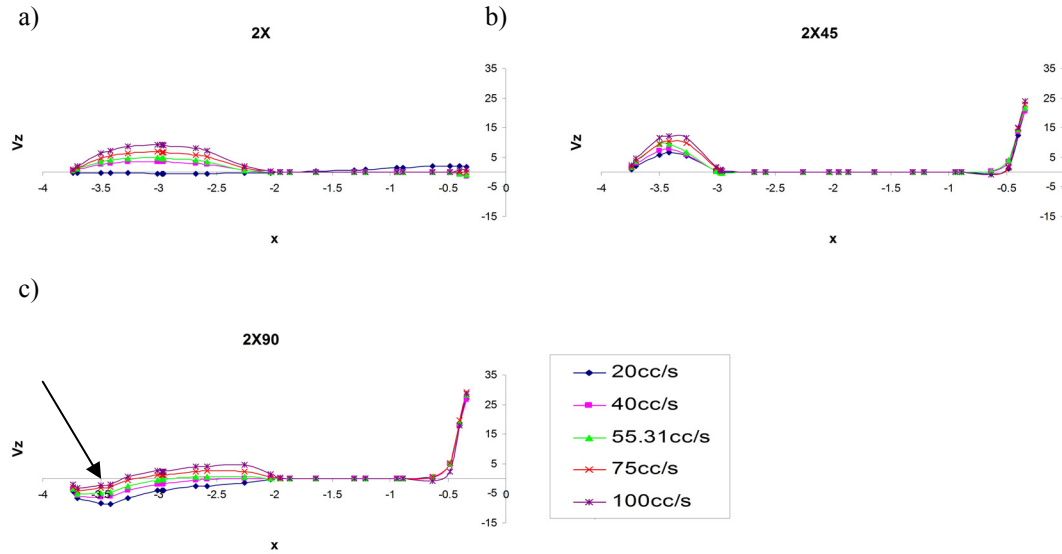


Figure 2.7. Z component of velocity at different flow rates for 2X, 2X45, 2X90.

Increasing stagger angle increases v_z near the center of the mixer, resulting in more flow-through in this area. Increased v_z with staggered paddles is unexpected because staggered paddle configurations are frequently chosen to increase mixing and fluid reorientation. Staggered paddles are generally expected to decrease v_z and possibly generate areas of backflow like those seen in the 2X90 configuration (Figure 2.7c). Backflow is indicated by negative v_z and marked by an arrow in the figure. The additional conveying effect in the center of the mixer, due to the influence of both the left and right-hand paddles, is enhanced by the staggered paddles.

2.4.2 Effect of flow rate on shear rate and mixing index

Shear rate values are higher near the center of the mixer for staggered configurations (Figure 2.8). Maximum shear rate for both staggered geometries is significantly larger than that found for 2X; and the peak for 2X90 is greater than that for 2X45. The higher shear rate near the center of the mixer is found because the fluid passes in a narrow space between two objects moving in the opposite direction. A higher shear

rate is also found where the fluid is forced between the paddle and barrel wall because of the narrow space. In this area, only one object is moving so the values are smaller than those in the center. Increasing flow rate did not significantly affect shear rate values. The exception, once again, is the 20cc/s rate in the 2X geometry. This flow is below the critical rate necessary to mirror the trend seen at the other values.

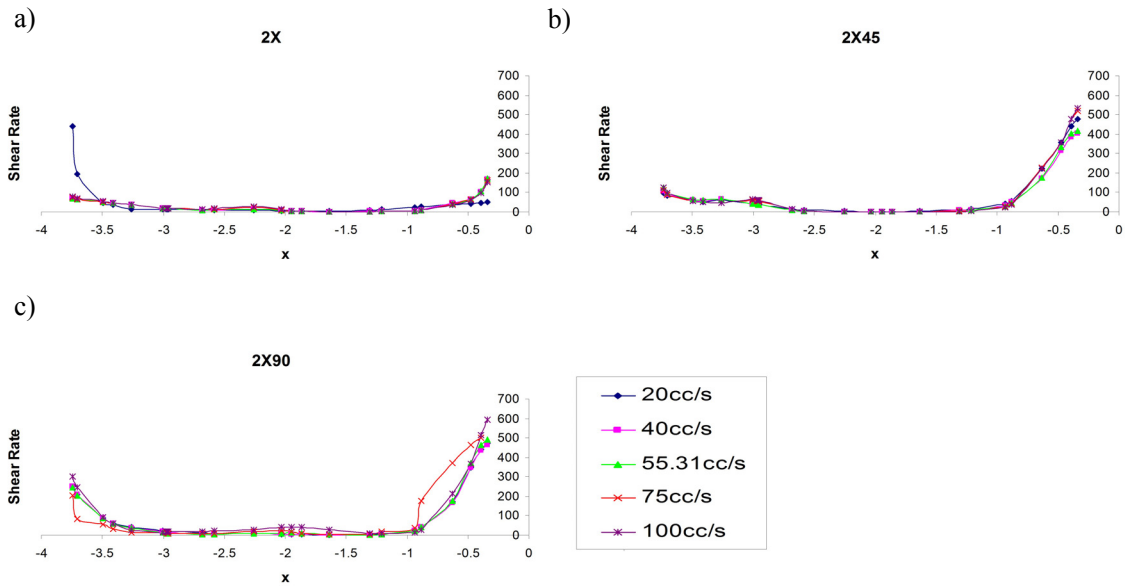


Figure 2.8. Shear rate at different flow rates for 2X, 2X45, 2X90.

Increasing flow rate increases the elongational contribution to the mixing index (Figure 2.9). This faster flow minimizes the rotational impact on the fluid as it spends less time in the mixer and is moved primarily in the axial direction through the mixer. Again the fluid inflow rate of 20cc/s is below the critical value needed in the 2X configuration to follow the trend seen at higher flow rates. In particular, there is an area of efficient dispersive mixing ($\lambda_{MZ} = 0.7$) between the paddle center and the barrel wall for all flow rates greater than 20cc/s.

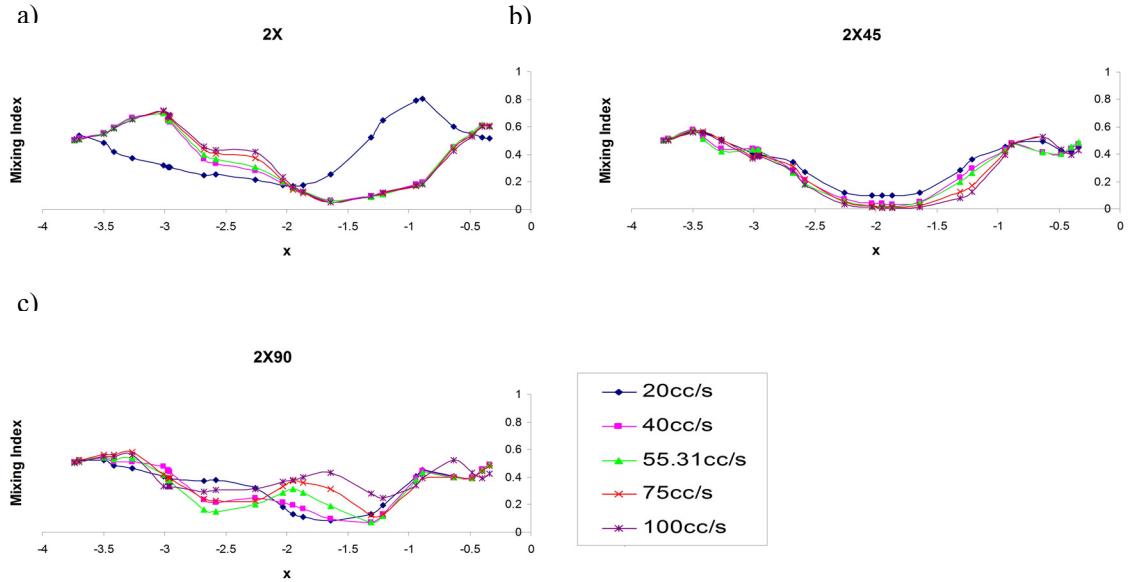


Figure 2.9. Mixing index at different flow rates for 2X, 2X45, 2X90.

Simple shear flow ($\lambda_{MZ} = 0.5$) occurs near the barrel wall and center which coincides with the higher shear rate values seen above. Most rotational flow occurs at mid-range x values, near the center axis of the paddle due to the location of these points with respect to the hub of rotation. In Figure 2.9b, the 2X45 configuration shows a neat pattern of mixing index values with shear flow near the center of the mixer and the barrel wall and pure rotational flow ($\lambda_{MZ} = 0$) in the center of the paddle. Both 2X and 2X90 have additional fluid disruption and have no areas of pure rotational flow.

2.4.4 Effect of mixer speed on 3D velocity distribution

Increasing mixer speed increased v_x magnitude (Figure 2.10) but the trend remains the same with stagger angle. There is little variation between 2X, 2X45, and 2X90. Only the number of points at maximum velocity magnitude increases with increasing stagger angle. The largest magnitude velocity values for each mixer speed are the same for all three geometries. In Figure 2.11, v_y has negative values near the barrel

wall and positive values near the barrel center. Increasing v_y magnitude occurs with increasing mixer speed. Trends seen for v_x and v_y coincide with the fluid motion in the mixer. The paddle pushes fluid up near the center of the mixer, across the top, and down near the barrel wall due to the counter-clockwise rotation. The three configurations have very similar trends for all mixer speeds.

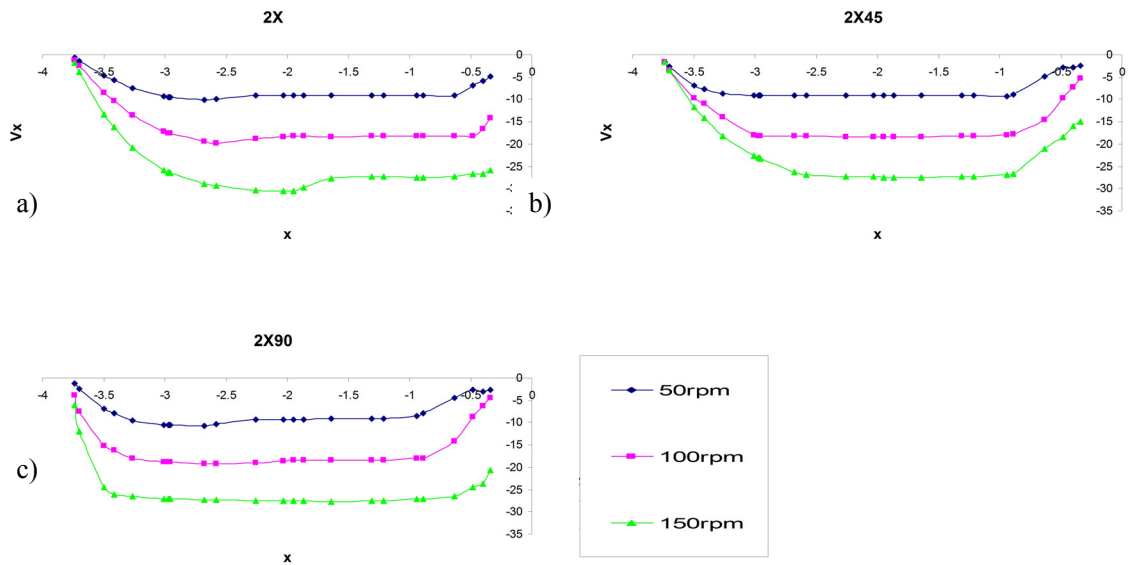


Figure 2.10. X velocity component at different rotation speeds for 2X, 2X45, 2X90.

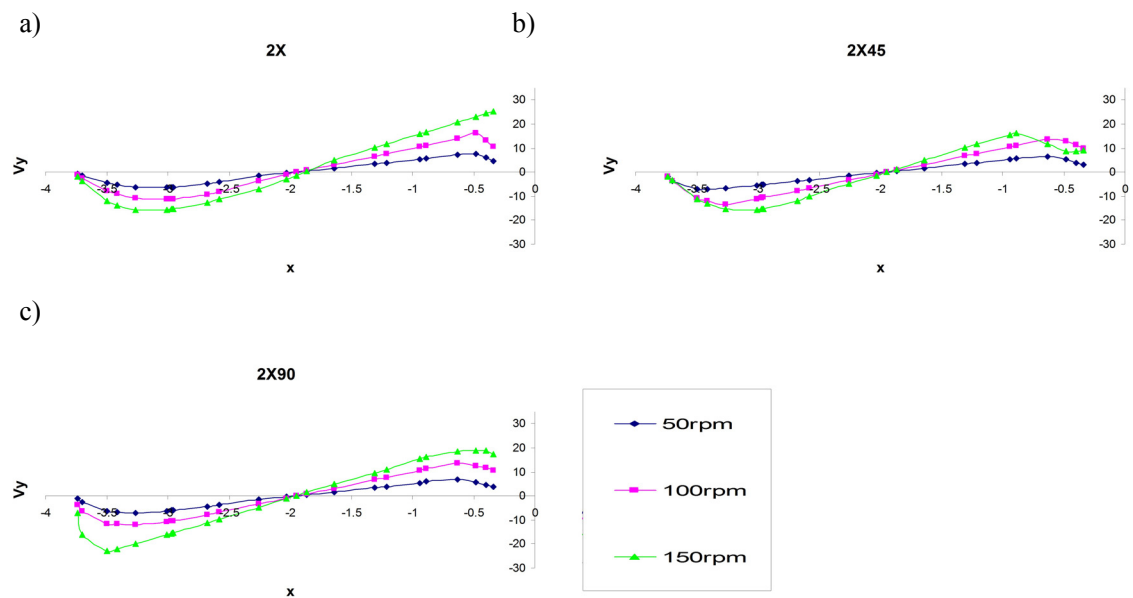


Figure 2.11. Y velocity component at different rotation speeds for 2X, 2X45, 2X90.

Increasing mixer speed increases v_z in the 2X geometry (Figure 2.12). This trend does not continue in the staggered configurations. In fact, areas of backflow are seen in both 2X45 and 2X90 at 150rpm. Backflow causes fluid to spend more time in the mixer instead of flowing directly through it enabling the mixer to cause more reorientation.

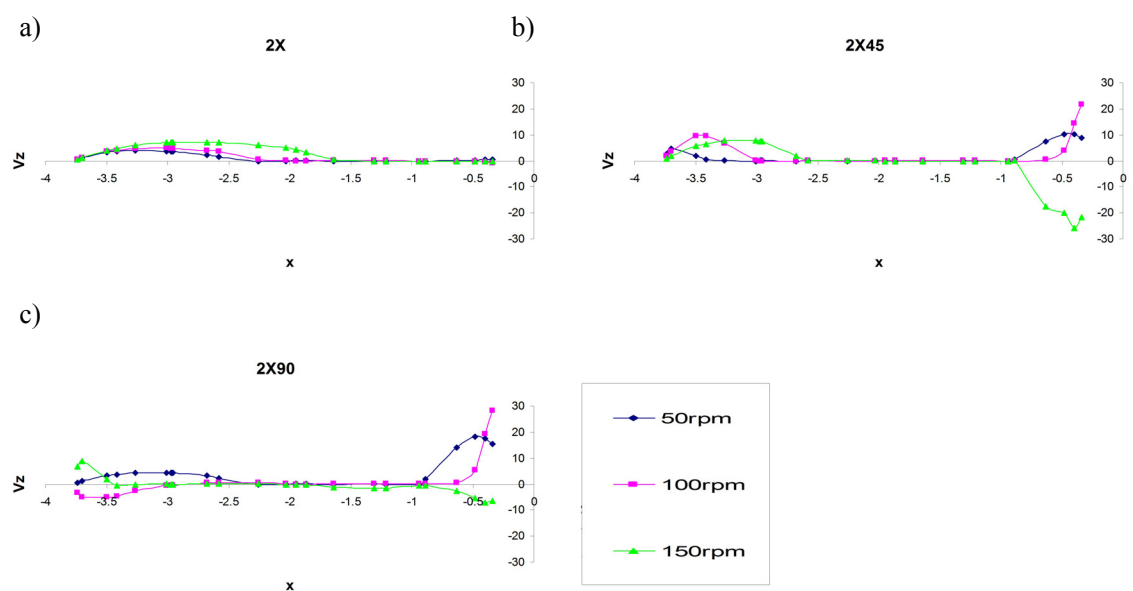


Figure 2.12. Z velocity component at different rotation speeds for 2X, 2X45, 2X90.

2.4.5 Effect of mixer speed on shear rate and mixing index

Shear rate values increase with increasing mixer speed near the barrel wall of the mixer (Figure 2.13) corresponding with the squeezing of the fluid between the paddle tip and barrel wall as the paddle rotates. In the center of the mixer, the fluid also experiences shearing forces due to the movement of both paddle sets. Due to the 90° angle between the right and left-hand paddle, each imparts opposing motion to the fluid. Near the barrel center, increasing the mixer speed from 50rpm to 100rpm increases shear rate and increasing the mixer speed from 100rpm to 150rpm decreases the shear rate. The highest speed seems to indicate a speed above which further increases in mixer speed do not positively affect shear rate. Both staggered configurations have higher maximum shear rates than 2X, but 2X90 has the highest peak. This peak is seen near the mixer center at 100rpm and moves to the barrel wall at 150rpm, indicating a change in shear flow location at higher speed.

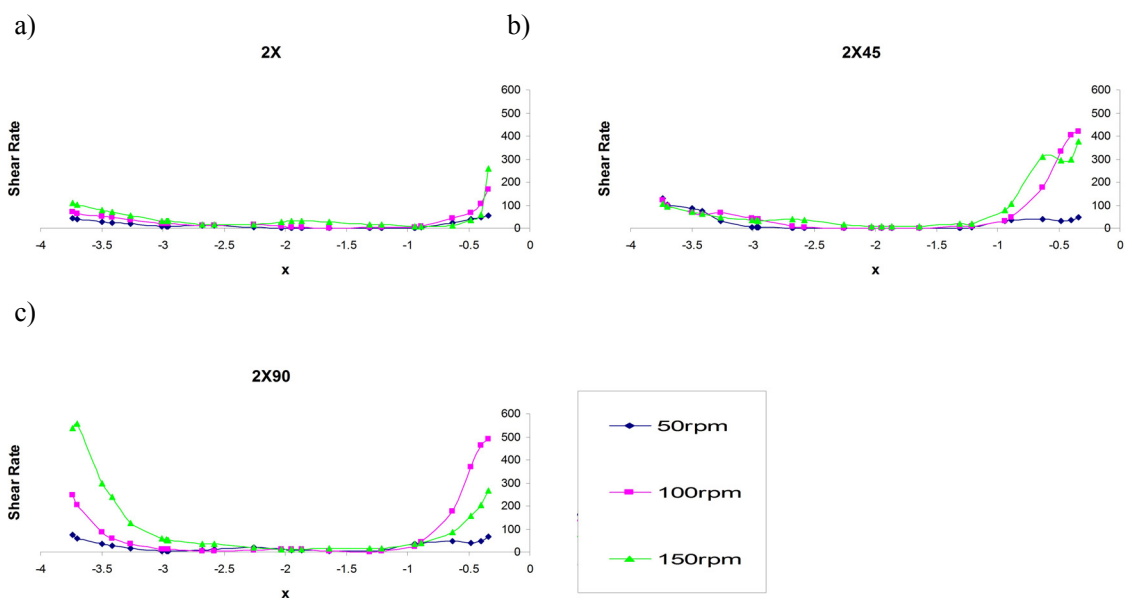


Figure 2.13. Shear rate at different rotation speeds for 2X, 2X45, 2X90.

Increasing the mixer speed increases the mixing index near the barrel wall in the 2X and 2X45 configurations (Figure 2.14). Simple shear flow ($\lambda_{MZ} = 0.5$) is seen in areas of high shear rate noted above. Higher mixing index values indicate more elongational flow which is surprising given that increasing the mixer speed should increase the rotational flow. The converse is true near the barrel center and throughout the 2X90 configuration. This result coincides with the expectation that increased rotation speed increases the rotational contribution to the mixing index.

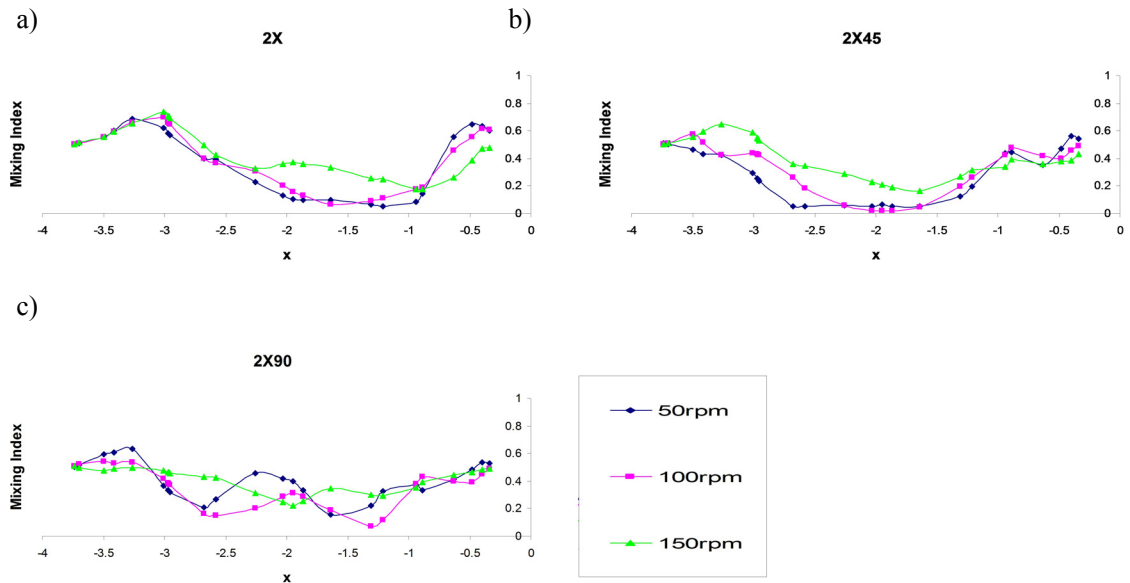


Figure 2.14. Mixing index at different rotation speeds for 2X, 2X45, 2X90.

2.5 Conclusions

Increasing mixer speed increases v_x and v_y values, indicating more mixing, while increasing fluid inflow rate increases v_z values, indicating greater flow-through. In relation, increasing fluid inflow rate increases elongational contribution to the mixing index. Additionally, increasing paddle stagger angle increases v_z near the barrel center and maximum shear rate value.

High mixing index values combined with high shear rates are necessary to break most agglomerates. The 2X90 paddle configuration operating at 100rpm with a fluid inflow rate of 100cc/s shows the highest shear rate. Although 2X90 shows several values indicating simple shear flow, the 2X paddle configuration indicates efficient dispersive mixing with $\lambda_{MZ}=0.7$ at flow rates greater than 20cc/s. Thus 2X is the best paddle configuration to promote efficient dispersive mixing. Examining the 2X90 trend, perhaps increasing the fluid inflow rate would increase the efficiency of dispersive mixing in this configuration.

This research explored a simplified mixer and observed the effect of paddle angle and operating conditions. Backward staggered paddles are expected to enhance mixing. It would be informative to see the effect compared with the forward staggered data shown here. In this work, dispersive mixing is examined. It would be fruitful to investigate distributive mixing as well since this also contributes to the overall quality of the final product.

Chapter 3

NON-NEWTONIAN FLUID MIXING IN A TWIN SCREW MIXER GEOMETRY: 3D MESH DEVELOPMENT, EFFECT OF FLUID MODEL AND OPERATING CONDITIONS¹

3.1 Abstract

Mixing was examined in a Readco continuous mixer (Readco Kurimoto, LLC, York, PA); a mesh was developed for 3D FEM simulation and validated against experimental Newtonian fluid results. The mesh was designed to ensure accuracy in areas with a high velocity gradient while minimizing computational cost. It was utilized for investigation of non-Newtonian fluids, including power-law and Bird-Carreau models. Simple shear flow is seen at high $\dot{\gamma}$ in the center of the mixer; efficient dispersive mixing appears near the barrel wall at all flow rates. Both configurations experience increasing velocity and $\dot{\gamma}$ with mixer speed. Efficient dispersive mixing is observed near the barrel center with parallel paddles. Staggered paddles cause areas of backflow, improving fluid retention time. Under the same operating conditions the Bird-Carreau fluid shows the greater influence of paddle motion, including less flowthrough and significant backflow. Maximum $\dot{\gamma}$ is higher than that seen for the power-law fluid, while mixing index maxima are similar for both fluids.

¹ Reprinted with permission, from Maureen L. Rathod, Bharani K. Ashokan, Lindsay M. Fanning, and Jozef L Kokini, “Non-Newtonian fluid mixing in a twin screw mixer geometry: 3D mesh development, effect of fluid model and operating conditions”, Journal of Food Process Engineering (accepted 2014).

3.2 Practical Application

This work evaluates mixing using complex fluids in a realistic geometry and explores the effect of different operating conditions. Previous work has been confined to mainly Newtonian fluids or simplified geometries. A major benefit of 3D numerical simulation is that it enables comprehensive, non-invasive fluid analysis and determination of mixing quality. The most valuable simulations are those that closely mimic existing equipment scenarios. This information will allow industry users to design more efficient mixers and develop better mixer configurations with lower capital cost. This is particularly important to the dough industry which needs a well-defined mixing profile for both product rheology and machinability.

3.3 Introduction

Mixing is important in many food processes including ingredient distribution, air introduction, and structure formation. These operations are achieved by distributive mixing which determines the movement of particles through the mixer space, and dispersive mixing, which is concerned with breaking clumps, droplets, or bubbles. Measurements of mixing efficiency include calculation of the Manas-Zloczower mixing index, length stretch, area stretch, instantaneous mixing efficiency, time-averaged mixing efficiency, segregation scale, and cluster distribution index. Increasing the complexity of fluids and mixer geometry complicates direct evaluation of mixing. Numerical simulation offers a non-invasive method of obtaining information on shear rate, velocities, and mixing efficiencies. The more realistic the simulation geometry and assumptions are, the more accurate the results will be.

Zhang et al. 2009 examined residence time distribution (RTD) in a co-rotating twin-screw extruder using computational fluid dynamics (CFD) and validated simulation data with experimental results. They used mixing metrics that included area stretch ratio, instantaneous efficiency, and time-averaged efficiency. Both operating conditions (screw speed and feed rate) and kneading disc geometry affected local RTD. Good distributive mixing performance was obtained using small width kneading discs with a gap between them and a large stagger angle.

Muzzio's group (Alvarez et al., 2002; Lamberto et al., 2001; Zalc et al., 2001; Portillo et al., 2008, 2009) explored stirred tank reactors, static mixing flows, and mixing in laminar to turbulent flows using generalized Newtonian fluids. Portillo et al. 2008 explored mixing of acetaminophen and lactose in a continuous convective blender. They studied the effect of blade design, mixer rotation rate, and processing angle on mixing efficiency. The upward processing angle with the outlet of the mixer higher than the inlet led to the largest mean residence time, lowest relative standard deviation (RSD), highest variance reduction ratio (VRR), and thus the best mixing performance. Increasing mixer speed decreased material residence time while increasing the number of blade passes it experienced, resulting in more variability with increasing mixer speed. Portillo et al. 2009 found that blade angle with respect to the shaft affected mixing performance; and that impeller rotation rate had the greatest effect on relative variance, followed by powder cohesion and processing angle. Both rotation rate and processing angle improved residence time, although rotation rate had a greater impact.

Bertrand et al. (2003) used fictitious domain method, a mesh refinement relying on a single reference mesh, to simulate a complex moving-part geometry without

remeshing for every time step as is necessary in classical finite element method (FEM). Internal parts were not meshed but represented by time-dependent control points in the fluid domain where a kinematic constraint was imposed, and updated with the velocity of the moving parts. This method allowed prediction of shear rate in the intermeshing zone and between the screws and the barrel. These gaps were very small and the position varied with time. Thus it was necessary to use mesh refinement based on a single mesh which could adapt locally. When the resulting simulation values were compared to experimental values good agreement was found.

Mixing behavior of simple fluids in simplified geometries has been examined extensively using numerical simulation. Earlier numerical exploration included Newtonian and non-Newtonian fluids in geometries resembling industrial mixers (Connelly and Kokini, 2003, 2004, 2006a, 2006b, 2007; Ashokan et al., 2003; Ashokan, 2008). A Newtonian fluid was also studied in a Brabender Farinograph by Connelly (Connelly and Kokini, 2004; Connelly and Kokini, 2006a, 2006b). The numerical results, using mesh superposition and particle tracking, were validated against experimental values obtained by Prakash and coworkers via laser Doppler anemometry (LDA) (Prakash, 1996; Prakash and Kokini, 1999, 2000; Prakash et al., 1999).

Previous work examined single-screw and twin-screw mixers using two-dimensional (2D) FEM simulations. In the twin screw mixer, there was a symmetric velocity field with material flow between the two halves of the barrel and a small dead zone where the flow changed direction. The area between the two paddles has large pressure and velocity gradients which also impact axial movement of material (Connelly and Kokini, 2007). Although both mixers produce mainly shearing the area with the most

elongational mixing was larger and stronger in the twin screw mixer. Comparing mixing index (λ_{MZ}) and shear rate ($\dot{\gamma}$) showed that elongational flow as well as high shear stress occurred in the intermeshing region. This allowed the twin screw mixer to perform dispersive mixing of clumps, drops, and air bubbles at a lower speed than that necessary in the single screw mixer.

Further work involved 3D simulation of corn syrup within the Readco continuous mixer. In comparing configurations with parallel consecutive paddles (FLAT) to those with 45° staggered paddles (45F and 45R), it was found that staggered paddles caused limited flow disruption, and did not contribute to overall forward or reverse flow (Vyakaranam et al., 2012). Non-Newtonian fluid mixing was explored in an abbreviated mixer geometry representing a two paddle portion of the mixing region (Rathod and Kokini, 2013). It was found that increasing mixer speed increased the x and y velocity components (v_x and v_y) while increasing fluid inflow rate increased the z velocity component (v_z) as well as the elongational contribution to λ_{MZ} . Highest $\dot{\gamma}$ was seen in the 2X90 configuration but the most efficient dispersive mixing was found in the 2X configuration.

In this study the objectives were to expand on previous 2D mesh continuous mixer work to obtain an optimal 3D mesh, allowing a more complete picture of fluid motion within the flow domain. After validating this mesh using experimental data the goal was to combine it with previous numerical examination of non-Newtonian fluid mixing within an abbreviated twin-screw co-rotating mixer geometry. Extending the simulation to encompass the full nine-paddle length of the mixing region gives a more accurate model of the studied geometry. Using non-Newtonian fluids like a power-law

model fluid and a Bird-Carreau fluid will better represent food products which are largely non-Newtonian, and exhibit the difference in fluid behavior with the same mixer and operating conditions.

3.4 Materials and Methods

3D FEM simulations were performed using the Polyflow suite of programs from ANSYS, Inc.: Gambit: mesh generator, Polyflow: FEM solver, and CFX-Post: graphic post-processor. Further description of these programs and their use can be found in Connelly and Kokini 2007. Hardware included a Dell Precision 690 workstation with Dual Core Xeon processors and 16 GB RAM (Dell Inc., Round Rock, TX). Parameters chosen included fully-developed Poiseuille flow between the paddles and barrel, zero tangential velocity and normal force at the outflow, no slip at the walls, isothermal conditions, inertia taken into account, and gravity neglected. Mesh superposition was used to accommodate the paddle motion and resulting overlap between the barrel and paddle meshes. The paddle mesh is superimposed on the barrel mesh and a penalty term is added to the conservation equation to determine if a given barrel element falls within the fluid or solid domain. In order to avoid fluid loss into the solid paddle, a compressibility factor is added to the continuity equation. The conservation and continuity equations are modified as seen below (Vyakaranam et al., 2012; Rathod and Kokini, 2013).

$$H(\mathbf{v} - \bar{\mathbf{v}}) + (1 - H)(-\nabla p + \nabla \cdot \mathbf{T} - \rho \mathbf{a}) = 0 \quad \text{Equation 3.1}$$

where \mathbf{v} is velocity, $\bar{\mathbf{v}}$ is local velocity, p is pressure, \mathbf{T} is the extra stress tensor, and \mathbf{a} is acceleration. H is the step function which is 0 outside the moving part and 1 inside,

allowing the determination of whether a barrel mesh element is considered fluid or solid for the purposes of the conservation equation calculation.

$$\nabla \cdot \mathbf{v} + \frac{\beta}{\eta} \Delta p = 0 \quad \text{Equation 3.2}$$

where η is the local viscosity.

Fluids studied here include Newtonian corn syrup, used in the mesh development and validation, as well as a non-Newtonian 2% aqueous carboxymethyl cellulose (CMC) solution and a Bird-Carreau model fluid. Corn syrup had a viscosity of 54 Poise and density of 1.42 g/cm³. The CMC solution was modeled as a power-law fluid whose density was 1.0068 g/cm³. Fluid characteristics were experimentally measured at room temperature (23-25°C) (Prakash, 1996).

$$\eta = K(\lambda \dot{\gamma})^{n-1} \quad \text{Equation 3.3}$$

where $K=15.74 \text{ N s}^n \text{ m}^2$, $n=0.397$, and $\lambda=1$.

The Bird-Carreau fluid was defined according to Equation 3.4

$$\eta = \eta_{\infty} + (\eta_0 - \eta_{\infty})(1 + \lambda^2 \dot{\gamma}^2)^{\frac{n-1}{2}} \quad \text{Equation 3.4}$$

where $\eta_0=100,000$ poise, $\eta_{\infty}=11,111.11$ poise, $\lambda=60\text{s}$, $n=0.2$ (Connelly and Kokini, 2004).

Each simulation was run for one rotation at mixer speeds of 50rpm, 100rpm, and 150rpm. Results were recorded every 10° or 0.033333s at 50rpm, 0.016667s at 100rpm, and 0.011111s at 150rpm. Fluid inflow rates of 20cc/s, 40cc/s, 53cc/s, 55.31cc/s, 75cc/s, and 100cc/s were used. The horizontal axis is x , the vertical axis is y , and the axis from the inlet to the outlet of the mixer is z .

3.4.1 Radial and axial mesh density

The Readco continuous mixer geometry was drawn in Gambit and a mesh was imposed upon it. Six different meshes were developed by varying the number of elements in the radial direction and the relative size of these elements. The initial mesh was created with uniform element size between the shaft and the barrel wall (Figure 3.1). Next, a radial mesh was made with larger elements near the mixer shaft and smallest elements near the wall where more mixing effects are experienced. Further refinement led to a radial-8-16 mesh with half of the distance between the shaft and the wall meshed with 8 equal intervals and the remaining portion meshed with elements of decreasing size as one approached the wall. The radial-8-12 mesh was formed in the same way as the radial-8-16, but with 12 elements between the center point and the wall. In addition, radial-6-9 and radial-4-6 meshes were created from the radial-8-16 mesh with 6 and 4 elements from the shaft to the center point and 9 and 6 elements from the center point to the wall, respectively. Starting from the radial-4-6, a radial-4-6-azi mesh was formed with an azimuthal gradation half that of the previous meshes.

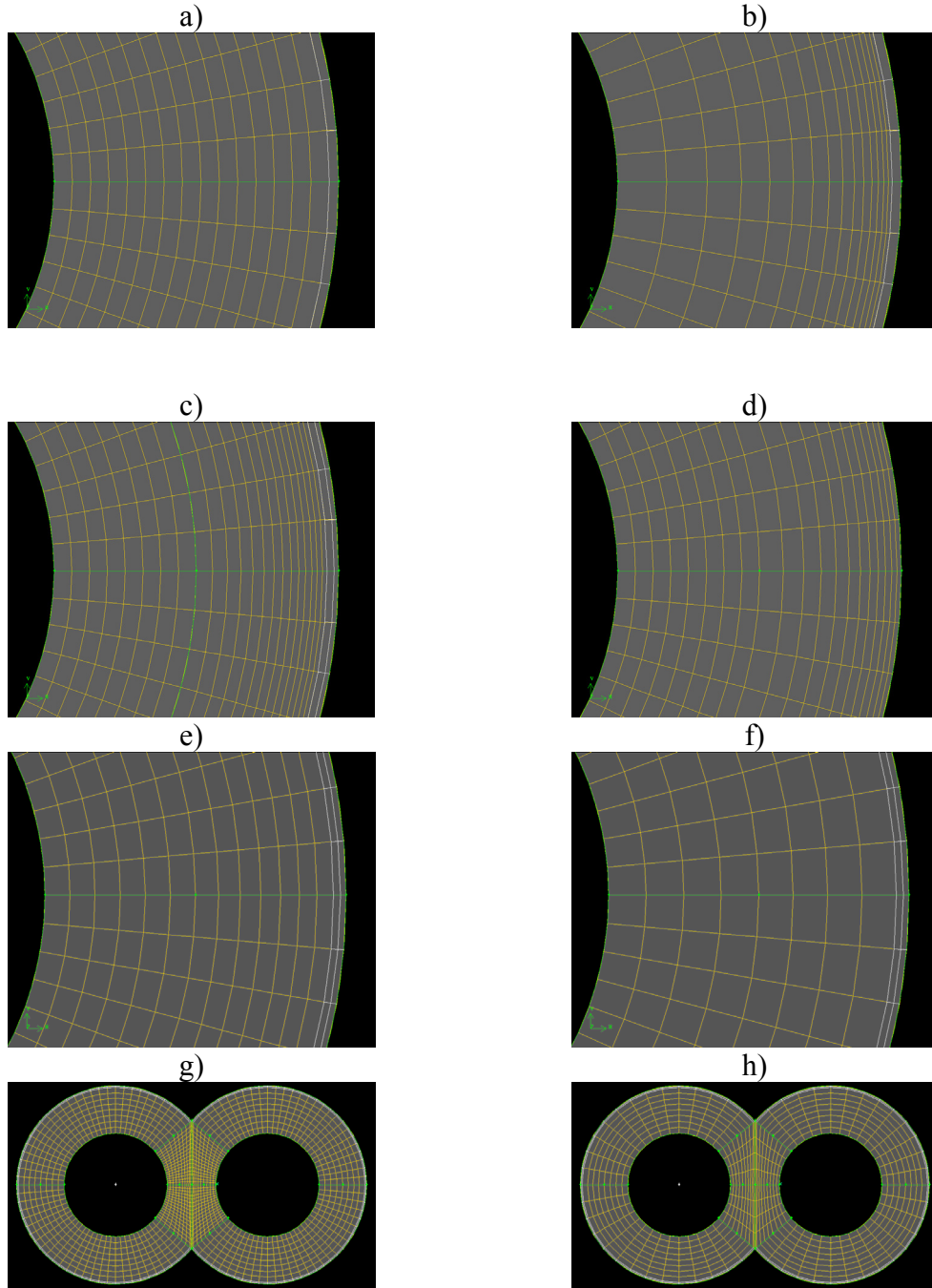
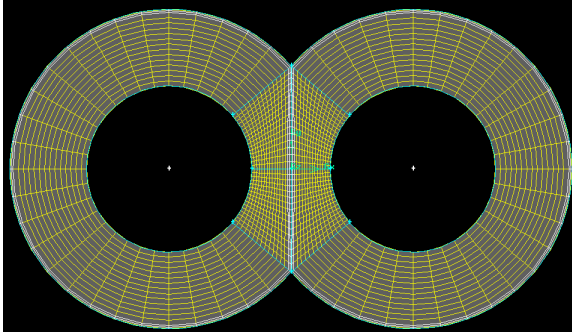


Figure 3.1. Radial gradation of mesh density: a) Uniform, b) Radial, c) Radial-8-16, d) Radial-8-12, e) Radial-6-9, f) and g) Radial-4-6, h) Radial-4-6-azi.

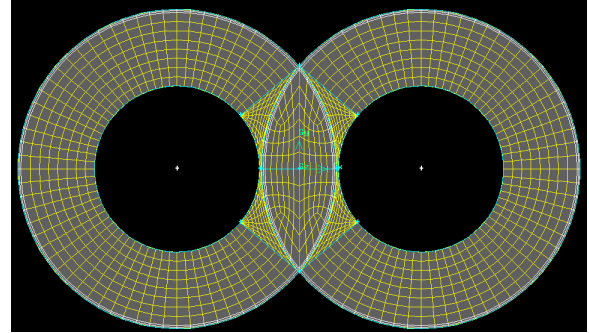
Mesh #1 was created with 16 uniform elements in the radial direction, including 2 boundary layer elements, and 28 elements in the azimuthal direction. The intermeshing region was also meshed with 28 intervals along the inside of the shafts. Meshes #2, 3, and

4 (Figure 3.2) were designed to avoid overlapping of barrel elements by both paddles in the intermeshing region. The addition of a boundary layer consisting of at least two mesh elements assured that there would be a small gap between the two solid paddles at all times. This prevented the contact of the two paddles during their rotation.

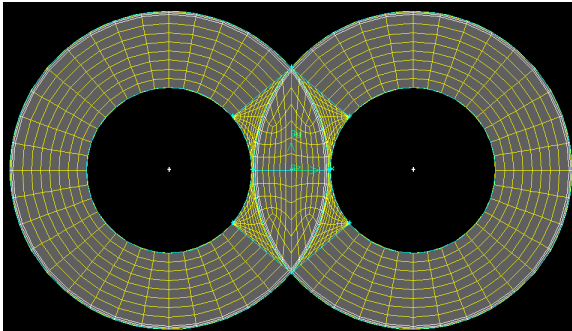
a) Mesh #1



b) Mesh #2



c) Mesh #3



d) Mesh #4

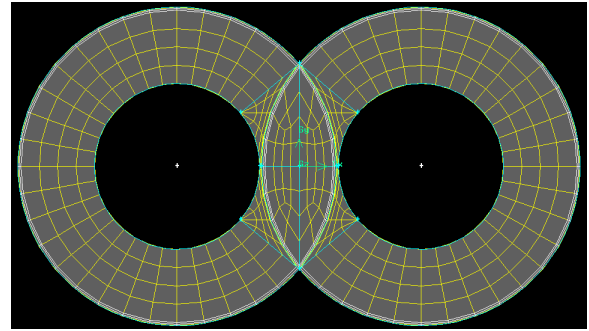


Figure 3.2. 2D meshes with varying radial mesh density a) Mesh #1, b) Mesh #2, c) Mesh #3, d) Mesh #4 (Ashokan, 2008).

Meshes in Figure 3.3 were developed to examine the effect of varying the number of axial elements on computational accuracy and cost. Each has an extra half-paddle width added to the length of the barrel. This width corresponds to an addition of two mesh elements at both ends of the barrel to isolate the area of interest from entrance and exit effects. This side view of the barrel contains the paddle width as well as two

elements for both entrance and exit lengths. The paddle area is meshed using two, three, four, and five elements and the velocities obtained with each mesh are compared.

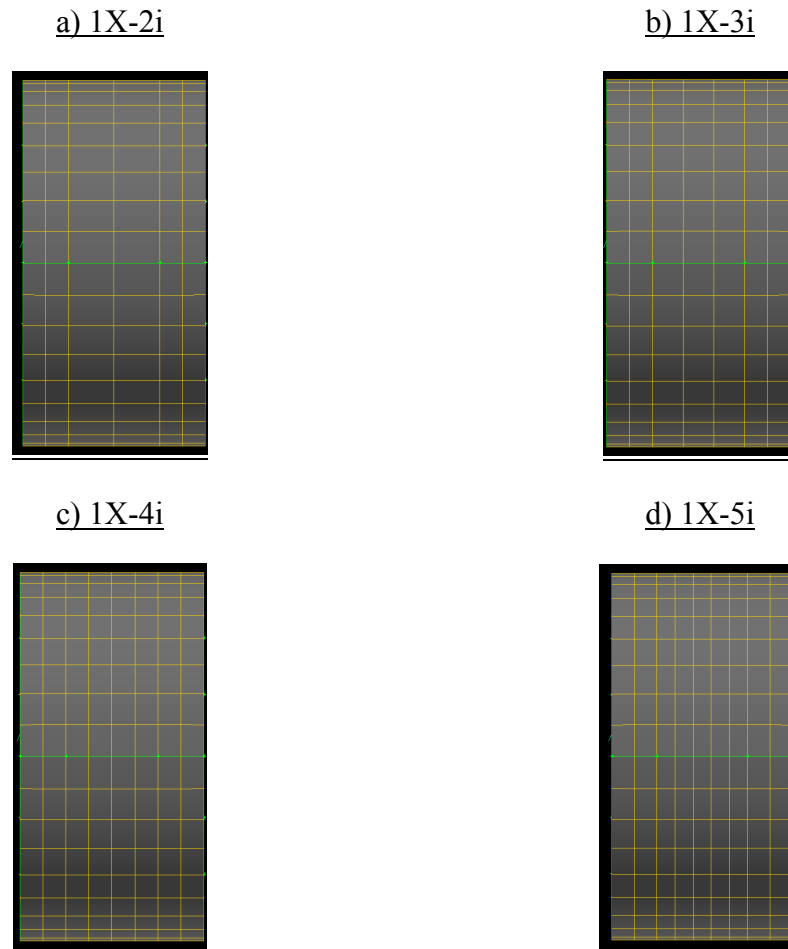


Figure 3.3. Barrel meshes with a) 2, b) 3, c) 4, d) 5 mesh intervals in the region of the paddles (Ashokan, 2008).

The initial three and final three paddles were fused in this geometry. In order to evaluate the effect of fusing these paddles on the quality of simulation results, a three-paddle-pair mesh was generated with gaps between the paddles as well as a mesh containing one paddle pair with a thickness equal to three paddles without gaps. Additionally, the fused paddle mesh was created with 5 and 9 axial mesh intervals (Figure 3.4).

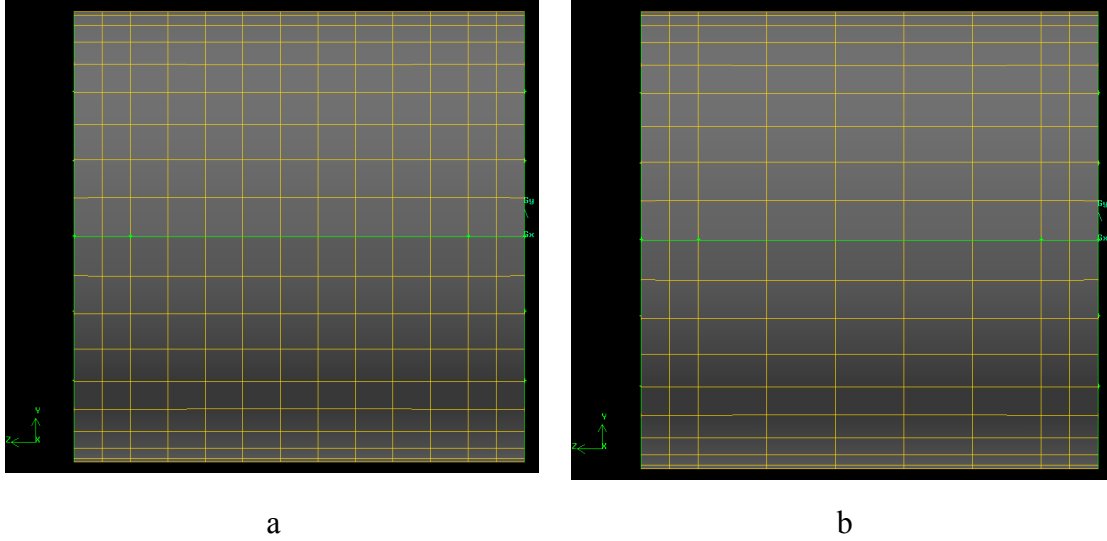


Figure 3.4. Three pair paddle mesh with a) nine, b) five mesh intervals.

3.4.2 Determination of mesh quality

3.4.2.1 Equiangle skew

The first measure of the quality of a mesh is an estimation of the degree of skewness in the elements. Ideally all elements will be square in shape but when the geometry has curvature or corners this is not possible. The equiangle skew defined in Equation 3.5 provides a quantitative test of the skewness of the mesh:

$$Q_{EAS} = \max \left\{ \frac{\theta_{\max} - \theta_{eq}}{180 - \theta_{eq}}, \frac{\theta_{eq} - \theta_{\min}}{\theta_{eq}} \right\} \quad \text{Equation 3.5}$$

where θ_{\max} and θ_{\min} are the maximum and minimum angles in degrees between the edges of the element, and θ_{eq} is the characteristic angle corresponding to an equilateral cell of similar form, ($\theta_{eq}=60^\circ$ for triangular or tetrahedral elements and $\theta_{eq}=90^\circ$ for quadrilateral or hexahedral elements). Thus equiangle skew varies from 0 (for a quadrilateral element) to 1 (for a degenerate element). For 3D meshes, an average $Q_{EAS}=0.4$ is considered high-quality. Values up to 0.6 are considered to be good and those

between 0.6 and 0.9 are fair to poor elements. Elements with skew values greater than 0.9 are unacceptable (Gambit, 2007).

3.4.2.2 Stretch ratio

A second measure of the mesh quality is defined by how much a mesh is stretched from an ideal geometry. This is given by the stretch ratio defined in Equation 3.6 below:

$$Q_s = 1 - \sqrt{\frac{K \min(s_1, s_2, \dots, s_m)}{\max(d_1, d_2, \dots, d_n)}} \quad \text{Equation 3.6}$$

where d_i is the length of diagonal i , s_j is the length of the element edge j , and n and m are the total numbers of diagonals and edges, respectively. This quality measurement can only be applied to quadrilateral and hexahedral elements. For quadrilateral elements, $n = 2$, $m = 4$, and $K = 2$; for hexahedral elements, $n = 4$, $m = 12$, and $K = 3$. Stretch ratio varies from 0 to 1 where $Q_s=0$ for an equilateral element and $Q_s=1$ for a completely degenerate element (Gambit, 2007).

The selected nine paddle meshes are shown in Figure 3.5. In this geometry the paddles have a thickness of 1.27cm and the barrel includes half-paddle (0.635cm) entrance and exit lengths as well as a 0.03cm axial gap between successive paddles. Data collected along Lines 1 and 2 (Figure 3.6) is used to compare simulation and experimental results. The paddle configurations in Figure 3.7 were used to explore the effect of rotation speed, fluid inflow rate, and paddle angle, where 9X is composed of paddles which are parallel to each other and 9X45 contains a section of paddles at a 45° to each other in the central mixing region. Line 3 is a modification of Line 2, located at $z=7.165$. This position was chosen to capture fluid motion in the center of the mixer among the paddles modeled with gaps.

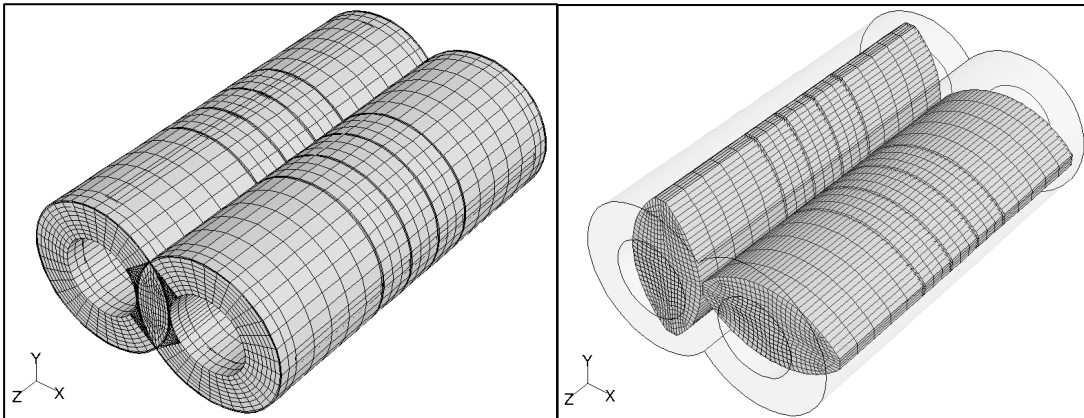


Figure 3.5. Nine paddle a) barrel, b) paddle meshes.

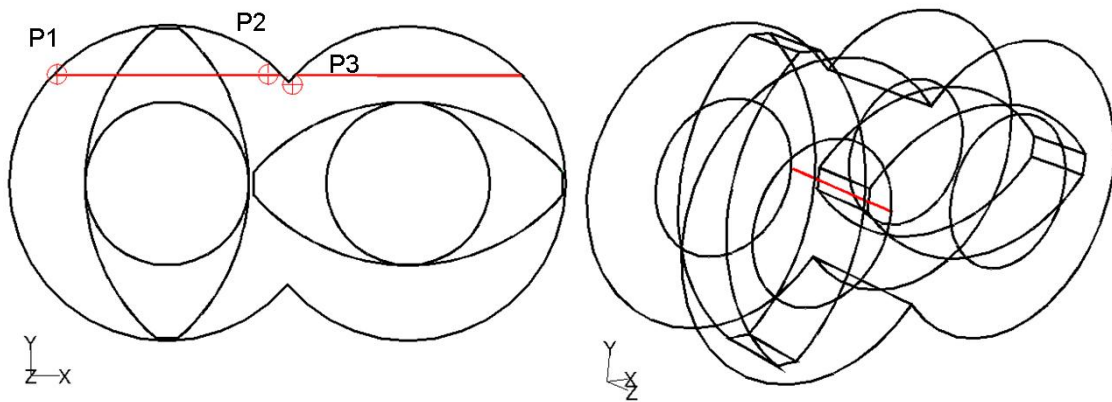


Figure 3.6. Position of a) Line 1, Points P1, P2, P3, b) Line 2 in the mixer.

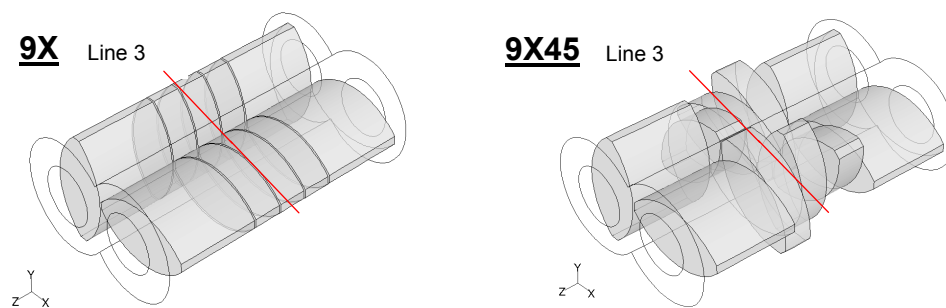


Figure 3.7. Mixer configurations and position of Line 3 a) parallel paddles, b) 45° staggered paddles.

3.4.3 Simulation validation

3.4.3.1 Experimental determination of velocity profiles

Experimental work, used here for numerical validation, was performed using a Plexiglas barrel (Arkema Inc., King of Prussia, PA) and clear fluid (Globe corn syrup 1142) to enable laser travel with minimal optical disruption. The mixer was fully filled, with a speed of 100rpm. Measurements were taken at the fourth pair of paddles from the mixer inlet. Velocities at three points were compared. These points were chosen to examine the clearance area between the paddle and barrel wall and the intermeshing region between the two paddles (Ashokan, 2008). The equipment set-up is shown in Figure 3.8. The advantages of LDA are that it does not disturb the flow, can be measured throughout the vessel, and all three dimensions can be examined at once (Fanning, 2009).

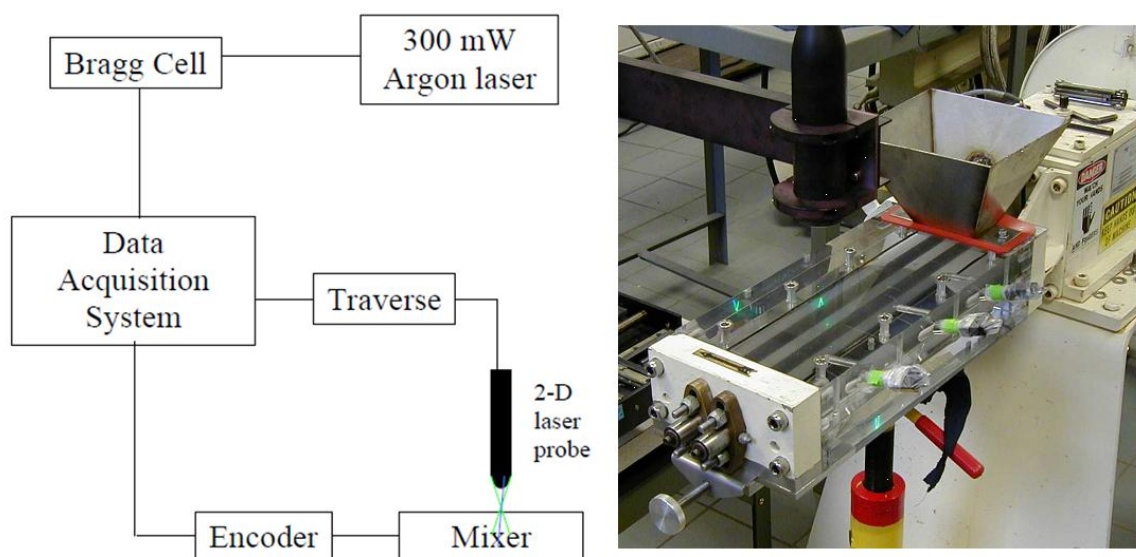


Figure 3.8. LDA system a) Schematic (Fanning, 2009), b) Probe and beams (Ashokan, 2008).

Beginning at the entrance of the mixer, the geometry included two feed screws, nine aligned flat paddles, a feed screw, and a reverse helical paddle nearest the mixer exit. Shaft orientation relative to the data point was measured by an encoder on the shaft.

Forty data points were obtained across a given cross-section, with the traverse moving from point to point in numerical order. In order to calculate velocity gradient, additional measurements were taken 2mm from the original point in the x , y , and z directions. Velocity was averaged at each point and the position corrected for refraction due to the fluid and barrel. The optical similarity between the fluid and barrel materials allowed the complete volume to be treated as a solid and the curvature to be neglected.

A two color Argon ion laser Doppler anemometer (Dantec Dynamics, Mahwah, NJ) was used. The laser was sent to a Bragg cell where it was split and one beam experienced a frequency shift. This allowed the measurement of velocity gradient and direction. Two perpendicular beams were used to measure each velocity component. Beams of the same color were placed at an angle to each other and measurements were taken at the point of their intersection. This crossing defined the measurement volume with interference fringes appearing as light and dark areas. The spacing between fringes was dependent upon the angle between the beams as particles in the measurement volume scattered laser light. Frequency was measured and converted to velocity with Equation 3.7, where v_D was measured and other parameters were determined by the LDA settings (Table 3.1).

$$\mathbf{v} = \frac{v_D \lambda}{2 \sin \alpha} \quad \text{Equation 3.7}$$

where \mathbf{v} is fluid velocity, v_D is the Doppler frequency of the scattered light, λ is the wavelength, and α is the half-angle between the beams. The probe was on a 3D traverse to allow accurate positioning within 0.1mm; and the encoder was able to measure rotation every degree through the complete 360 degree rotation within $\pm 3^\circ$. Measurements were made from the top of the mixer.

Table 3.1. Settings used for LDA system (Fanning, 2009)

LDA Settings		
Probe Lens Focal Length (mm)	120	
Bragg Cell Frequency Shift (MHz)	40	
	Blue Beam	Green Beam
Wavelength, λ (nm)	488	514.5
Number of Fringes	60	60
Fringe Spacing (μm)	1.5602	1.6449

LDA velocity data obtained within the mixer was validated using a couette geometry. The inner cylinder had a diameter of 69mm and rotated at 20rpm, while the outer cylinder had a diameter of 104mm. LDA measurements were made along the center line of the cylinders. Tangential and axial velocities were measured. Axial velocity was expected to be 0 m/s with negligible secondary flows. Relatively low angular velocities were seen with negligible inertial and centrifugal forces (Fanning, 2009). Velocity was measured at five points and corrected for refraction using Equation 3.8. The intersection point was obtained from Equation 3.9 and the corrected velocity calculated using Equation 3.10.

$$C_f = \frac{1}{n_f} \left[1 + \left(\frac{r_a}{R_o} \right) \left[\left(\frac{R_o}{R_i} \right) \frac{\left(\frac{n_f}{n_w} - 1 \right)}{n_f} + \frac{n_w - 1}{n_w} \right] \right]^{-1} \quad \text{Equation 3.8}$$

$$r_f = C_f r_a \quad \text{Equation 3.9}$$

$$V_{\phi f} = C_f V_{\phi a} \quad \text{Equation 3.10}$$

where C_f is the correction factor for fluid velocity, n_f is the refractive index of the fluid, r_a is the radius of beam intersection without refraction, R_o is the outer radius of the cylinder wall, R_i is the inner radius of the cylinder wall and n_w is the refractive index of the cylinder wall. The true radius of the beam intersection position with refraction is r_f , $V_{\phi f}$ is the corrected tangential velocity and $V_{\phi a}$ is the measured tangential velocity.

3.4.3.2 Calculation of simulation and experimental difference

In order to compare the experimental data with simulations results, Root Mean Square (RMS) % difference was calculated using Equations 3.11 and 3.12.

$$RMS = \frac{\sqrt{\sum_n (v_s - v_e)^2}}{n} \quad \text{Equation 3.11}$$

$$\%RMS = \frac{RMS}{(v_{e_{\max}} - v_{e_{\min}})} \times 100 \quad \text{Equation 3.12}$$

where v_s and v_e are the simulated and experimental velocity magnitudes and n is the number of measurement points.

3.4.4 Calculation of mixing index

Dispersive mixing was characterized by the Manas-Zloczower mixing index λ_{MZ} (Cheng and Manas-Zloczower, 1990).

$$\lambda_{MZ} = \frac{|\mathbf{D}|}{|\mathbf{D}| + |\mathbf{\Omega}|} \quad \text{Equation 3.13}$$

where $|\mathbf{D}|$ is the magnitude of the rate of deformation tensor and $|\mathbf{\Omega}|$ is the magnitude of the vorticity tensor. When $\lambda_{MZ}=0$ it indicates pure rotational mixing, $\lambda_{MZ}=0.5$ indicates simple shear flow, $\lambda_{MZ}=0.7$ indicates efficient dispersive mixing, and $\lambda_{MZ}=1$ indicates pure elongational flow. This measure is not frame-invariant (Manas-Zloczower, 1997)

and shear stress magnitude must be taken into account when relating it to dispersive mixing (Yang and Manas-Zloczower, 1992).

3.5 Results and Discussion

3.5.1 Selection and validation of mesh density

Each of the meshes with varying radial density (Figure 3.2) was evaluated for its equiangle skew and stretch ratio using Equations 3.5 and 3.6 above. Due to the intricate nature of the geometry, many elements are not square but in fact stretched (Table 3.2). Despite this, data comparisons with experimental work show good correlation. Using the different meshes, velocity magnitudes obtained along Line 1 are compared in Figure 9. Mesh #3 is found to be the optimum radial mesh because it does not allow overlapping like Mesh #1, is more accurate than Mesh #4, and shows similar accuracy to Mesh #2 without the added cost of additional refinement (Table 3.3) (Ashokan, 2008). Thus Mesh #3 is chosen for use in the 3D mesh development.

Table 3.2. Quality of meshes with varying radial gradation (Ashokan, 2008)

Mesh	Number of elements	Equiangle skew > 0.5 (% elements)	Stretch ratio > 0.5 (% elements)
Mesh #1	1920	0	54.27
Mesh #2	1632	14.46	31.86
Mesh #3	1072	22.01	48.51
Mesh #4	512	19.53	46.88

Table 3.3. Comparison of RMS % difference at points P1, P2 and P3 for the four 2D meshes investigated using corn syrup with a flow rate of 53cc/s into the mixer (Ashokan, 2008)

	P1		P2	P3
	v_x	v_y	v_x	v_x
Mesh #1	9.73	2.40	6.92	23.43
Mesh #2	9.66	3.12	7.67	20.57
Mesh #3	9.90	3.22	7.28	20.40
Mesh #4	10.86	4.46	8.59	16.05

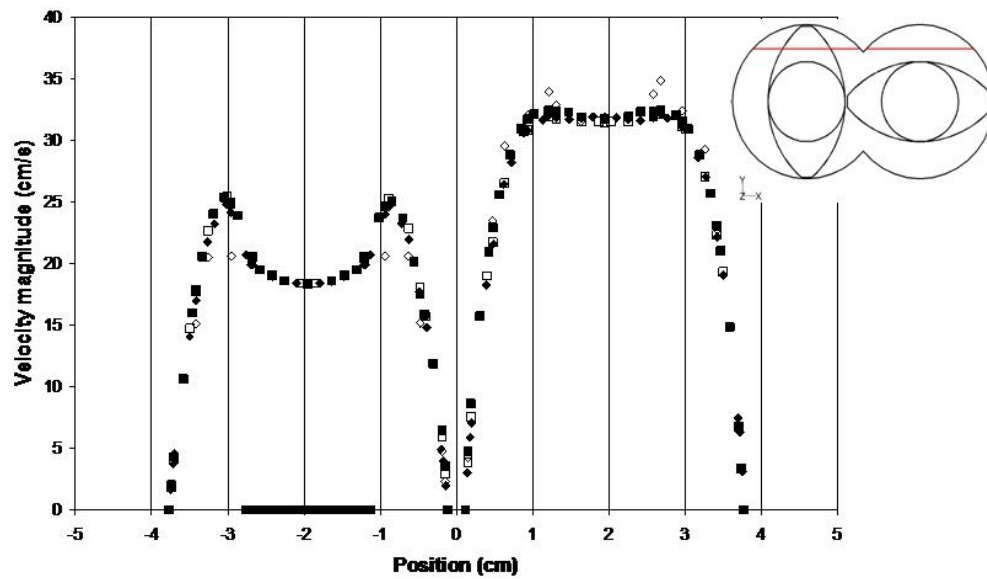


Figure 3.9. Comparison of velocity magnitudes along Line 1 for Mesh #1 (■), Mesh #2 (◆), Mesh #3 (□) and Mesh #4 (◇) (Ashokan, 2008).

For the axial meshes (Figure 3.3), velocity magnitude data is examined along Line 2 and plotted in Figure 3.10. The mesh with three axial elements is chosen because it produces similar velocity results to those found with four and five elements without the added computational cost. This mesh is used when exploring meshes including more than one pair of paddles.

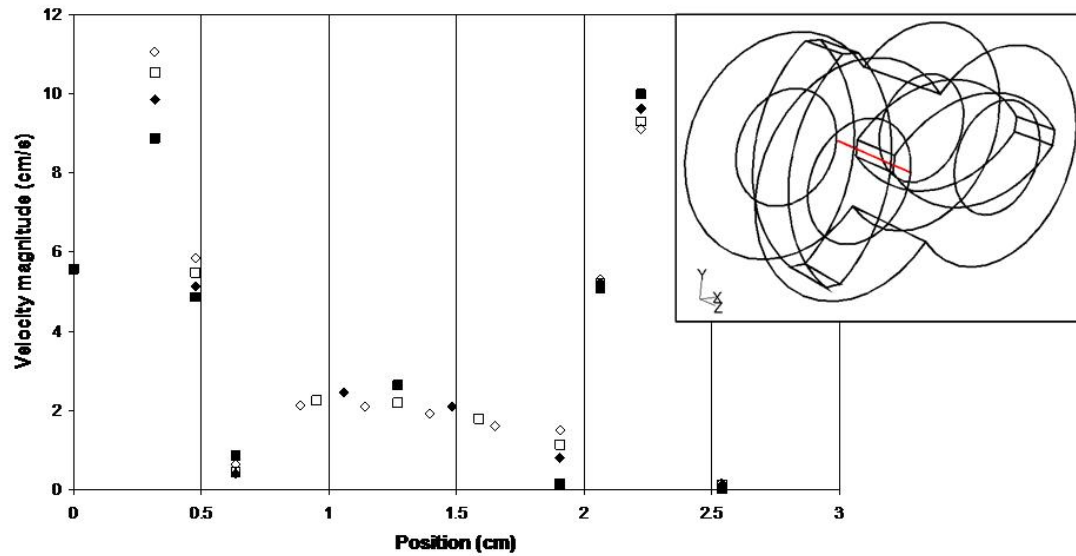


Figure 3.10. Velocity comparison along Line 2 for meshes with 2 (■), 3 (◆), 4 (□) and 5 (◇) axial mesh intervals (Ashokan, 2008).

After having determined the number of axial mesh intervals, the next step is to determine the number of paddle pairs necessary for good correlation between simulation and experimental data. The data in Figure 3.11 are RMS % difference values at point P1. V_x and v_y show a small decrease in RMS % difference in the axial center of the mixer with increasing length. Due to their similarity, only v_x is shown here. A larger impact is seen for v_z as a visible decrease in RMS % difference with each additional paddle pair. The third paddle pair in the five paddle pair geometry exhibits well-developed flow, isolated from entrance and exit effects. This demonstrates the contribution of additional paddle pairs in minimizing these disruptions.

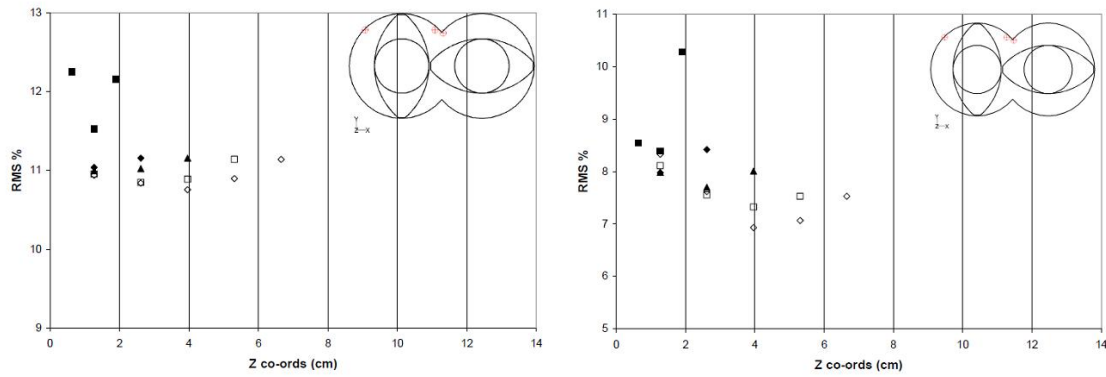


Figure 3.11. RMS % difference at point P1 between experimental and simulated values as a function of axial location for simulation geometries having 1 pair (■), 2 pairs (◆), 3 pairs (▲), 4 pairs (□) and 5 pairs (◇) of paddles in the a) v_x velocity component, b) v_z velocity component (Ashokan, 2008).

The velocity magnitude comparison between the three paddle pair axial meshes in Figure 3.4 is shown in Figure 3.12. Variation in velocity magnitude is best captured in the mesh containing gaps as the fluid follows a narrow path between the paddles and a wider one in the gap, leading to greater velocity magnitude in the gap. Without gaps the values are still close in magnitude and there is no significant difference in accuracy between the nine and five-interval axial meshes. Thus the five-interval fused axial mesh is chosen for further work.

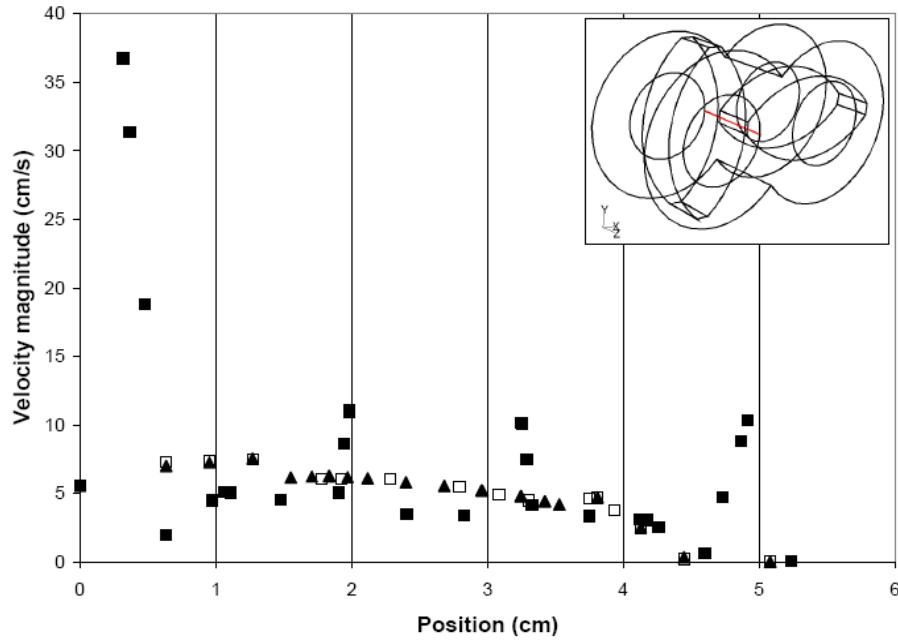


Figure 3.12. Velocity comparison along Line 2 for 3 paddle pair meshes with gaps (■), fused 3 paddle pair meshes with 9 (▲) and 5 (□) axial intervals (Ashokan, 2008).

From this point the effect of adding an increased entrance length is explored and compared with the result of incorporating additional paddle pairs. Simulation data obtained at the eighth paddle of the nine paddle geometry correlates most closely to experimental data obtained at the fourth paddle. As seen with the smaller number of paddles pairs above, increasing the number of paddle pairs causes a small decrease in RMS % difference for v_x (Figure 3.13). A similar trend is noted for v_y , thus it is not repeated here. A greater impact is made on v_z with additional decreases in RMS % difference with an increasing number of paddle pairs. No increase in v_x or v_y accuracy is achieved with the inclusion of a longer entrance length. Even more problematic, a decrease in v_z accuracy is seen. Thus the nine paddle pair geometry was selected.

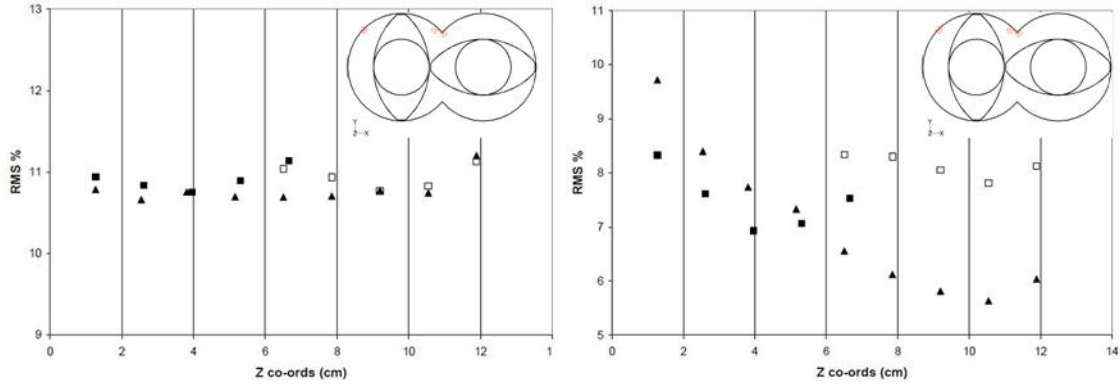


Figure 3.13. RMS % difference at point P1 between experimental and simulated values as a function of axial location for simulation geometries having 5 pairs (■), 5 pairs with increase in entrance length (□) and 9 pairs (▲) of paddles in the a) v_x velocity component, b) v_z velocity component (Ashokan, 2008).

3.5.2 Effect of flow rate on mixing in a power-law fluid

After examining mixing of a non-Newtonian 2% CMC solution in a shortened, two paddle pair mixer (Rathod and Kokini, 2013), the study was extended to the full, nine paddle mixing region. Data displayed here was obtained along Line 3. Looking at several fluid inflow rates in 9X, there is a similar trend for v_x , excepting the 40cc/s simulation (Figure 3.14). The negative v_x in this area of the mixer mirrors the counterclockwise motion of the paddles. In 9X45 there are lower magnitude v_x peaks and flatter curves than the 9X data. This implies that staggering the paddles produces a steadying effect on v_x , isolating it from fluctuations with fluid inflow rate. V_x values at 20cc/s, 40cc/s, and 55.31cc/s follow each other closely, but the values at 75cc/s and 100cc/s show an increase in magnitude indicating the promotion of fluid reorientation at these flow rates in 9X45.

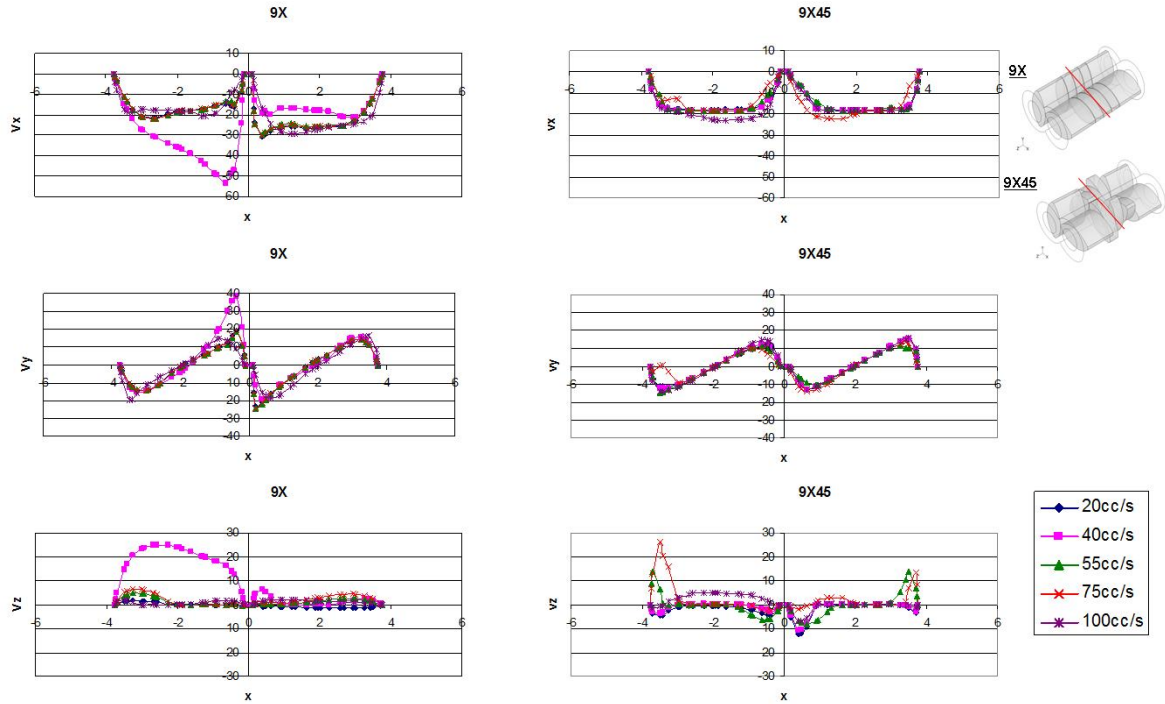


Figure 3.14. Power-law fluid velocity components along Line 3 at different fluid inflow rates and stagger angles a) 9X v_x , b) 9X45 v_x , c) 9X v_y , d) 9X45 v_y , e) 9X v_z , f) 9X45 v_z .

For different flow rates, 9X v_y values follow the same trend with positive values corresponding to fluid being pushed upward and negative values to the fluid being pushed downward according to the counterclockwise motion of the paddles. The exception is the 40cc/s simulation, as was the case for v_x . It is possible that the circumstances at 40cc/s in 9X form a unique situation with regard to the velocity components, enhancing flow on the left side of the mixer. In 9X45, there is a similar trend among the different flow rates, comparable to 9X, although the maximum magnitudes are lower. Thus staggered paddles also insulate v_y .

Increasing fluid inflow rate, up to 75cc/s, increases v_z magnitude in both configurations. The 100cc/s simulation data has lower magnitudes, in areas comparable to the 20cc/s data. This is interesting due to the fact that the fluid enters the mixer in the z

direction and thus increasing its rate is expected to increase v_z . At higher flow rates it would not be surprising to see v_z as the dominant fluid motion. Most noticeably, 9X45 shows areas of negative v_z , indicating backflow. This allows the fluid to remain longer within the mixer, providing opportunity for further mixing.

The 9X $\dot{\gamma}$ trend is similar up to 75cc/s (Figure 3.15). Highest $\dot{\gamma}$ peaks occur in the center of the mixer. At 100cc/s, the $\dot{\gamma}$ profile is more like that found in 9X45. The lower $\dot{\gamma}$ seen in the center of the mixer implies that the fluid is not passing directly through the mixer in this area, but is being reoriented. This is striking to see at the highest flow rate in the parallel configuration. One would anticipate a higher flow rate speeding fluid through the mixer on a nearly straight path, creating a good scenario for shear flow.

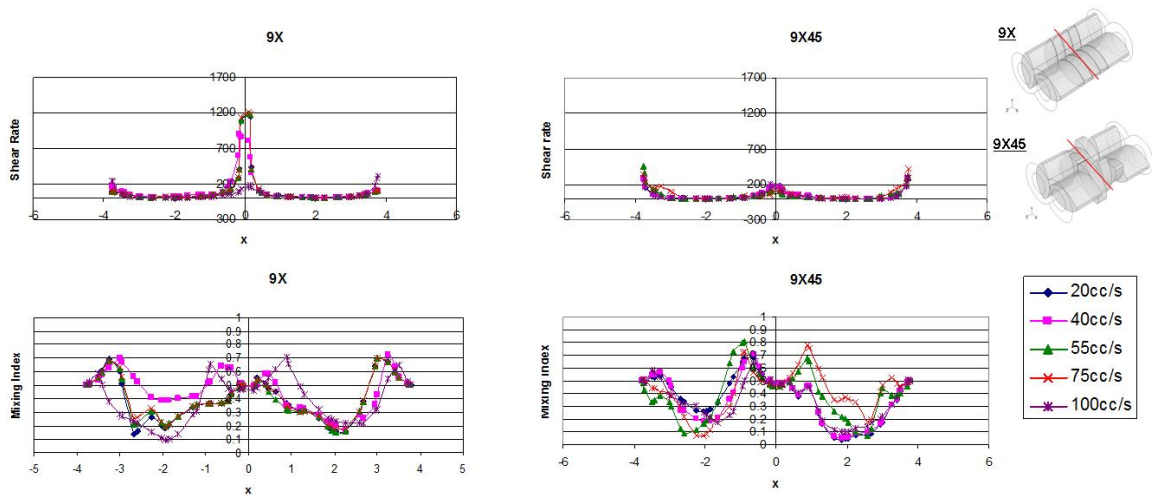


Figure 3.15. Power-law fluid shear rate and mixing index along Line 3 at different fluid inflow rates and stagger angles a) 9X $\dot{\gamma}$, b) 9X45 $\dot{\gamma}$, c) 9X λ_{MZ} , d) 9X45 λ_{MZ} .

All flow rates show areas of efficient dispersive mixing ($\lambda_{MZ}=0.7$) around $x=3$ and $x=-3$. The 100cc/s simulation also shows additional areas near $x=1$ and $x=-1$. Lowest λ_{MZ} is found near the center of the paddles, where the fluid experiences more rotational flow. In 9X45, the minimum values are closer to zero than those in 9X, indicating more

rotational flow. The 55.31cc/s and 75cc/s fluid inflow rates show strong elongational contribution which does not continue when the flow rate is increased to 100cc/s. At this flow rate, λ_{MZ} values are similar to those found at lower flow rates, with no points experiencing efficient dispersive mixing.

3.5.3 Effect of mixer speed on mixing in a power law fluid

Increasing mixer speed increases v_x and v_y magnitude in 9X (Figure 3.16). This is not surprising as the counterclockwise paddle rotation moves fluid both vertically and horizontally in the mixer. In contrast, 9X45 data indicates that staggered paddles produce a more consistent v_x at a given mixer speed. Staggering the paddles appears to have a negative effect on v_x and v_y , implying less fluid reorientation. This corresponds with the limited disruption found by Vyakaranam et al. (2012).

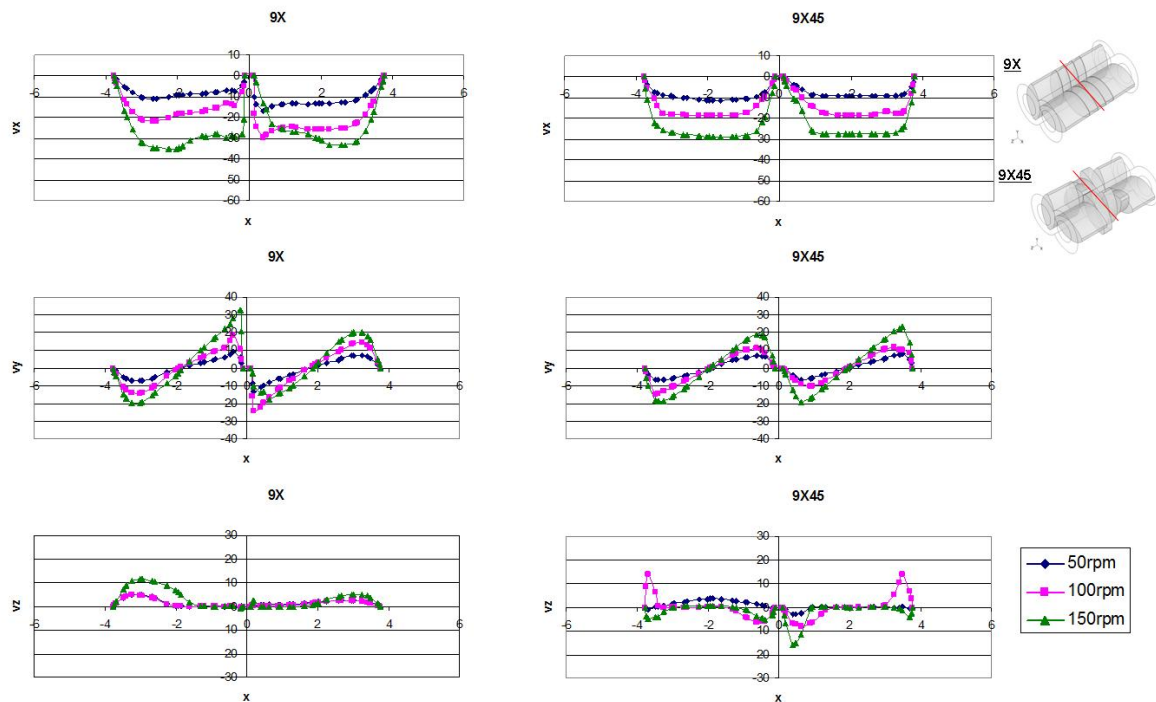


Figure 3.16. Power-law fluid velocity components along Line 3 at different mixer speeds and paddle stagger angles a) 9X v_x , b) 9X45 v_x , c) 9X v_y , d) 9X45 v_y , e) 9X v_z , f) 9X45 v_z .

The effect of increasing v_z with mixer speed is more pronounced on the left side of the mixer, where the current paddle position allows more flowthrough. 9X45 exhibits greater magnitude maximums and minimums than 9X. The benefit anticipated as a result of backflow needs to be balanced against the negative effect caused by increased flowthrough. 100rpm shows more flowthrough near the barrel wall, but also more backflow near the center of the mixer. Further increasing mixer speed to 150rpm promotes backflow in the center and generates small areas of backflow near the barrel wall.

Increasing 9X $\dot{\gamma}$ is observed with mixer speed (Figure 3.17). In this area the fluid is being advanced through the mixer, passing through the narrow space formed by the two opposing paddle sets. 9X45 also shows increasing $\dot{\gamma}$ with mixer speed, but values are lower near the center of the mixer and higher near the barrel wall when compared with 9X simulations. This is likely due to additional flow types caused by staggered paddles in the center of the mixer.

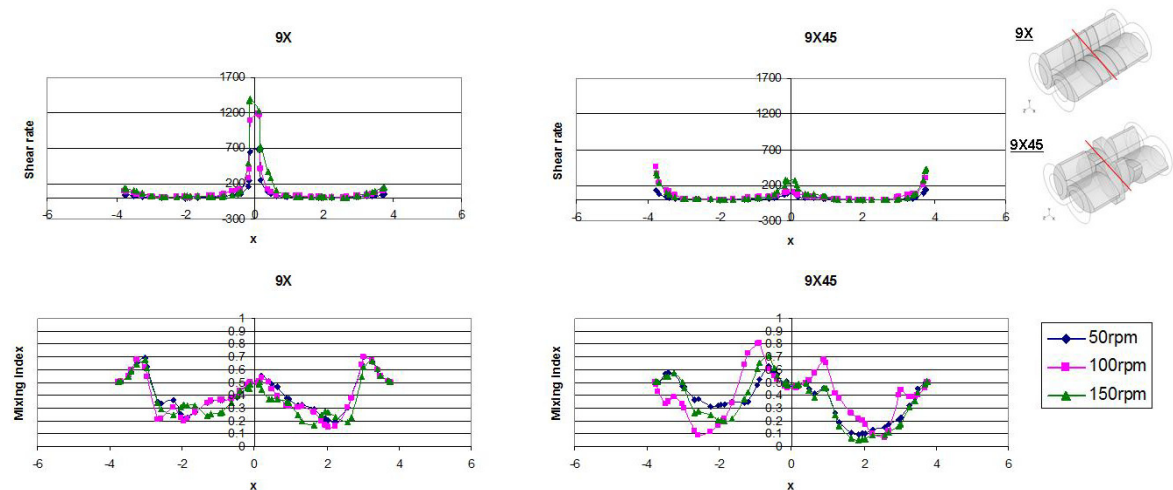


Figure 3.17. Power-law fluid shear rate and mixing index along Line 3 at different mixer speeds and paddle stagger angles a) 9X $\dot{\gamma}$, b) 9X45 $\dot{\gamma}$, c) 9X λ_{MZ} , d) 9X45 λ_{MZ} .

There is no significant mixing index trend with increasing mixer speed. In 9X45, there are λ_{MZ} values closer to zero and one, indicating both more rotational and elongational contributions than that found in 9X. 100rpm, in particular, shows a strong elongational contribution.

3.5.4 Effect of flow rate on mixing in a Bird-Carreau fluid

Little effect on v_x values is evident when increasing fluid inflow rate in 9X (Figure 3.18), although peak v_x values are greater than those seen with the power-law fluid. Increasing v_x is only seen on the left side of the mixer in 9X45, which has higher overall v_x magnitude than 9X. The right side of the mixer has lower magnitude values in 9X45 and the curves have shallower peaks throughout the mixer. This is likely due to enhanced fluid movement caused by the greater fluid inflow rate and staggered paddles, leading to more horizontal fluid movement. The paddle position on the right side of the mixer has a negative effect on horizontal flow at this point in the rotation.

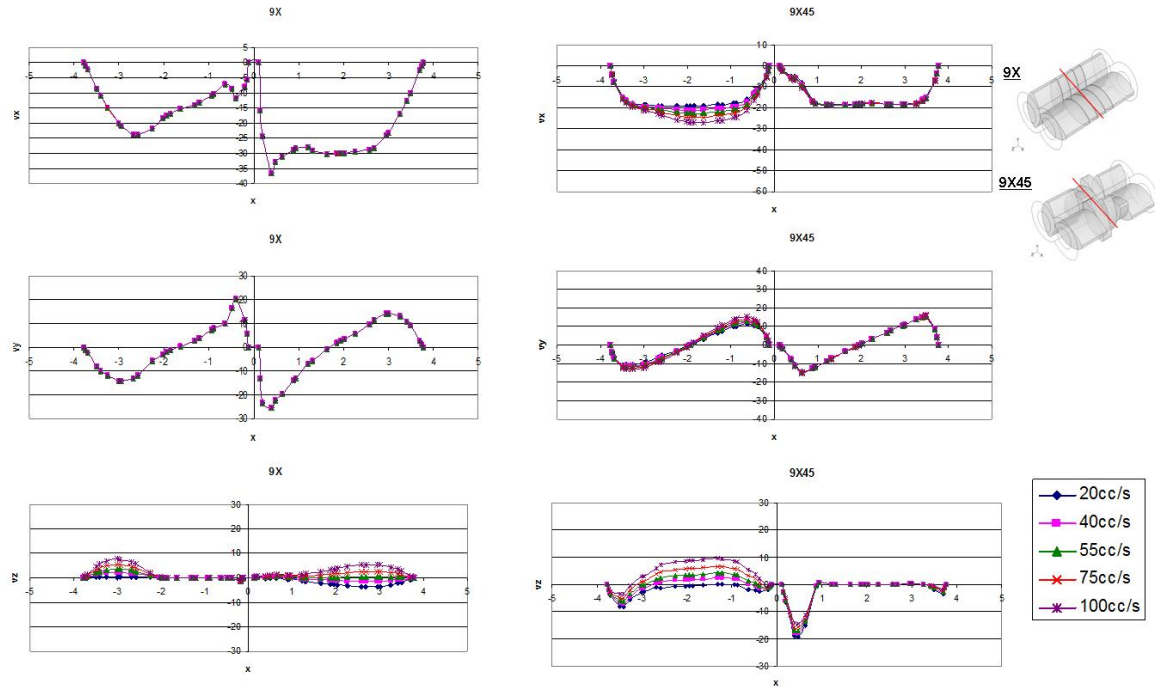


Figure 3.18. Bird-Carreau fluid velocity components along Line 3 at different fluid inflow rates and paddle stagger angles a) 9X v_x , b) 9X45 v_x , c) 9X v_y , d) 9X45 v_y , e) 9X v_z , f) 9X45 v_z .

No significant difference in v_y values is seen with increasing fluid inflow rate in 9X. In contrast, we see increasing v_y magnitude on the left side of the mixer in 9X45. Higher fluid speed combines with the paddle rotation to bring the fluid in the positive vertical direction. Lower magnitude peaks are found near the mixer center and higher magnitude near the barrel wall compared to 9X. Thus the staggered configuration appears to have a greater influence on vertical fluid movement near the barrel wall.

In 9X, increasing fluid inflow rate increases v_z . At low flow rates there are areas of backflow which disappear as the flow rate increases. On the right side of the mixer the paddle position blocks flowthrough at lower flow rates. 9X45 displays significant backflow near the center of the mixer with minimal v_z values on the right side of the mixer near the barrel wall. Increasing fluid inflow rate does not eliminate this backflow.

Maximum v_z is greater in 9X45 and increases with flow rate. Backflow and flowthrough need to be balanced to allow sufficient fluid residence time within the mixer. The combined positive and negative effects on v_z are similar to those seen in the power law fluid results above, although the Bird-Carreau fluid displays a beneficial combination of greater backflow and less flowthrough.

In the center of the mixer, peak $\dot{\gamma}$ is observed and the value is virtually unchanged with increasing fluid inflow rate in 9X (Figure 3.19). 9X45 peaks are near the barrel wall, but also show little variation with increasing flow rate. These values are much lower than those found in 9X. This indicates significant shear flow in 9X which is disrupted by the change in paddle orientation in 9X45. Fluid is no longer mainly passing through the narrow space formed by the parallel paddles moving in opposite directions, but primarily experiencing other flow types. In comparison with the power law fluid, the Bird-Carreau fluid has a greater shear rate peaks, due to its shear-thinning behavior.

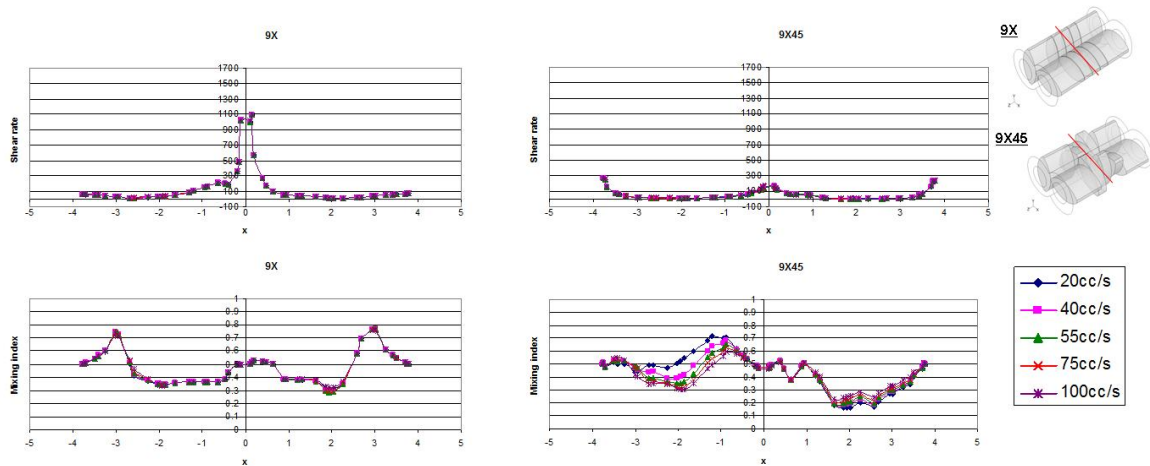


Figure 3.19. Bird-Carreau fluid shear rate and mixing index along Line 3 at different fluid inflow rates and paddle stagger angles a) 9X $\dot{\gamma}$, b) 9X45 $\dot{\gamma}$, c) 9X λ_{MZ} , d) 9X45 λ_{MZ} .

Peaks indicating good dispersive mixing ($\lambda_{MZ}=0.7$) are visible in 9X near the middle of the paddle on each side of the mixer. These peaks are similar to those values seen with the power-law fluid. Areas indicating simple shear flow ($\lambda_{MZ}=0.5$) are found in both configurations near the mixer center. This corresponds with the high $\dot{\gamma}$ seen above. No areas of pure rotational flow ($\lambda_{MZ}=0$) are seen, 9X45 shows a more irregular trend than 9X ; and peak values are only on the left side of the mixer. Decreasing λ_{MZ} values are seen on the left side of the mixer with increasing flow rate, while increasing values are on the right side. This is an indicator of the additional disturbance caused by the staggered paddles.

3.5.5 Effect of mixer speed on mixing in a Bird-Carreau fluid

Increasing mixer speed increases v_x magnitude in 9X (Figure 3.20) due to the additional energy imparted to the fluid. Lowest magnitudes are near the mixer center and wall as fluid in these areas is more likely to experience vertical motion. In 9X45, a broader region of large magnitude v_x values is seen compared to 9X. Peak values are significantly less than those in 9X but also increase with mixer speed.

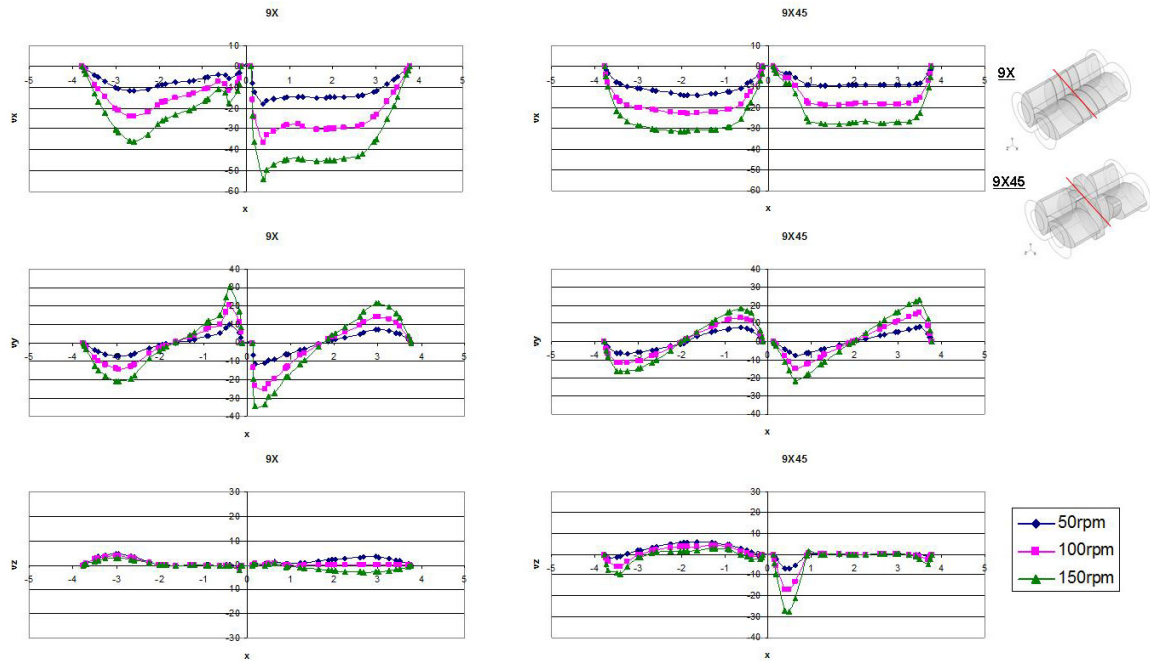


Figure 3.20. Bird-Carreau fluid velocity components along Line 3 at different mixer speeds and paddle stagger angles a) 9X v_x , b) 9X45 v_x , c) 9X v_y , d) 9X45 v_y , e) 9X v_z , f) 9X45 v_z .

In 9X v_y magnitude increases with mixer speed. Greatest magnitude values are seen near the mixer center, following the counter-clockwise paddle motion. Moderate values occur near the center of the paddle. Increasing mixer speed also increases v_y magnitude in 9X45. A similar trend to 9X is observed, although peak values are lower.

Decreasing v_z magnitude is seen with increasing mixer speed in 9X. Backflow is found on the right side of the mixer at the highest mixer speed. This is noteworthy due to the expectation that higher speeds will propel the fluid more quickly through the mixer. There is also a smaller backflow area in the mixer center. In 9X45 there is more significant backflow than 9X, as well as an additional area near the barrel wall. This positive impact is due to the increased fluid reorientation caused by the staggered paddles.

Shear rate increases significantly with mixer speed in the center of 9X (Figure 3.21). Shear is not the only flow in the mixer. A lower $\dot{\gamma}$ is an indication of the significance of these other flow types. In addition to small $\dot{\gamma}$ peaks in the mixer center, larger peaks are seen near the barrel wall. All peak values increase with mixer speed. This is due to the added energy imparted to the fluid as it moves between the perpendicular paddles rotating at an increasing rate.

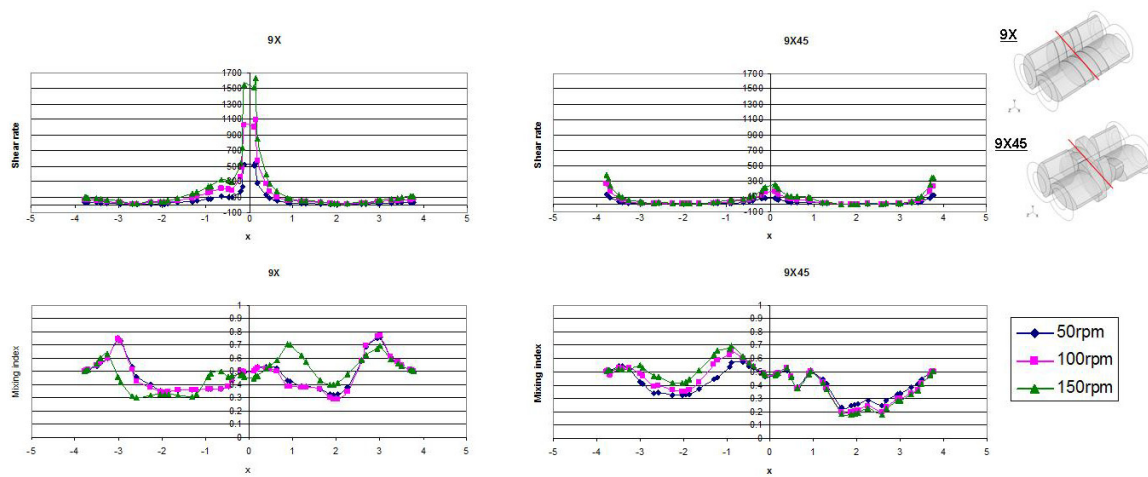


Figure 3.21. Bird-Carreau fluid shear rate and mixing index along Line 3 at different mixer speeds and paddle stagger angles a) 9X $\dot{\gamma}$, b) 9X45 $\dot{\gamma}$, c) 9X λ_{MZ} , d) 9X45 λ_{MZ} .

There is little difference between the λ_{MZ} values in 9X at 50rpm and 100rpm. Both show good dispersive mixing ($\lambda_{MZ}=0.7$) near the barrel wall. At 150rpm the λ_{MZ} values are similar in the center of the mixer, but lower peaks are found near the barrel wall. An additional peak is offset from the mixer center. Increasing the mixer speed to this level increases rotational contribution near the barrel wall and also increases the elongational contribution in the mixer center. This difference in behavior is likely caused by the interaction between the two paddle sets in the center of the mixer, imparting opposing motion to the fluid.

λ_{MZ} values indicating good dispersive mixing ($\lambda_{MZ}=0.7$) are seen near the mixer center in 9X45. Areas of simple shear ($\lambda_{MZ}=0.5$) are found near the barrel wall. Increasing mixer speed increases λ_{MZ} on the left side of the mixer, while decreasing λ_{MZ} on the right side. This indicates greater elongational flow and rotational flow, respectively.

3.6 Conclusions

Increasing power-law fluid inflow rate increases v_z as expected due to fluid inflow in the positive z direction. Simple shear flow is seen at peak $\dot{\gamma}$ in the center of the mixer, and efficient dispersive mixing appears near the barrel wall at all flow rates. At the highest fluid inflow rate this is also observed near the barrel center. Combined with high $\dot{\gamma}$, these areas are suited for bubble break-up. Both 9X and 9X45 configurations experience an increase in velocity and $\dot{\gamma}$ with mixer speed. Only the 9X45 geometry experiences areas of backflow improving fluid retention time in the mixer. Despite this, staggering the paddles results in generally lower magnitude velocity and $\dot{\gamma}$. This seems to contradict the expectation that staggered paddles enhance opportunities for mixing.

Maximum v_z values are greater in 9X45 than 9X, for the Bird-Carreau fluid, and increase with fluid inflow rate. Positive velocity contributions include an area of backflow visible near the mixer center and increasing v_x and v_y magnitude with fluid inflow rate in 9X45. The $\dot{\gamma}$ peak in 9X is greater than that in 9X45, but both display areas of good dispersive mixing and simple shear flow. In 9X45, the mixing index trend is irregular with increasing fluid inflow rate corresponding with the mixed velocity effects. Backflow magnitude is greater in 9X and this, combined with increased v_x and v_y , promotes fluid mixing. Shear rate peaks increase with mixer speed in both configurations; and 9X peaks are the greater of the two. More disruption at higher mixing

speeds is indicated by the additional λ_{MZ} peak in 9X, and in 9X45 as a combination of increasing λ_{MZ} values on the left side of the mixer and decreasing λ_{MZ} values on the right side of the mixer.

Under the same operating conditions, the Bird-Carreau fluid shows greater influence of paddle motion. This is possibly due to the inelastic nature of the fluid. The Bird-Carreau fluid shows significantly less flowthrough than the power-law fluid as well as significant backflow. This is beneficial to mixing, allowing the fluid more time for reorientation in the mixer. Maximum $\dot{\gamma}$ for the Bird-Carreau fluid is higher than that seen for the power-law fluid. This is likely due to the shear-thinning nature of the fluid, allowing increased shearing as the fluid viscosity decreases. Maximum values of λ_{MZ} are similar for both fluids, but the Bird-Carreau fluid shows no areas of pure rotational flow, indicated by a minimum λ_{MZ} of 0.15. As this fluid is strongly influenced by shear flow, it is possible that this domination prohibits areas of pure rotational flow.

The mesh used in this work was developed to ensure a dense mesh in areas with a high velocity gradient, to avoid barrel elements overlapped by both paddles, and to save computational cost without a negative effect on accuracy. Simulation data obtained using the chosen mesh showed good correlation with Newtonian experimental data. Extending the investigation to non-Newtonian fluids enabled the modeling of increasingly complex fluids in an industrial mixer. Further research will advance this work into the area of viscoelastic materials.

Chapter 4

EXTENSION RATE DISTRIBUTION AND IMPACT ON BUBBLE SIZE DISTRIBUTION IN NEWTONIAN AND NON-NEWTONIAN FLUID IN A TWIN SCREW CO-ROTATING MIXER¹

4.1 Abstract

Extension rate is known to weigh considerably more than shear rate in the dispersion of bubbles in a mixer. If both shear rate and extension rate are known then it is possible to calculate the maximum stable diameter of bubbles in a flow field based on estimation of the Capillary number Ca . Extension rate distributions have been calculated in a twin screw mixer for Newtonian and non-Newtonian fluids. While shear rate distribution calculations are routinely made, extension rate calculations have never been made before in a complex geometry since the classical work of Debbaut and Crochet (1988) showed that extension rate was given by the ratio of the third invariant of the strain rate tensor to the second invariant of the strain rate tensor. In an overwhelming number of studies extension rate is assumed to be negligible. This study shows that the extension rate is quite significant and equal to 15-25% of the magnitude of the shear rate depending on location in the mixer and mixer speed. The center of the mixer where the two sets of paddle elements intermesh displays high extension and shear rates. Critical capillary number and maximum stable bubble diameter are affected much more by extension rather than shear flow. Different flow types dependent on location in the mixer produce varying impacts on bubble breakup. Mapping maximum stable bubble diameter defines areas which have a higher potential for bubble dispersion.

¹ Submitted to the Journal of Food Engineering in January 2015.

4.2 Introduction

Extensional flows during mixing are very important in the deformation and breakup of droplets/bubbles which in turn are very important to foaming processes in the chemical and food industries. (Vyakaranam and Kokini, 2012; Cisneros and Kokini, 2002; Huang and Kokini, 1999). While shear rate distribution calculations are routinely made extension rate calculations have never been made before in a complex geometry since the classical work of Debbaut and Crochet (1988) showing that extension rate is equal to the ratio of the third invariant of the strain rate tensor to the second invariant of the strain rate tensor. Despite their importance in the transportation and quality of two phase dispersed systems, direct extension rate distribution studies have not been conducted to date in any complex geometry. Fundamental studies of extension rate generally used simplified geometries such as abrupt contractions (Debbaut and Crochet, 1988; Keunings and Crochet, 1984; Debbaut, et al., 1988) or expansions (Dheur and Crochet, 1987), flow around a sphere, and circular die swell (Debbaut and Crochet, 1987). Extension rate is important in complex flows but it comes in tandem with shear rate and most flows are combined shear and extension. In their rigorous theoretical studies Debbaut and Crochet (1988) examined extensional flows for generalized Newtonian (White-Metzner and Bird-Carreau) and viscoelastic fluids (upper-convected Maxwell). They showed that extension rate can be calculated from the ratio of six times the third invariant to the second invariant of the rate of strain tensor.

Janssen and Meijer (1993) noted that fluids in practical mixing devices experience bubble break-up beginning with the elongation of threads rather than stepwise break-down of larger bubbles under equilibrium conditions. Consistent with our work they

showed that transient mechanisms resulted in smaller droplets and allowed a finer morphology at a higher viscosity ratio. They found that 2D elongation was more effective than simple shear flow. In fact, the critical capillary number Ca_{cr} was lower for the thread scenario than that for a drop. A greater stretching rate caused a thinner thread before break-up and thus smaller resulting drops.

In their experimental and numerical work on starch extrusion Emin and Schuchmann (2013) found that increasing screw speed and oil content of the blend increased bubble coalescence due to the effect on drainage probability and increased likelihood of collisions between bubbles. In contrast, increasing blend feed rate decreased coalescence. They found that increasing screw speed did not necessarily result in smaller bubbles, due to a combination of increased droplet break-up and coalescence. Increasing feed rate caused smaller droplets due to an increase in blend viscosity and decreased probability of coalescence. They also found that reverse kneading blocks increased the number of particles with a high maximum capillary ratio (Ca/Ca_{cr}), promoting dispersive mixing.

Previous work in our research group (Vyakaranam and Kokini, 2012) has examined bubble breakup as a function of flow type (shear vs. extensional) using a Newtonian fluid in a Readco continuous mixer utilizing the magnitude of the Manas-Zloczower mixing index given by:

$$\lambda_{MZ} = \frac{|\mathbf{D}|}{|\mathbf{D}| + |\mathbf{\Omega}|} \quad \text{Equation 4.1}$$

where \mathbf{D} is the strain rate tensor and $\mathbf{\Omega}$ is the vorticity tensor.

The Manas-Zloczower mixing index ranges from 0 for pure rotation to 1 for pure elongation and 0.5 for pure shear flow.

Consistent with the earlier fundamental studies of Grace (1982) and Khakhar and Ottino (1986), it was shown that extensional flows are key in the breaking of air cells during mixing. Three different paddle configurations for the mixing portion of the screw were used: FLAT, 45F (45° forward), and 45R (45° reverse). In the 45F and 45R configurations, the three center paddle pairs were staggered at 45° to each other, forward and reverse, respectively.

Better dispersive mixing was seen when elongational flows, as predicted by the Manas-Zloczower mixing index were strong. Elongational flow was determined by values of the index above 0.7, approaching 1, and was particularly observed in the intermeshing region above and below the paddle, as well as the middle of the C-shaped section between the barrel and the paddle. The behavior in the intermeshing region is of particular interest, as it is critical for dispersive mixing. Elongational flow was not observed in the nip region between the paddle tip and the barrel surface, where the highest shear rate is seen.

Staggered paddles were shown to disrupt the axial flow and reduced elongational flow. Only the FLAT configuration allowed apparent squeeze flow in the intermeshing region as the fluid passed between two paddles inducing motion in opposite directions. This effect was fragmented with the introduction of staggered paddles.

The objective of this paper is to gain further in-depth understanding of the bubble dispersion process and predict critical bubble diameter by calculating the extension rate profile for Newtonian and non-Newtonian fluids and mapping the extension rate and

shear rate distribution in different parts of the geometry. A twin screw continuous mixer is an important model continuous mixer especially in the plastic and dough industries for automated operations. Quantitatively predicting the contribution of extensional flows is valuable in understanding the overall flow particularly in a complex geometry where both shear and extension coexist, contributing to overall deformation rate and bubble dispersion.

4.3 Materials and Methods

4.3.1 Description of the numerical simulation

A 360° isothermal simulation was run on the full nine-paddle mixing section geometry (Figure 4.1) with the mesh used previously by Rathod et al. (2014) and by Vyakaranam et al. (2012). A closer view of the xy mesh is shown in Figure 4.2.

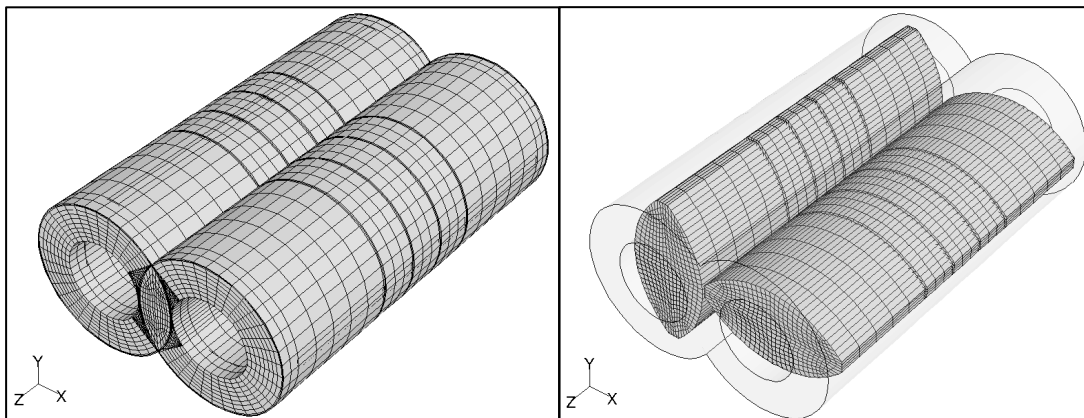


Figure 4.1. Nine paddle length barrel and paddle meshes (Rathod et al., 2014).

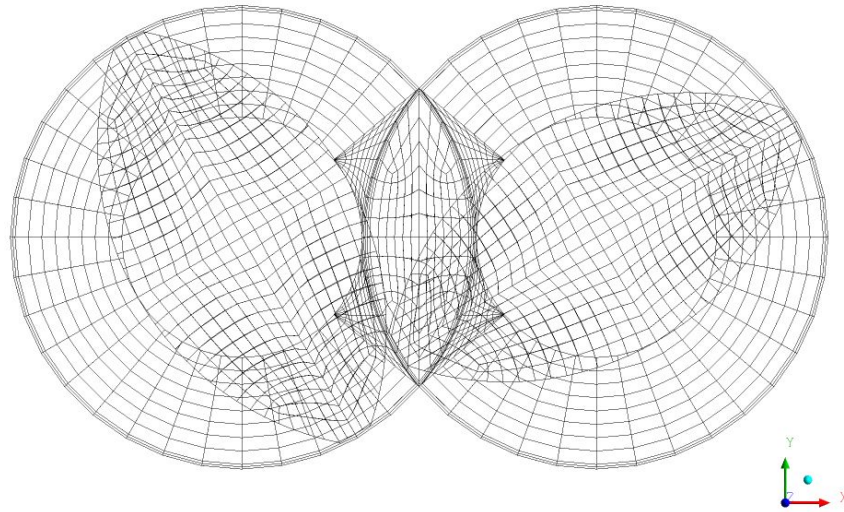


Figure 4.2. XY plane of superimposed barrel and paddle meshes.

In order to enable simulation of the fluid dynamics in moving elements mesh superposition was used (Vyakaranam, et al., 2012; Rathod and Kokini, 2013). The mixer speed was initially set at 100rpm and the fluid inflow rate was set at 55.31cc/s. A 2% Carboxymethyl cellulose solution was used as a model power law fluid where $K=15.74 \text{ N s}^n \text{ m}^2$, $n=0.397$, $\lambda=1$ and the density is 1.0068 g/cm^3 .

Mixer speeds of 50rpm, 100rpm, and 150rpm and fluid inflow rates of 20cc/s, 55.31cc/s, and 100cc/s were used. In addition to the non-Newtonian fluid two Newtonian fluids with viscosities of 1200 Poise and 600 Poise were modeled.

Simulations were run on a Dell Precision 690 workstation with Dual core Xeon processors and 16GB RAM using the Polyflow suite of programs from ANSYS, Inc. $\dot{\epsilon}$ (extension rate – Equation 4.2) was calculated and studied for all x and y values in a plane.

4.3.2 Simulation of extension rate

Extension rate ($\dot{\epsilon}$) was calculated from the deformation tensor (**D**) (Debbaut and Crochet, 1988), after calculation of the second invariant (*II*) and the third invariant *III* of the rate of deformation tensor, using Equation 4.2 below:

$$\dot{\epsilon} = 6 \frac{III}{II} \quad \text{Equation 4.2}$$

$$II = tr(\mathbf{D}^2) \quad \text{Equation 4.3}$$

$$III = \det(\mathbf{D}) \quad \text{Equation 4.4}$$

Twelve planes were sliced at $z=1.92$ (Plane 1), $z=4.475$ (Plane 2), $z=5.82$ (Plane 3), $z=7.165$ (Plane 4), $z=8.51$ (Plane 5), $x=0$ (Plane 6), $x=0.5$ (Plane 7), $x=-0.5$ (Plane 8), $x=2$ (Plane 9), $x=-2$ (Plane 10), $x=4$ (Plane 11), and $x=-4$ (Plane 12) (Figure 4.3). The positive y values refer to the upper half of the mixer while the positive x values refer to the right-hand half of the mixer. As the values of z increase, fluid is approaching the front of the mixer.

ANSYS

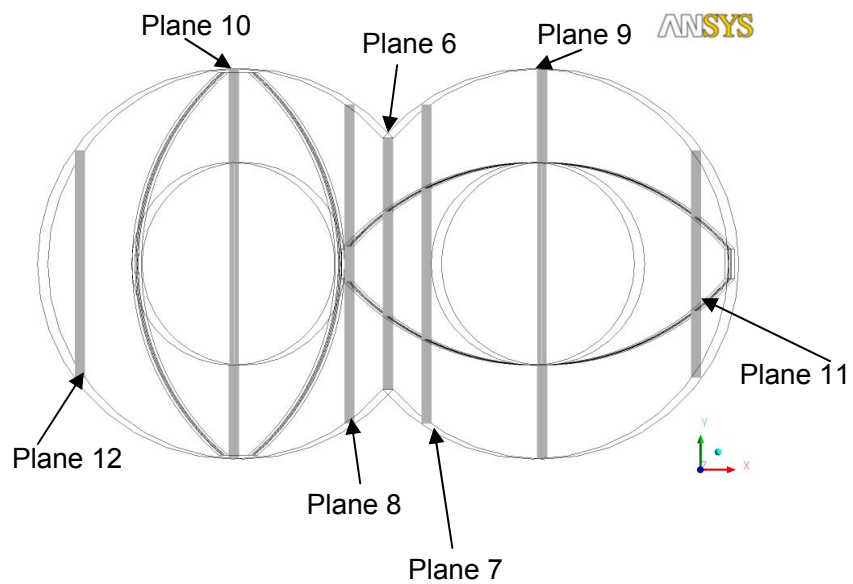
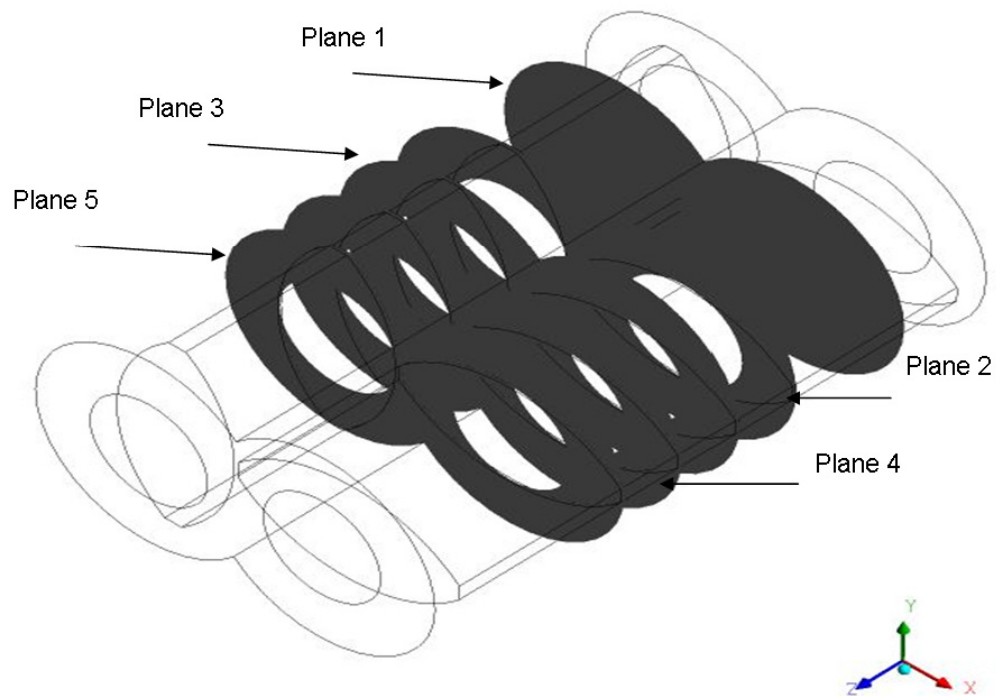


Figure 4.3. Location of Planes used to examine extension rates in the mixer a) Planes 1-5, b) Planes 6-12.

Planes 2, 3, 4, and 5 are locations in the center portion of the mixer, in the gap between the individual paddles. This allows us to examine the maximum number of fluid

points as data collection is not constrained by the location of the paddle. It also affords a view of activity in a very narrow area bounded by moving parts. Planes 6-12 were chosen to view changes along the axial length of the mixer. Extension rate values were also compared with shear rate ($\dot{\gamma}$) values along all of the planes.

4.3.3 Calculation of critical capillary number and maximum stable bubble diameter

A flow strength criterion (α_f) is defined using Equation 4.5 to account for the combination of shear and extensional flows. In two-phase flows, which have been of interest to this laboratory (Vyakaranam and Kokini, 2012), extensional flows play a very important role in dispersion of bubbles and the creation of nuclei for bubble growth in processes like extrusion and baking.

$$\alpha_f = \frac{\dot{\epsilon}}{\sqrt{\dot{\epsilon}^2 + \dot{\gamma}^2}} \quad \text{Equation 4.5}$$

Critical capillary number (Ca_{cr}) is the capillary number above which bubbles become unstable and break (Vyakaranam and Kokini, 2012). Much higher magnitude shear flow strength is needed to break bubbles in comparison to elongational flow. In order to incorporate both shear and extension rate the alternate elongational flow strength parameter α_f , defined in Equation 4.5, is used in place of α .

$$Ca_{cr} = \frac{0.145 p^{\frac{1}{6}}}{\alpha^{\frac{1}{2}}} \quad \text{Equation 4.6}$$

where p is the ratio of air viscosity to non-Newtonian fluid viscosity obtained from the simulation at relevant shear rates. Maximum stable bubble diameter is obtained from Ca_{cr} , fluid characteristics, and flow strength.

$$d_{\max} = \frac{2Ca_{cr}\sigma}{\mu_c\dot{\epsilon}} \quad \text{Equation 4.7}$$

where σ is surface tension and μ_c is the viscosity of the non-Newtonian fluid.

4.4 Results and Discussion

The magnitude and intensity of the numerically calculated extension rate in tandem with shear rate is studied and used to predict bubble size distribution from the ratio and intensity of shear and extension rates.

4.4.1 Analysis of extension rates in the twin screw mixer

4.4.1.1 Extension rate variation with viscosity and mixer operating parameters for a Newtonian fluid in a sample plane

Computations focused on Plane 4 as an example enable the study the effect of several material and operating parameters. Extension rate simulations were conducted with two Newtonian liquids, one with properties corresponding to corn syrup and the other with a viscosity half that of corn syrup. The variation of extension rate distribution was examined at one, two, and three revolutions on Plane 4 (Figure 4.4). Extension rate values and distribution were very similar for the three different revolutions. The magnitude of extension rates was nearly identical when the viscosity doubled. Extension rate values reached maxima at the top and bottom tips of the left-hand paddle for all parameters varied (viscosity, mass flow rate, and rpm). Due to the fixed nature of the barrel and the motion imparted to the fluid by the paddle, it is forced and drawn through the narrow gap formed by the two surfaces. This leads to fluid streams narrowing and lengthening resulting in stretching. Increasing the mixer speed increased the average and maximum extension rates proportionally (Figure 4.5).

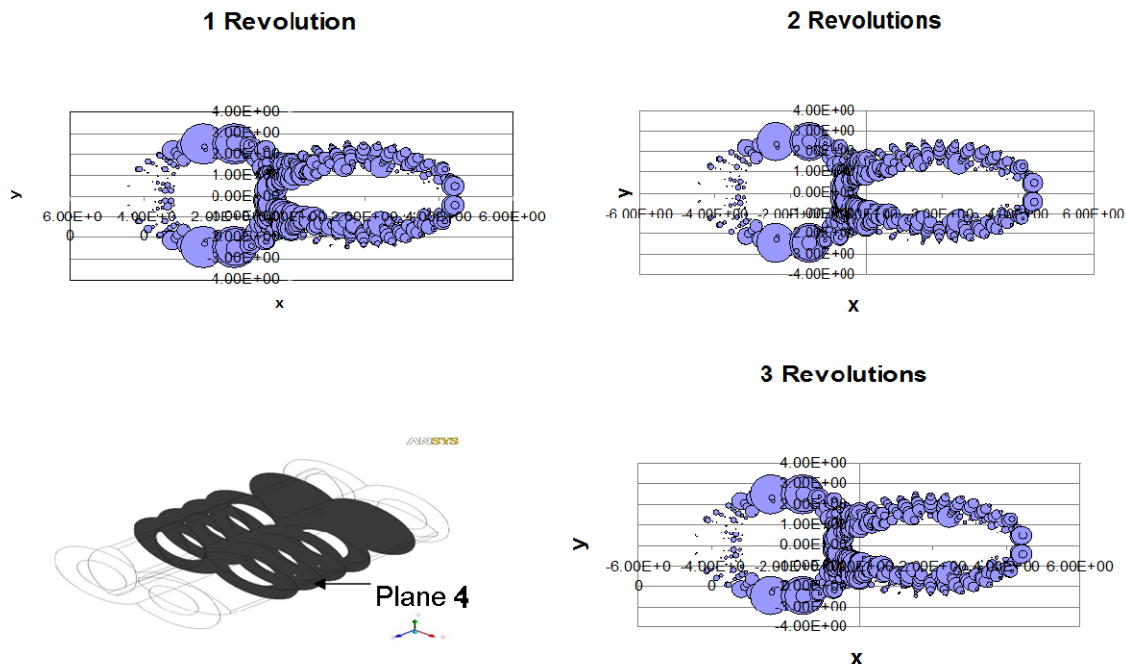


Figure 4.4. Extension rate for Newtonian corn syrup over three revolutions.

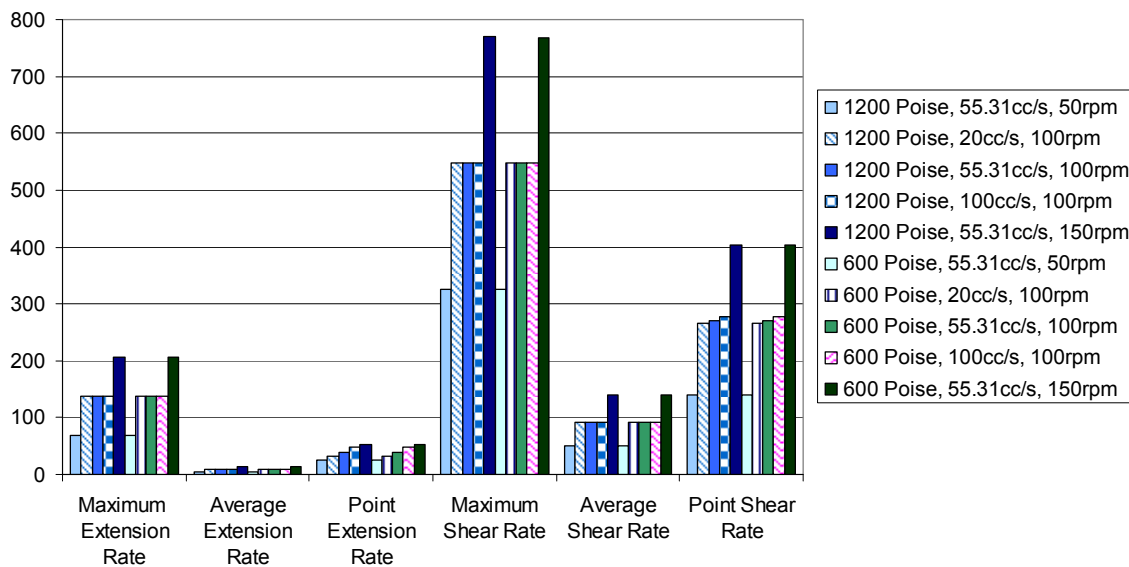


Figure 4.5. Extension and shear rate versus mixer speed and fluid inflow rate in Newtonian fluids over one revolution at three mixer speeds.

In order to provide physical insights into the variation of extension rates in the geometry of the mixer, one fixed point was also chosen in an area near the horizontal and

axial center of the mixer, where the fluid is overlapped by both paddles for periods of time within their rotation.

Varying fluid inflow rate had little impact on maximum and average extension rates (Figure 4.5) at a given mixer speed but increased the extension rate at the selected point. These results also correspond with previous findings which showed that although increasing fluid inflow rate increased fluid speed through the mixer; it did not significantly impact extensional flows (Rathod and Kokini, 2013). All extension and shear rate values (local, average, maximum) for both 600 and 1200 Poise were virtually identical.

In comparing extension rate and shear rate, the ratio of their maximum values is used (Figure 4.6). At a given mixer speed a constant ratio is seen regardless of fluid viscosity or inflow rate. In contrast, increasing mixer speed increases the ratio, indicating a greater contribution to maximum extension rate than maximum shear rate.

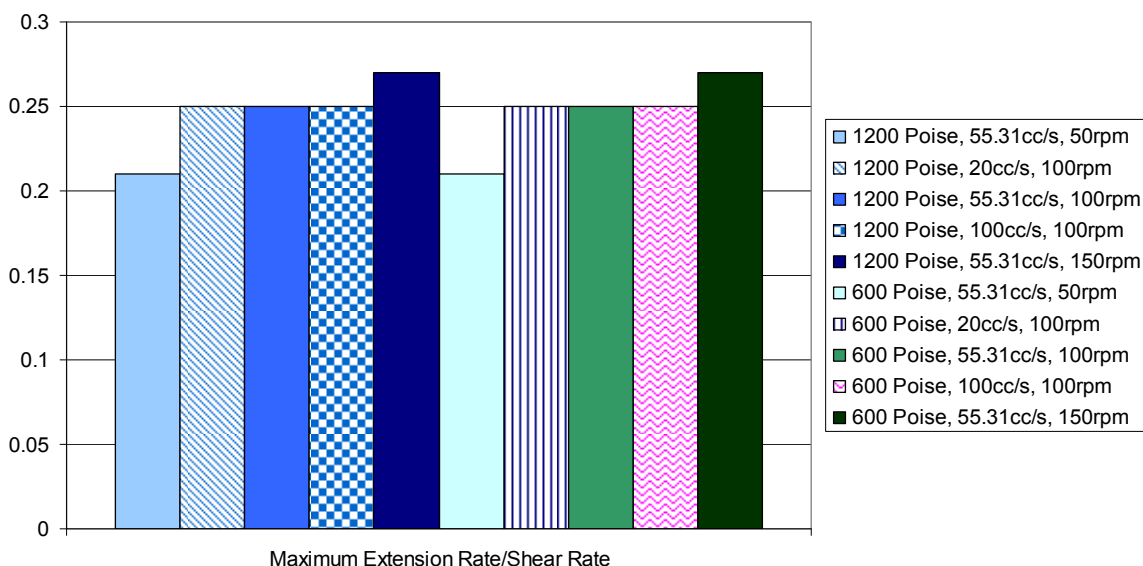


Figure 4.6. Ratio of maximum extension ratio to maximum shear rate for Newtonian fluids.

4.4.1.2 Extension rate variation with mixer operating parameters for a non-Newtonian fluid in a sample plane

Extension rate values were also examined over three revolutions for the non-Newtonian fluid model, a 2% CMC solution. Comparison at the same mixer speeds and fluid inflow rates used for the Newtonian fluids are shown for Plane 4. Similar to the Newtonian fluid simulation results, there is little difference in the magnitude of extension rates from one to three revolutions (Figure 4.7) showing that steady state has been obtained after one revolution. Peak values were seen at the tips of the left-hand paddle where the paddle pushing fluid along the barrel wall produces a high extension rate. Other significant observations are near the center of the mixer, between the tip of the right-hand paddle and the body of left-hand paddle where the paddle conveys the fluid through a narrow space and increased reorientation leading to relatively large extension rate is experienced.

As in the case of the Newtonian fluids changes seen from two to three revolutions are negligible and values (maximum extension rate, average extension rate, extension rate at the selected point) are not significantly affected beyond one revolution. This was true for all mixer speeds (Figure 4.8), indicating that one revolution has captured pertinent data. Additionally, extension rate at the selected point experienced a minimal increase at 20cc/s and a decrease at 100cc/s with increasing revolutions. Although the changes are small, it is interesting to note that at this point increasing fluid inflow rate, which speeds fluid in the z direction, had a negative impact on extension rate. There is a greater change in the magnitude of extension rates than that seen with previous Newtonian values, as well as minor variation with increasing rotations. This is an indicator of the more complex fluid model used.

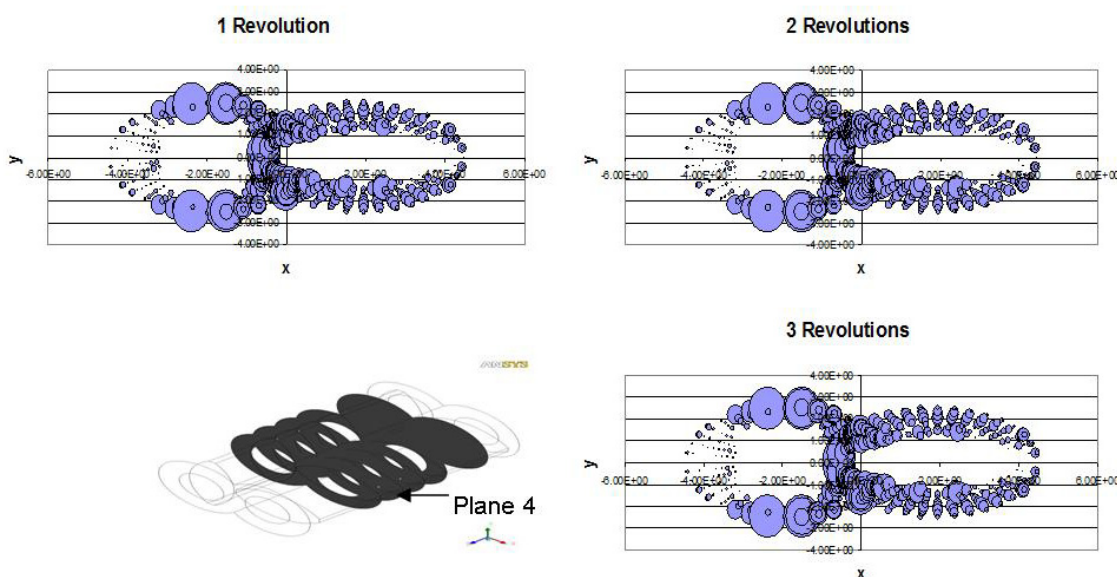


Figure 4.7. Extension rate for a non-Newtonian 2% CMC solution over three revolutions.

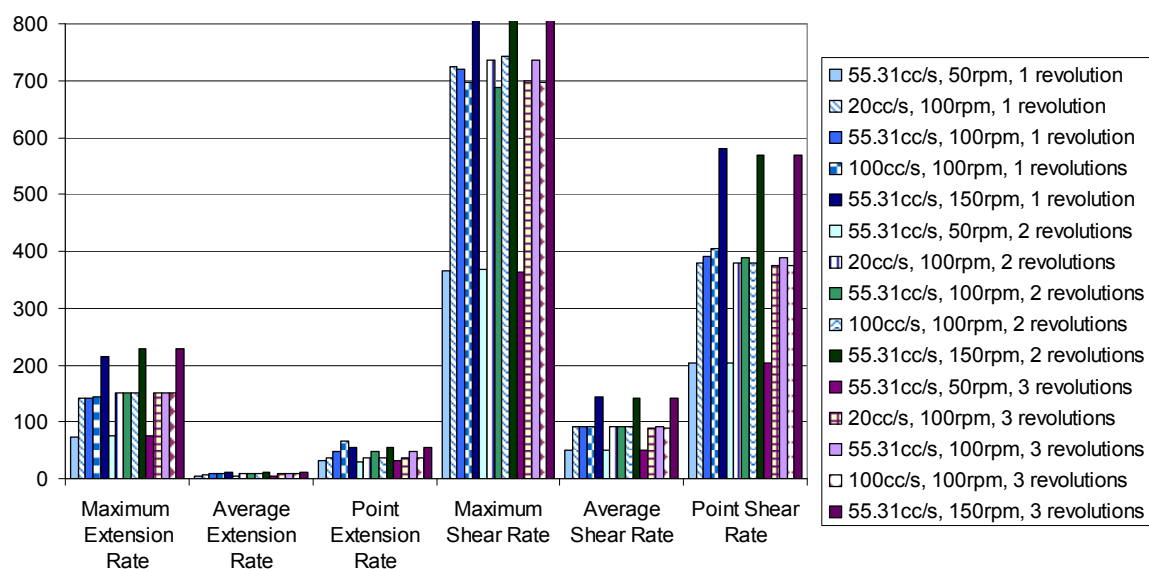


Figure 4.8. Extension rate and shear rate versus mixer speed and fluid inflow rate over three revolutions in a 2% CMC solution.

Maximum shear rate and shear rate at the selected point were greater than that found for the Newtonian fluid under the same operating conditions while average shear rate did not change appreciably. Thus fluid rheology is causing increased shear rate only in those areas which produce high shear rates due to their geometry. Increasing mixer

speed increased maximum shear rate in a similar way to maximum extension rate. In contrast, increasing fluid inflow rate had little impact on average shear rate.

The ratio of maximum extension rate to maximum shear rate under varying conditions is shown in Figure 4.9 and is little affected by increasing fluid inflow rate or mixer speed.

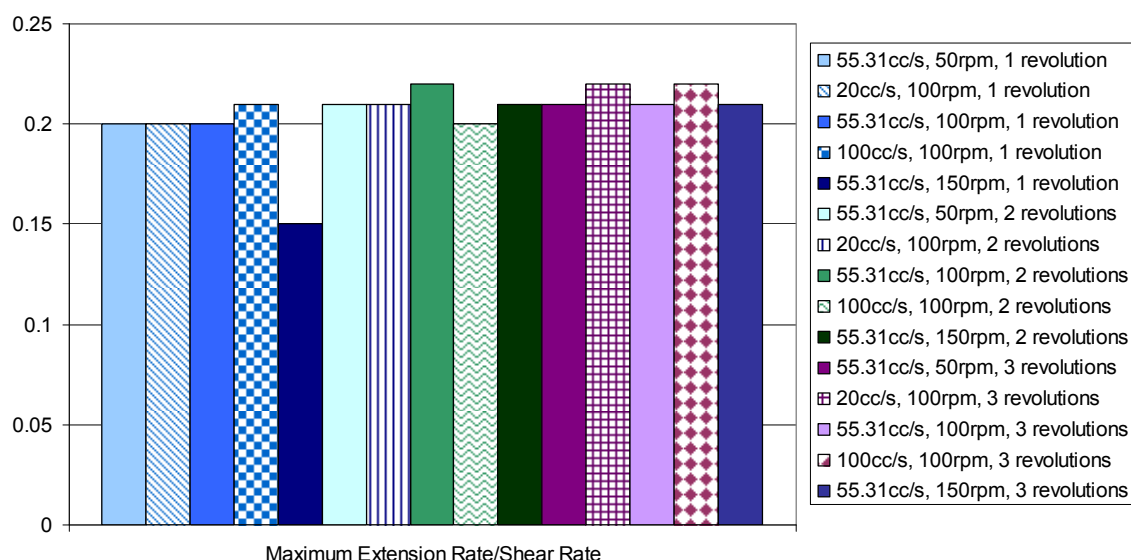


Figure 4.9. Ratio of maximum extension rate to shear rate over three revolutions for a 2% CMC solution.

4.4.1.3 Analysis of the distribution of the magnitude of extension rate in the axial direction in the mixer

In this part of the analysis only one revolution is used based on the earlier determination that this provided sufficiently detailed information without unduly increasing computational cost. Extension rate was plotted over the entire xy plane at different z values and across the entire yz planes at different x intervals.

With increasing axial distance, the fluid experiences the motion history of an increasing number of paddle pairs. Extension rate progressively increases as fluid moves

through the mixer from entry to exit passing between each additional paddle set. As stretching increases past a threshold, the fluid stretches at an increased rate. Plane 5 deviates from the trend due to its placement near the fused paddles and resulting reduced fluid disruption. The high values seen in Table 4.1 are most closely grouped in the planes nearest to the center of the mixer (Planes 3 and 4). The remaining planes show a range greater than 3-4% seen for Planes 3 and 4.

Table 4.1. Comparison of highest extension rates for Planes 1, 2, 3, 4, and 5

	Plane 1	Plane 2	Plane 3	Plane 4	Plane 5
fourth	65.96/s	131.72/s	144.53/s	137.56/s	122.08/s
third	71.24/s	131.84/s	145.98/s	138.87/s	124.41/s
second	77.03/s	133.78/s	148.42/s	142.07/s	125.01/s
maximum	107.83/s	141.20/s	149.33/s	142.64/s	136.11/s

In Figure 4.10 the magnitude of extension rate is displayed for five *xy* planes. Planes 2-5 have very similar patterns. None of these four planes is immediately adjacent to either the entry or exit, each is buffered by at least the length of three fused paddles, and similar extension rate values are seen in this central mixing area. Extension rate is non-uniform and depends on the flow strength throughout the geometry; the planes have several areas with high extension rates (Vyakaranam and Kokini, 2012).

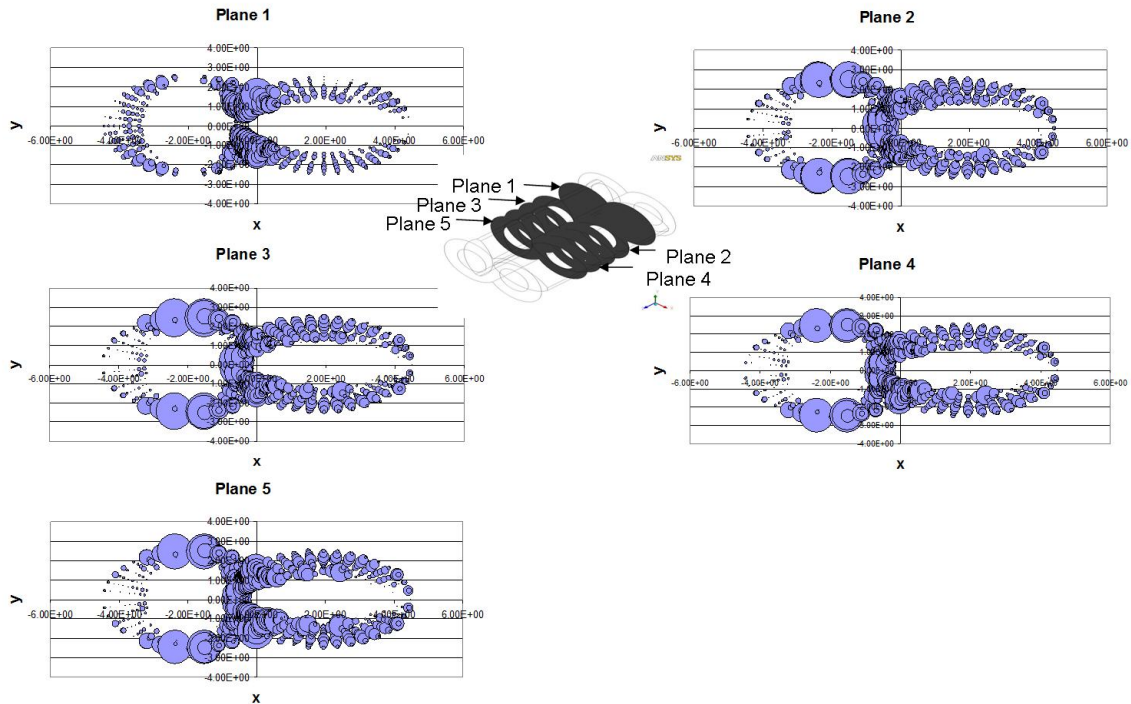


Figure 4.10. Evolution of extension rate across characteristic axial planes a) 1, b) 2, c) 3, d) 4, e) 5.

In Plane 2, the greatest values are seen on the left-hand side of the mixer (Figure 4.10b) and the pattern seen earlier in Plane 4 under various conditions is continued through the mixer. The two significant peaks correspond with the upper and lower paddle tips where pulling and stretching of the fluid is extensive. These peaks will be on the right side of the mixer when the positions of the paddles are reversed. At this point in the cycle the right paddle is horizontal and there are no extension rate peaks observed at its tip. Since this is a co-rotating mixer, there is no symmetry in extension rates on opposite sides of the mixer.

Peak extension rate values in the intermeshing zone appear to be caused by the overlapping motion of both paddles passing through the center of the mixer, an effect that is enhanced due to the 90° angle between the right and left-hand paddles moving the fluid in opposite directions. The fluid is stretched by the two paddle sets imparting partial

pulling motion coupled with opposing motion which results in mixed shear and extensional flow. In a co-rotating mixer the traditional assumption is that shear flow would predominate. However, we observe mixed shear and extensional flow with the magnitude of extensional flows averaging about 15-25% of the magnitude of shear flows. Prior to these calculations it was not possible to guess the contribution of extensional flows in this geometry. An additional peak extension rate is seen in the bottom half of the mixer. Greater and more frequent stretching is observed in the beginning portion of the mixer and stretching of the fluid is not limited to the bottom of the mixer.

Planes 3 and 5 have higher extension rates on the left-hand side of the mixer (Figure 4.10c and e). The only difference between the two sides is the position of the paddle set (i.e. vertical vs. horizontal); the left-hand paddle is vertical at this point in the cycle. This is consistent with earlier observations that fluid is being stretched mainly by upward motion of the paddle in the mixer especially in the narrow spaces between the barrel and the paddle. Interestingly, based on extension rate values fluid experiences the most reorientation and reorganization in locations which also have high shear. In the parts of the flow geometry closer to the entry of the mixer significant extension rates are not seen, but as the fluid moves forward toward the exit larger values are seen.

Extension rate peaks for Plane 1 (Figure 4.10a) are also found in the center of the intermeshing zone. The paddle outline is clearly visible as there is no significant stretching near the left paddle tips. Here relatively high shear occurs and there is a lack of synchronized motion to induce extension. There is also minimal stretching between the right paddle tip and barrel wall. In fact, the maximum extension rate in this plane is lower than that seen in Planes 2-5 (115 sec^{-1} vs. 140 sec^{-1}). Prior work has clearly shown that

this is the region where the highest shear rates are observed (Rathod and Kokini, 2013). The most significant extension rate values are slightly off-set to the left side of the mixer due to the vertical position of the left paddle. Minor peaks are seen away from the center, approaching the barrel wall. Unlike the other planes, no significant extensional flow is seen at the top and bottom of the mixer. Consistent with prior observations the highest values are seen in the areas of the barrel closest to the paddle centers. This seems to be due to the fused nature of the first three paddles.

4.4.1.4 Analysis of the distribution of the magnitude of extension rate in the horizontal direction of the mixer

The distribution in the horizontal direction was studied to complement understanding of the distribution of extension rates in a vertical plane at several constant horizontal locations. Seven vertical planes were selected as noted in Figure 4.3b. Maxima in Plane 6 at the center of the mixer are larger towards the exit of the mixer $z > 8$, while lower values are seen in the inlet side of the mixer, $z < 2$ (Figure 4.11a). This is interesting to note as Planes 1-5 did not show systematic increasing maximum extension rates with greater axial distance from the mixer inlet. Fluid is sheared and stretched more along the wall and with a decrease in the size of the flow channel. Increased extension rates occur at increasing axial distance from the mixer inlet only in the horizontal center of the mixer where shear and extensional flows are strongest.

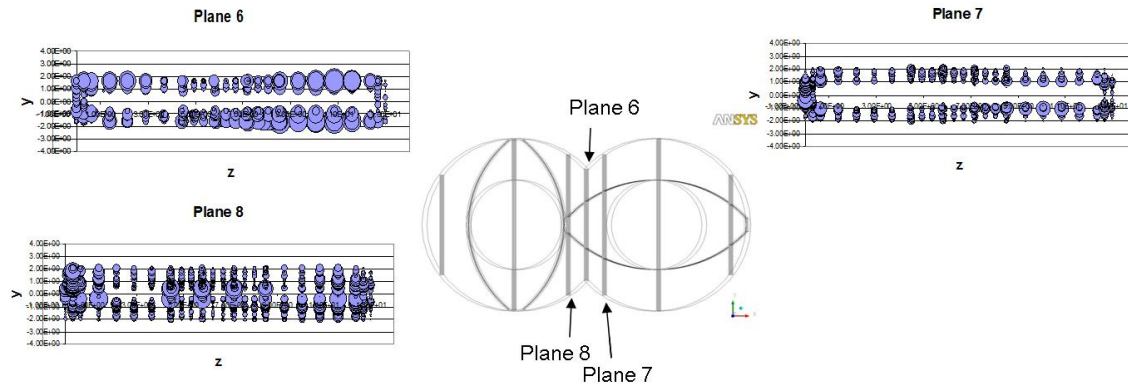


Figure 4.11. Evolution of extension rate across characteristic horizontal planes a) 6, b) 7, c) 8.

Plane 7 (Figure 4.11b) has relatively large extension rate values at the inlet of the mixer in the vertical center. Despite this, maximum values at the top and bottom of the mixer are greater in the latter third of the mixer. This builds on the fact that the narrow fluid channels between the paddles and wall are key for the development of stretching, particularly when changing from predominantly horizontal to vertical flow. The shear-thinning character facilitates elongational flow as the fluid moves through the narrow gaps in the mixer.

Plane 8 (Figure 4.11c) also displays larger extension rate values near the exit of the mixer, an example of the additive effect. There are additional large values seen in the vertical and axial center of the mixer, not seen in Plane 7. These large extension rate values are due to the fluid encountering both paddle sets in this area where narrow gaps drive extensional flows. Increasing distance from the horizontal center of the mixer results in decreasing extension rate.

4.4.2 Distribution of shear rates in the twin screw mixer

4.4.2.1 Analysis of the distribution of the magnitude of shear rate in the axial direction in the mixer

In order to improve understanding of flow behavior in the mixer, shear rate distribution is also analyzed as a complement to extension rate. Shear rate values were graphed on the same planes used for extension rate data displayed above. Largest shear rates (Figure 4.12) are seen in the center of the mixer and at the tip of the right-hand paddle closest to the wall. This observation is true for all five planes. The shear rate peak values at the right-hand paddle tip coincide with low extension rate values, and are an indicator of the variability in the types of flow dependent on location in the mixer.

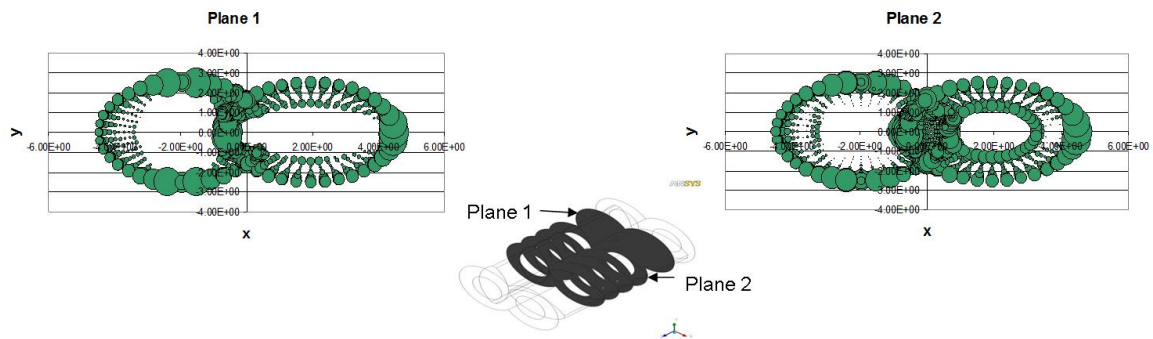


Figure 4.12. Evolution of shear rate across characteristic axial planes a) 1, b) 2.

Shear flows are the result of two perpendicular paddle sets in the center of the mixer moving in opposite directions. Shear combined with stretching was shown in earlier studies to contribute to more efficient mixing (Rathod, et al., 2014). Additional small shear rate values along the left-hand paddle, moderate values along the right-hand paddle, and large values in the center of the mixer are seen in Planes 2-5 due to fluid entering the gap between the paddles which causes considerable shear. Due to this similarity in shear rate trend, only Plane 2 is shown here. Decreasing maximum shear

rates and similar average shear rates are seen in Planes 2-5 with increasing axial distance from the mixer entrance. Plane 2 has the largest maximum shear rate and is in the transition between the fused paddles and those modeled with a gap. This location appears to have a significant impact on shearing due to the change in geometry of the fluid space.

4.4.2.2 Analysis of the distribution of the magnitude of shear rate in the horizontal direction in the mixer

As in the axial planes, largest shear rates in the horizontal planes are seen in the center of the mixer (Plane 6 – Figure 4.13a). Noticeable shear rates are seen near the entrance of the mixer due to the presence of the fused paddles, largest values in the axial center of the mixer, small shear rates in the gaps between the paddles, and small values in the areas of the fused paddles. This effect is decreased as the fluid moves toward the barrel wall and is no longer blocked by the paddles, evident in Plane 8 which shows shear rate values in the vertical center of the mixer (Figure 4.13c). Shear rate values near the inlet of the mixer are higher than those at the outlet in Planes 6 and 8. The converse is true in Plane 7, due to changes in the gap size for fluid to pass along the paddle. It is observed that the trend in shear rate magnitude is opposite to the trend in extension rate magnitude. Near the wall similar values are seen at all axial distances from the mixer inlet. This is likely due to the fact that the paddles are not crossing the plane at this point in the rotation.

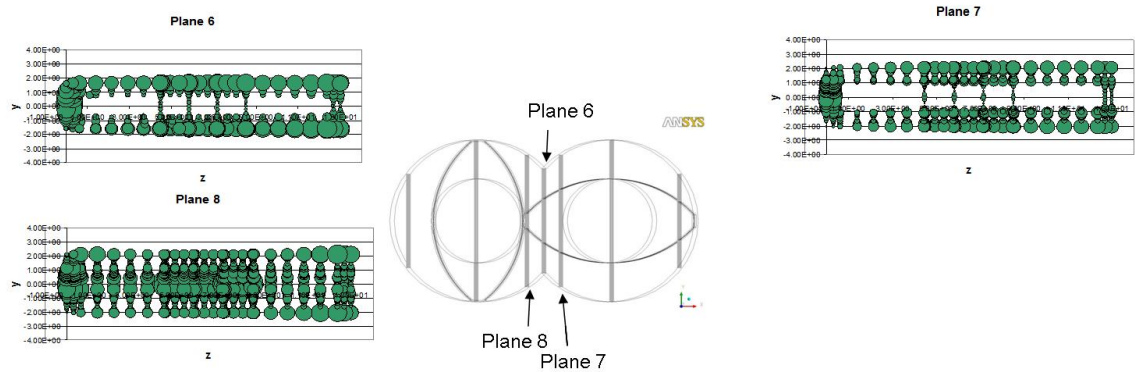


Figure 4.13. Evolution of shear rate across characteristic horizontal planes a) 6, b) 7, c) 8.

Average shear rates are higher in Planes 6 and 8 than in the remaining planes.

Plane 8 in particular displays large shear rates as it is in the gap between the right-hand paddle tip and the left-hand paddle. Due to its location, it is no surprise that this plane also has the highest extension rate among the yz planes.

4.4.3 Relative effect of extension rate and shear rate on critical capillary number and maximum stable bubble diameter in a non-Newtonian fluid

The importance of obtaining extension rate and shear rate distribution is in allowing calculation of the critical capillary number and the maximum stable bubble diameter across the mixer. These calculations have not been done before because extension rate distributions were unavailable prior to this study. Obtaining maximum stable bubble diameter also permits the calculation of an envelope of maximum possible bubble sizes in different locations in the mixer. Both critical capillary number and maximum stable bubble diameter are highest at extension rates close to zero (Figure 4.14) since the flow strength is too low to break and disperse bubbles. Little, if any, elongation force is imparted to the bubbles at this point and this cannot disperse the gas phase to

form small bubbles. As the extension rates increase, the external force on the bubbles increases. As a result, internal forces are overcome and the bubbles break into smaller, more stable bubbles. In a mixer, prior fundamental studies have suggested that bubbles will effectively disperse as a result of elongational flows during mixing.

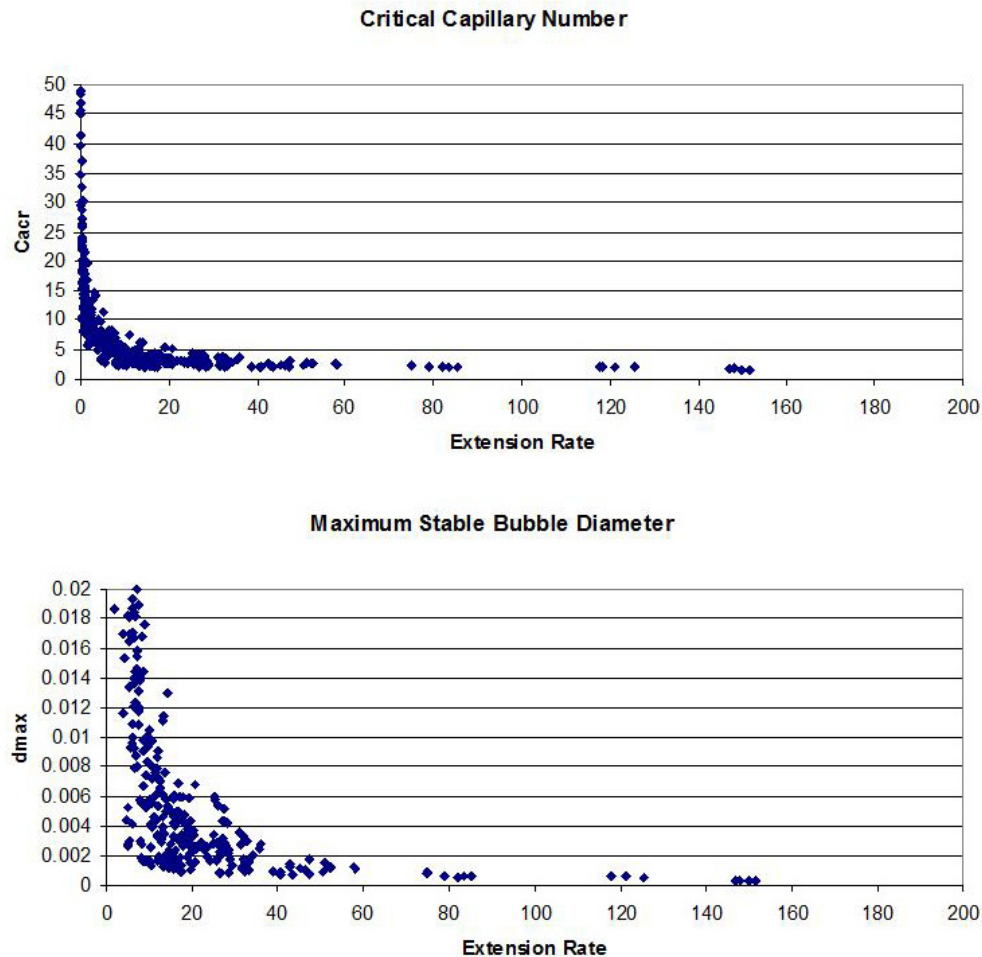


Figure 4.14. Relative effect of extension rate on a) critical capillary number and b) maximum stable bubble diameter.

The critical capillary number decreases with increasing flow strength and increasing elongational and shear flows. This leads to prediction of regions in the mixer which promote the breakdown and dispersion of bubbles. Any bubble that will travel

through regions of high flow strength clearly needs to break into much smaller bubbles.

As the largest bubbles break, remaining bubbles have a smaller d_{max} . The relation between higher extension rates and lower maximum stable bubble diameters is compatible with the understanding that increasing elongational flow is more efficient in breaking bubbles. As seen in the xy and yz plots above, areas in the mixer center and between the paddle tip and barrel wall provide areas of higher extension rate values which increase external stress on bubbles, leading to lower d_{max} .

In Figure 4.15 it is evident that bubbles in the same xy location show a smaller d_{max} with increasing axial distance. Large bubbles are seen in the horizontal center of the mixer near the entrance where extensional flow strength is lower. When the fluid is approaching the latter third of the mixer, d_{max} is at a minimum value. By far the largest d_{max} is found in the region between the vertical left paddle and the wall effectively parallel to it. This corresponds with comparatively low extension rates found in this area. It is interesting to note that the points with the highest and lowest d_{max} occur in areas experiencing simple shear flow as indicated by the mixing index. Moderately-sized bubbles were found in locations experiencing a variety of flow types, including rotation, simple shear, and dispersive mixing. Bubbles seen along $x=0$ were dwarfed by others further from the vertical center line, due to high extension rates in this area.

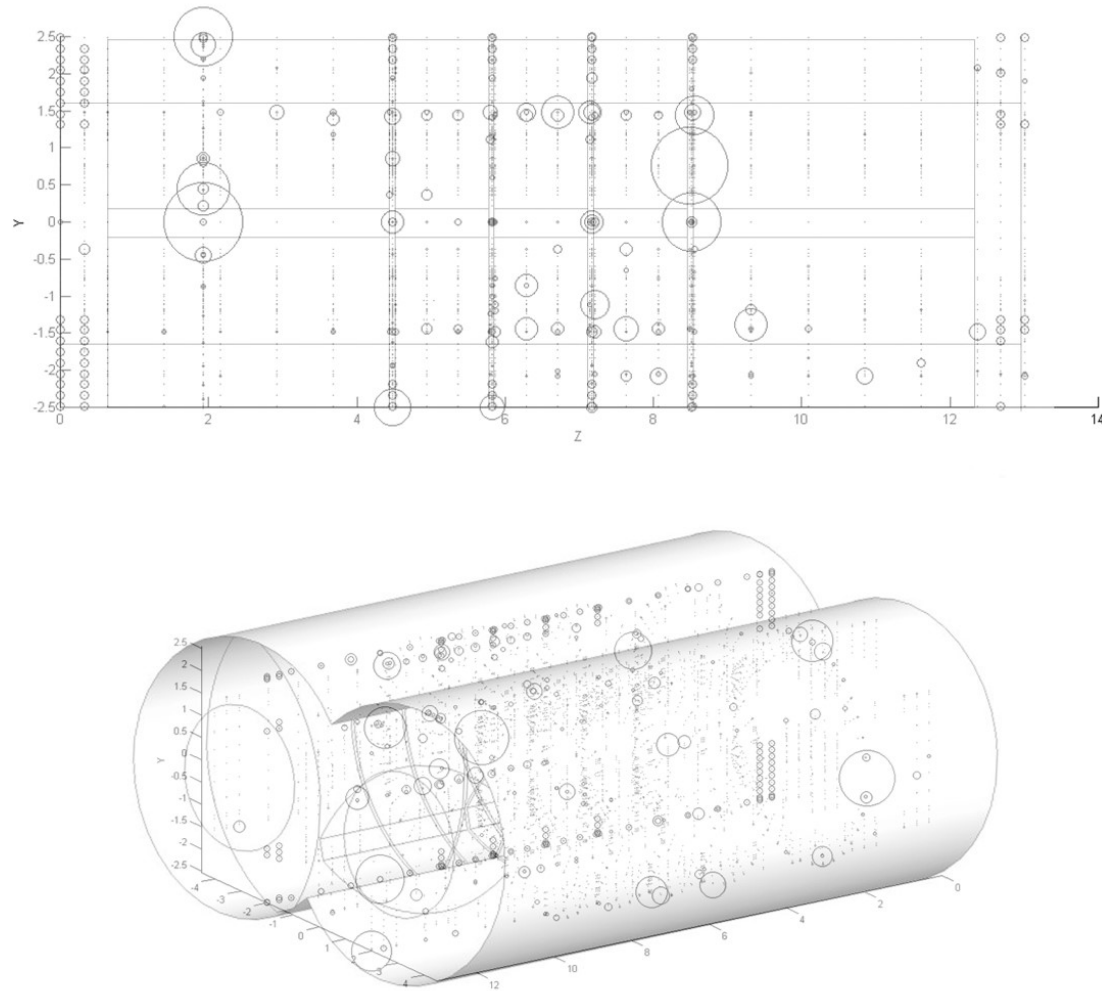


Figure 4.15. Maximum stable bubble diameter at 100rpm and 55.31cc/s through the mixer a) yz view, b) angled view.

Generally larger bubbles are found in the same plane as the maximum d_{max} in the mixer, for the same reason. Near the entrance of the mixer and above and below the center of the right paddle larger bubbles are also seen. These are areas of lower extension rates where fluid passes through a relatively large clearance. Some larger bubbles are seen just before the latter fused paddles and in the bottom of the mixer near the exit. A few relatively large bubbles are found near the paddle tips and in the gaps between the sequential paddles. This is surprising due to the high extension rates seen in these areas. This is likely due to the presence of predominantly shear flows in these areas which do

not promote the breakdown of bubbles. This mixed flow permits larger bubbles in areas anticipated to experience bubble dispersion. Small bubbles are seen in the horizontal center at the top and bottom of the mixer, and as well as in the axial center of the mixer between the two paddle sets where high extension rates are predicted.

At 20cc/s and 100cc/s the largest d_{max} values are seen near the vertical center of the mixer and the barrel wall in areas of mainly shear flow (Figure 4.16). The maximum d_{max} at 100cc/s is double that seen at 20cc/s. Significant bubbles are also seen in near the bottom of the mixer and again near the barrel wall when advancing axially. The smallest values are near the axial center of the mixer, in an area known to experience extensional flow. Similar maximum d_{max} values are seen on opposite sides of the mixer (Planes 7 and 8, Planes 11 and 12), suggesting similar effects of flow on bubbles in these paired areas.

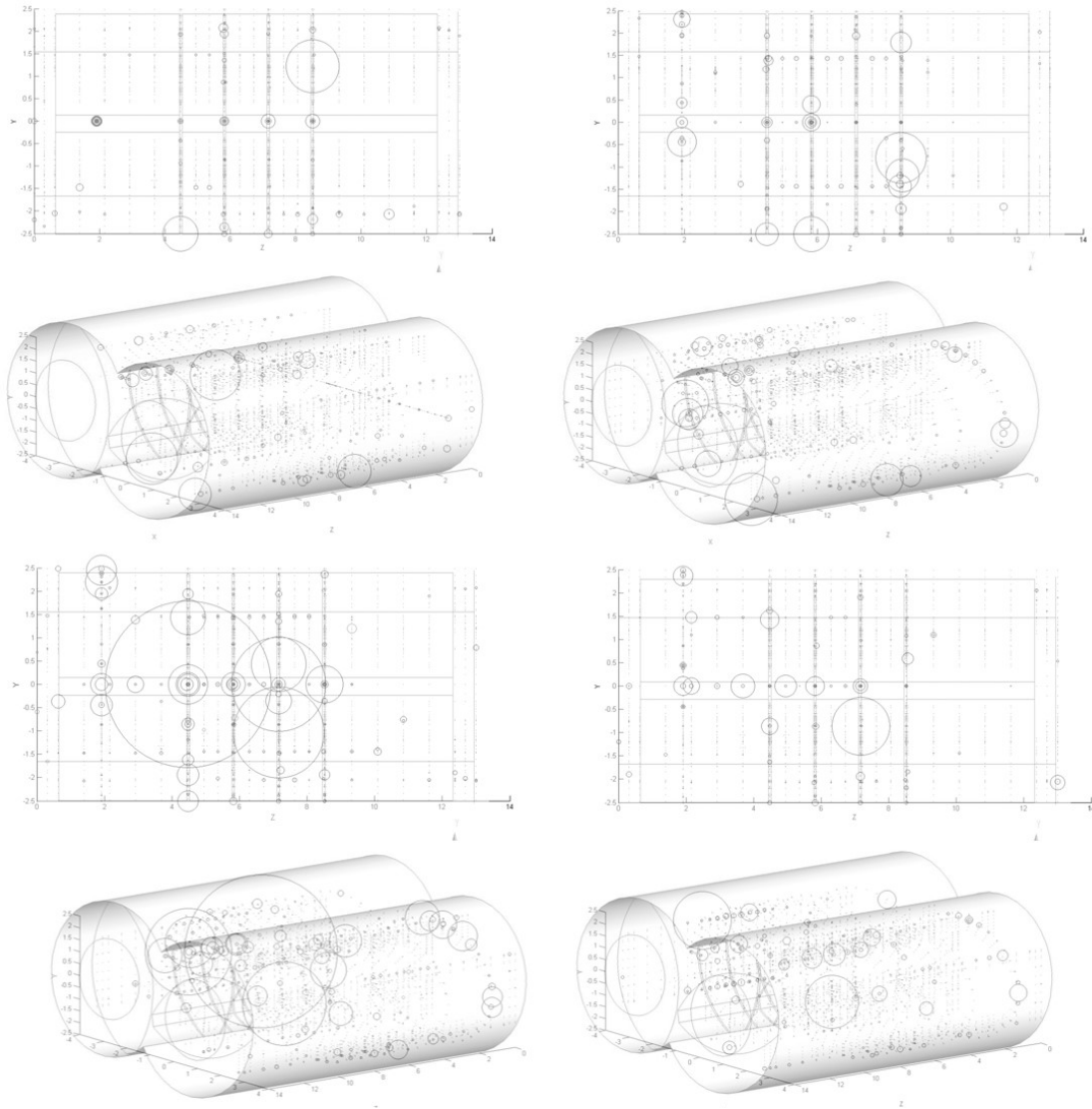


Figure 4.16. Maximum stable bubble diameter through the mixer a) 20cc/s, b) 100cc/s, c) 50rpm, d) 150rpm.

At 50rpm the largest d_{max} is seen on the left side of the mixer in an area not categorized as simple shear, extensional, or rotational flow. Nor was it categorized as an area of good dispersive mixing. The largest values are higher than maxima seen at other fluid inflow rates and mixer speeds. Additional large values are seen in areas of simple shear flow clustered near the vertical and axial center of the mixer, while the smallest d_{max} is seen near the axial center of the mixer. The region with the largest d_{max} is near the

beginning of the paddles modeled with gaps, while significant values are also seen in the middle of the gap-paddle section. This is unexpected as this area is seen to have significant extensional flow.

At 150rpm the largest d_{max} is also on the left side of the mixer, but in an area of simple shear flow. This maximum is the same order of magnitude as that seen at 100cc/s. The left side of the mixer also shows the largest number of high d_{max} values; and the largest bubble is seen near the end of the gap-paddle region. Additional large values are seen near the axial center of the mixer. The smallest d_{max} is seen near the axial center of the mixer corresponding with simple shear flow.

The value of this study is in providing a visualization and understanding of the distribution of shear rates and extension rates which then led to the calculation of maximum stable bubble diameter. Distribution of stable maximum bubble sizes is complicated by the trajectory of the fluid, which carries bubbles through the mixer. If bubbles pass through regions of high extension rates then they disperse and form small bubbles. But if the fluid streamlines escape regions of high extension rates and flow strength then it is possible that relatively large bubbles will survive the dispersion process. In fact in an earlier study with Newtonian fluids (Vyakaranam and Kokini, 2012) we observed that it is possible to observe a small fraction of relatively large bubbles. This study offers the tools to more precisely calculate bubble size distribution through the twin screw mixer than previously possible. In that sense it offers progress in state-of-the-art computational studies of twin screw mixers and the dynamics of how bubble sizes change and bubbles disperse in a mixer.

4.5 Conclusions

The role of extension and shear rate on bubble breakup and dispersion for Newtonian and non-Newtonian fluids was examined using direct calculations of the extension and shear rate distribution in a twin screw mixer. The extension rate, which has a much larger impact on bubble breakup, varies a great deal from one location to the next and depends on screw speed, mass flow rate, size of the flow channel, and interaction between the screws. Maximum extension rates are seen around paddle tips leading to small maximum bubble diameters. For a non-Newtonian fluid, peak extension rate values are also seen at paddle tips and near the center of the mixer, between the two paddles sets which continuously or periodically form a narrow fluid channel through which fluid is forced or pulled forward. No significant difference in extension rate values is seen with increasing axial distance.

The calculated maximum stable bubbles were plotted as a function of location to provide visual clarity for how bubble dispersion occurs and where the likelihood of bubble dispersion is higher. High shear rates are seen in regions with relatively low extension rates such as the tips of the right-hand paddle near the barrel wall and vice versa. The critical capillary number Ca_{cr} and the maximum stable diameter d_{max} are largely controlled by extension over shear flow even though shear rate can play a considerable role where extension rates are small. Different locations provide different types of flow and differing impact on bubble breakup.

Chapter 5 - Conclusions

CFD was utilized to determine the effect of screw configuration and mixer operation on dispersive mixing of a non-Newtonian fluid and the distribution of extension rate and maximum stable bubble size. Initially a 3D FEM simulation of a simplified mixer was used to examine the effect of mixer configuration and operating conditions on dispersive mixing. This was extended to encompass the complete mixing section for a more thorough understanding of fluid mixing. Further investigation included the importance of extension rate, critical capillary number, and maximum stable bubble diameter.

A combination of high shear rate and mixing index values is needed for bubble breakup. High mixing index values indicate increased elongation which can be caused by increasing fluid flow rate. Increasing paddle stagger angle increased maximum shear rate, seen particularly with 90° staggered paddles at 100rpm and 100cc/s. Despite this, no areas of efficient dispersive mixing were seen. Thus the parallel configuration was the best scenario for efficient dispersive mixing in the abbreviated mixer.

Peak shear rates and simple shear flow were seen in the center of the mixer. Efficient dispersive mixing was seen near the barrel wall where, combined with high shear rates, they produced a situation well-suited to bubble break-up. These are prime areas for fluid reorientation due to the narrow flow channels they form. Staggering the paddles caused low velocity and shear rate values, belying the idea that staggering paddles enhances mixing.

Both parallel and staggered paddle configurations in the nine paddle mixer saw an increase in velocity and shear rate with increasing mixer speed, as well as showing good

dispersive mixing and shear flow. The staggered paddle configuration experienced an irregular mixing index trend and mixed velocity effects with increasing fluid flow rate. Thus staggered paddles appear to deflect fluid at higher flow rate. Increased backflow and greater x and y velocity indicated better mixing and more disruption seen with increasing mixer speed.

The Bird-Carreau fluid showed a greater influence of paddle motion under a given set of operating conditions, likely caused by the inelastic property of the fluid. Compared to the power-law fluid, there was more backflow allowing more retention time for fluid mixing. Shear-thinning behavior also resulted in greater maximum shear rate as shearing became easier with decreasing fluid viscosity. This predominance of shear flow prevented areas of pure rotational flow.

Extension rate has a larger effect on bubble breakup than shear rate and its value varies with location. It is also dependent on screw speed, mass flow rate, flow channel size, and interaction between the screws. Maximum extension rate is seen at the paddle tips for both Newtonian and non-Newtonian fluids and corresponds with mixing index values of approximately 0.5, indicating a level of shear and elongation flow. For the non-Newtonian fluid, peak extension rate is seen in the center of the mixer in the narrow channel formed between the paddles. This area forms a positive scenario for bubble breakup as the fluid advances.

Peak extension rate values appear in areas of low shear rates, while low values exist in areas with high shear rates. Critical capillary number and maximum stable bubble diameter are influenced mainly by extension, but when extension rate values are low

shear rate can play a much larger role. Thus different locations in the mixer have varying impacts on bubble breakup due to the dominant flow type.

In evaluating the mixer variables we see that a high mixer speed promotes mixing. In contrast, a mid-range fluid flow rate is most promising as a desirable flow pattern has already developed and further increase enables fluid flow-thorough. In evaluating these simulations, increasing the number of revolutions results in diminishing returns. One revolution is sufficient to capture Newtonian fluid mixing behavior, while only a slight difference is seen between one and two revolutions for the non-Newtonian fluid. Staggering the paddles did not result in better dispersive mixing.

The most effective mixer is one that creates a convoluted fluid path, allowing sufficient residence time for shear and extension, forming narrow spaces through which the fluid can pass, while still advancing the fluid to gain the production advantage of a continuous mixer. This research has shown direct calculation of extension rates is possible via simulation and can be used to obtain critical capillary number and maximum stable bubble diameter. These parameters can be used to develop design criteria for dispersion of air and generation of nuclei for bubble growth. Further work would include a thorough validation of the non-Newtonian simulation work using experimental data.

References

- U.A. Al Mubaiyedh, R. Sureshkumar and B. Khomami, "Linear stability of viscoelastic Taylor-Couette flow: Influence of fluid rheology and energetics", *Journal of Rheology* **44** (2000) (5) p.1121.
- B. Alsteens, V. Legat and T. Avalosse, "Parametric study of the mixing efficiency in a kneading block section of a twin-screw extruder", *International Polymer Processing* **19** (2004) p.207
- M.M. Alvarez, J.M. Zalc, T. Shinbrot, P.E. Arratia and F.J. Muzzio, "Mechanisms of mixing and creation of structure in laminar stirred tanks", *AIChE Journal* **8** (2002) (10) p.2135.
- P.D. Anderson, O.S. Galaktionov, G.W.M. Peters, F.N. van de Vosse and H.E.H. Meijer, "Chaotic fluid mixing in non-quasi-static time-periodic cavity flows", *International Journal of Heat and Fluid Flow* **21** (2000a) (2) p.176.
- P.D. Anderson, O.S. Galaktionov, G.W.M. Peters, F.N. van de Vosse and H.E.H. Meijer, "Mixing of non-Newtonian fluids in time-periodic cavity flows", *Journal of Non-Newtonian Fluid Mechanics* **93** (2000b) (2-3) p.265.
- P.E. Arratia, J.P. Gollub and D.J. Durian, "Polymeric filament thinning and breakup in microchannels", *Physical Review E* **77** (2008) p. 036309.
- B. Ashokan, Developing methods for design of continuous mixers through 3D numerical simulation of flow and mixing, *Department of Food Science*, Rutgers University, New Brunswick (2008).
- B.K. Ashokan, L. Fanning, R.K. Connelly and J.L. Kokini, "Determination of the flow and mixing in a continuous mixer using LDA and 3D simulation", Proceedings of the Eighth Conference of Food Engineering, A topical conference held in conjunction with the 2003 AIChE Annual Meeting, San Francisco, CA (2003).
- B.J. Bentley and L.G. Leal, "An experimental investigation of drop deformation in steady, two-dimensional linear flows", *Journal of Fluid Mechanics* **167** (1986) p.241.
- F. Bertrand, F. Thibault, L. Delamare and P.A. Tanguy, "Adaptive finite element simulations of fluid flow in twin-screw extruders", *Computers and Chemical Engineering* **27** (2003) p.491.
- D.M. Binding, M.A. Couch, K.S. Sujatha and M.F. Webster, "Experimental and numerical simulation of dough kneading in filled geometries", *Journal of Food Engineering* **58** (2003) (2) p.111.

H. Cheng and I. Manas-Zloczower, "Study of mixing efficiency in kneading discs of co-rotating twin-screw extruders", *Polymer Science and Engineering* **37** (1997) (6) p.1082.

J.J. Cheng and I. Manas-Zloczower, "Flow field characterization in a banbury mixer", *International Polymer Processing* **5** (1990) (3) p.178.

F.H. Cisneros and J.L. Kokini, "A generalized theory linking barrel fill length and air bubble entrapment during extrusion of starch", *Journal of Food Engineering* **51** (2002) (2) p.139.

R.K. Connelly, Numerical simulation and validation of the mixing of dough-like materials in model batch and continuous dough mixers, *Department of Food Science*, Rutgers University, New Brunswick (2004).

R.K. Connelly and J.L. Kokini, "2-D numerical simulation of differential viscoelastic fluids in a single-screw continuous mixer: Application of viscoelastic finite element methods", *Advances in Polymer Technology* **22** (2003) (1) p.22.

R.K. Connelly and J.L. Kokini, "The effect of shear thinning and differential viscoelasticity on mixing in a model 2D mixer as determined using FEM with particle tracking", *Journal of Non-Newtonian Fluid Mechanics* **123** (2004) (1) p.1.

R.K. Connelly and J.L. Kokini, "3D numerical simulation of the flow of viscous Newtonian and shear thinning fluids in a twin sigma blade mixer", *Advances in Polymer Technology* **25** (2006) (3) p.182.

R.K. Connelly and J.L. Kokini, "Mixing simulation of a viscous Newtonian liquid in a twin sigma blade mixer", *AIChE Journal* **52** (2006) (10) p.3383.

R.K. Connelly and J.L. Kokini, "Examination of the mixing ability of single and twin screw mixers using 2D finite element method simulation with particle tracking", *Journal of Food Engineering* **79** (2007) (3) p.956.

B. Debbaut and M.J. Crochet, "Extensional effects in complex flows", *Journal of Non-Newtonian Fluid Mechanics* **30** (1988) (2) p.169.

B. Debbaut, J.M. Marchal and M.J. Crochet, "Numerical simulation of highly viscoelastic flows through an abrupt contraction", *Journal of Non-Newtonian Fluid Mechanics* **29** (1988) p.119.

M. Dhanasekharan and J.L. Kokini, "Viscoelastic flow modeling in the extrusion of a dough-like fluid", *Journal of Food Process Engineering* **23** (2000) (3) p.237.

M. Dhanasekharan and J.L. Kokini, "Design and scaling of wheat dough extrusion by numerical simulation of flow and heat transfer", *Journal of Food Engineering* **60** (2003) (4) p.421.

J. Dheur and M.J. Crochet, "Newtonian stratified flow through an abrupt expansion", *Rheologica Acta* **26** (1987) (5) p.401.

M.A. Emin and H.P. Schuchmann, "Droplet breakup and coalescence in a twin-screw extrusion processing of starch based matrix", *Journal of Food Engineering* **116** (2013) p.118.

L. Fanning, Characterization of velocity distribution in a Readco continuous mixer using Laser Doppler Anemometry, *Department of Food Science*, Rutgers University, New Brunswick (2009).

GAMBIT. *GAMBIT 2.4 User's Guide*. Fluent, Inc., Lebanon, NH (2007) p.3-91.

R. Giguere, F. Bertrand and P.A. Tanguy, "A three-dimensional mesh refinement strategy for the simulation of fluid flow with a fictitious domain method", *Computers and Chemical Engineering* **30** (2006) p.453.

H.P. Grace, "Dispersion phenomena in high viscosity immiscible fluid systems and application of static mixers as dispersion devices in such systems", *Chemical Engineering Communications* **14** (1982) p.225.

H. Huang and J.L. Kokini, "Prediction of dough volume development which considers the biaxial extensional growth of cells". Bubbles in Food. Ed. G.M. Campbell, C. Webb, S.S. Pandiela and K. Niranjana, Eagan Press. American Association of Cereal Chemists, St. Paul (1999) p.113.

T. Ishikawa, S.-I. Kihara and K. Funatsu, "3D non-isothermal flow field analysis and mixing performance evaluation of kneading blocks in a co-rotating twin screw extruder", *Polymer Engineering & Science*, **41** (2001) (5) p.840.

J.M.H. Janssen and H.E.H. Meijer, "Droplet break-up mechanisms: Stepwise equilibrium versus transient dispersion", *Journal of Rheology* **37** (1993) (4) p.597.

T. Jongen, "Characterization of batch mixers using numerical flow simulations", *AIChE Journal*, **46** (2000) (11) p.2140.

T.R.G. Jongen, M.V. Bruschke and J.G. Dekker, "Analysis of dough kneaders using numerical flow simulations", *Cereal Chemistry* **80** (2003) (4) p.383.

R. Keunings and M.J. Crochet, "Numerical simulation of the flow of a fluid through an abrupt contraction", *Journal of Non-Newtonian Fluid Mechanics* **14** (1984) p.279.

D.V. Khakhar and J.M. Ottino, "Deformation and breakup of slender drops in linear flows", *Journal of Fluid Mechanics* **166** (1986) p.265.

S. Kumar and G.M. Homsy, "Chaotic advection in creeping flow of viscoelastic fluids between slowly modulated eccentric cylinders", *Physics of Fluids* **8** (1996) (7) p.1774.

D.J. Lamberto, M.M. Alvarez and F.J. Muzzio, "Computational analysis of regular and chaotic mixing in a stirred tank reactor", *Chemical Engineering Science* **56** (2001) p.4887.

C.W. Leong and J.M. Ottino, "Increase in regularity by polymer addition during chaotic mixing in two-dimensional flows", *Physical Review Letters* **64** (1990) (8) p.874.

I. Manas-Zloczower, "Analysis of mixing in polymer processing equipment". *Rheology Bulletin* **66** (1997) (1) p.5.

I. Manas-Zloczower and M. Kaufman, "Mixing Measures". *Mixing and Compounding of Polymers: Theory and Practice*. Ed. I Manas-Zloczower. Munich: Karl Hanser Verlag, (2009) p.252.

M.E.H. Meijer and J.M.H. Janssen, In: I. Manas-Zloczower and Z. Tadmor, Editors, *Mixing and compounding of polymers: theory and practice*, Carl Hanser Verlag, New York (1994).

M.S.N.Oliveira, M.A. Alves, F.T. Pinho and G.H. McKinley, "Viscous flow through microfabricated hyperbolic contractions". *Experiments in Fluids* **43** (2007) p. 437.

J.M. Ottino, *The Kinematics of Mixing: Stretching, Chaos and Transport*, Cambridge University Press (1989).

Polyflow, User Manual, <http://www.fluent.com>, (2008).

P.M. Portillo, M.G. Ierapetritou and F.J. Muzzio, "Characterization of continuous convective powder mixing processes", *Powder Technology* **182** (2008) p.368.

P.M. Portillo, M.G. Ierapetritou and F.J. Muzzio, "Effects of rotation rate, mixing angle, and cohesion in two continuous powder mixers—A statistical approach", *Powder Technology* **194** (2009) p.217.

S. Prakash, Characterization of shear rate distribution in a model mixer using laser doppler anemometry, *Department of Food Science*, Rutgers University, New Brunswick (1996).

S. Prakash, M. Karwe and J.L. Kokini, "Measurement of velocity distribution in the Brabender Farinograph as a model mixer, using Laser-Doppler Anemometry", *Journal of Food Process Engineering* **22** (1999) (6) p.435.

S. Prakash and J.L. Kokini, "Determination of mixing efficiency in a model food mixer", *Advances in Polymer Technology* **18** (1999) (3) p.209.

- S. Prakash and J.L. Kokini, "Estimation and prediction of shear rate distribution as a model mixer", *Journal of Food Engineering* **44** (2000) (3) p.135.
- M.L. Rathod and J.L. Kokini. "Effect of mixer geometry and operating conditions on mixing efficiency of a non-Newtonian fluid in a twin screw mixer". *Journal of Food Engineering* **118** (2013) p.256.
- M.L. Rathod, B.K. Ashokan, L.M. Fanning and J.L. Kokini, "Non-Newtonian fluid mixing in a twin screw mixer geometry: 3D mesh development, effect of fluid model and operating conditions", *Journal of Food Process Engineering* (accepted 2014).
- M.L. Rathod and J.L. Kokini, "Extension rate distribution and impact on bubble size distribution in a Newtonian and non-Newtonian fluid in a twin screw co-rotating mixer", *Journal of Food Engineering* (submitted 2015).
- C. Rauwendaal, "Scale-up of single screw extruders", *Polymer Engineering & Science* **27** (1987) p.1059.
- Y.W. Stegeman, F.N. van de Voss and H.E.H. Meijer, "On the applicability of the Grace curve in practical mixing operations", *The Canadian Journal of Chemical Engineering* **80** (2002). (4) p.632.
- H.A. Stone, B.J. Bentley and L.G. Leal, "An experimental study of transient effects in the breakup of viscous drops", *Journal of Fluid Mechanics* (1986) **173** p.131.
- G.I. Taylor, "The formation of emulsions in definable fields of flow", *Proceedings of The Royal Society of London. Series A, Containing Papers of a Mathematical and Physical Character* **146** (1934) (858), p.501.
- K.V. Vyakaranam, Analysis of dispersive mixing and breakup of air bubbles during continuous mixing of viscous liquids using experimental and numerical simulation techniques. PhD Thesis. *Department of Food Science*, Rutgers University, New Brunswick (2012).
- K.V. Vyakaranam and J.L. Kokini. "Prediction of air bubble dispersion in a viscous fluid in twin screw continuous mixer using FEM simulations of dispersive mixing", *Chemical Engineering Science* **84** (2012) p.303.
- K.V. Vyakaranam, B.K. Ashokan and J.L. Kokini, "Evaluation of effect of paddle element stagger angle on the local velocity profiles in a twin-screw continuous mixer with viscous flow using Finite Element Method simulations", *Journal of Food Engineering* **108** (2012) (4) p.585.
- J. Wang and D.F. James, "Lubricated extensional flow of viscoelastic fluids in a convergent microchannel", *Journal of Rheology* **55** (2011) (5) p. 1103.

H.-H. Yang and I. Manas-Zloczower, "Flow field analysis of the kneading disc region in a co-rotating twin screw extruder". *Polymer Engineering and Science* **32** (1992) (19) p.1411.

J.M. Zalc, M.M. Alvarez, F.J. Muzzio and B.E. Arik, "Extensive validation of laminar flow in a stirred tank with three Rushton turbines", *AIChE Journal* **47** (2001) (10) p.2144.

J.M. Zalc, E. S. Szalai, M. M. Alvarez, and F. J. Muzzio, "Using CFD to understand chaotic mixing in laminar stirred tanks", *AIChE Journal* **48** (2002) (10) p.2124.

X.M. Zhang, L.F Feng, W.X. Chen and G.H. Hu, "Numerical simulation and experimental validation of mixing performance of kneading discs in a twin screw extruder", *Polymer Engineering and Science* **49** (2009) (9) p.1772.